공학박사학위논문

Microfluidic Immunodetection System Based on Asymmetric Particle Aggregation

비대칭 입자 응집 기반 미세유체 면역감지 시스템

2017 년 8 월

서울대학교 대학원

기계항공공학부

김 성 구

Abstract

Microfluidic Immunodetection System Based on Asymmetric Particle Aggregation

Sunggu Kim

Department of Mechanical and Aerospace Engineering

The Graduate School

Seoul National University

Micro- and nanoparticles are mobile substrates for capturing, transporting and detecting biomolecules or cells *via* surface functionalization and are used in bioanalytical researches. A large surface area of the suspension of such particles enables effective interaction with the target molecule in the sample solution. Controlled manipulation of these solid particles provides a multifaceted opportunity in the microfluidic format for on-chip bioanalysis. Thus, it is an important component of Point-of-Care applications or Lab-on-a-Chip devices.

In this thesis, we propose asymmetric immunoaggregated particles (AIPs) between two micro-particles of different size and magnetism, and propose methods to detect such aggregates including a microfluidic device. The number of particle aggregates formed *via* antigen-antibody reaction is known

to be an indicator of the quantity of target analyte. As with the conventional symmetric particle aggregation (single type particle aggregation), asymmetric aggregation also follows similar reaction behavior. Also, one can easily distinguish the aggregates using not only the size discrimination methods but also magnetic separation. Utilizing an additional physical property can simplify the transducer design.

We first developed an optical detection method that reads contours of particles/AIPs to investigate the behavior of aggregation. We, then, developed a magnet integrated sensor to image AIBs selectively, followed by a microchannel-based rapid detection device using a syringe pump. In the microfluidic device, AIPs were detected by optical monitoring in a flow under an external magnetic field. AIPs are attracted to the top surface of the channel by a magnetic field and made to slide along the upper surface by flow drag. This sliding behavior is in contrast with other particles such as magnetic (MG) and polystyrene particles (PS); while attracted MG hardly slide (or roll) due to their small size, PS quickly move with the flow due to the absence of magnetism. Sliding AIPs are optically monitored in a designated sensing area in the microchannel. A custom-built program code is used for counting the AIPs and further analysis such as number and velocity distributions that are correlated with target concentration. Furthermore, we analyzed the trajectory of each AIP inside the microchannel through force analysis for system optimization.

The proposed system shows a detection range of 40 pg/mL to 54 ng/mL for influenza type A H1N1 nucleoprotein (NP). The non-specific aggregation ratio was obtained at 2.47 ± 0.59% in the absence of antigen (BSA 0.1% w/v included) and the dynamic range was over 1000-fold. The detection takes 6

min, much faster than conventional methods (~10 min to several hours). This method uses microscopic power not more than 100×, so optical requirements are not strict and fluorescence are not required. Simple structure makes our sensor reusable, cheap, and robust.

Keywords: Particle-based immunoassay, Immunoagglutination, Asymmetric aggregation, Optical detection, Lab-on-a-Chip, Point-of-Care testing

Student Number: 2011-20692

Contents

List of Tables

List of Figures

Nomenclature

$\boldsymbol{m}$	Magnetic dipole moment of a magnetic particle ($A\ m^2$)
$\boldsymbol{B}$	Magnetic flux density (T)
$\boldsymbol{H}$	Magnetic field (A/m)
V	Volume of magnetic particle (m^3)
χ	Effective magnetic susceptibility of magnetic particle in water
M_s	Magnetized level of a cylinder magnet (A/m)
R_{mag}	Radius of a cylindrical magnet (m)
μ_k	Kinetic friction coefficient between antibody particle and microchannel surface
R_{AIB}	Effective radius of AIP (m)
f_D	Drag coefficient of the particle traveling in the vicinity of the surface
K	Drag force correction factor by the shape of AIP
v_f	Velocity of the sample flow (m/s)
h_c	Half of the height of the microchannel (m)
L_c	Width of the sensing area (m)
F_g	Gravitation force – Buoyance force of AIP (N)
θ	In the x-y plane, the angle between a straight line connecting the center of the PS and MG in the sliding AIP and the x axis (negative direction).

Constants

μ_0	Magnetic permeability of free space ($1.26 \times 10^{-6}\ N/A^2$)
η	Viscosity of water ($1.0 \times 10^{-3}\ N\ s/m^2$)
g	Gravitational acceleration ($9.81\ m/s^2$)
R_{MG}	Radius of a magnetic particle ($0.5\ \mu m$)
R_{PS}	Radius of a polystyrene particle ($1.4\ \mu m$)
φ_0	The angle between the straight line connecting the center of the PS and the MG of the sliding AIP and the wall (28.3°)
L_c	Width of the sensing area ($1180\ \mu m$)

Abbreviations

MG	Magnetic particle
PS	Polystyrene particle
AIP(s)	Asymmetric immunoaggregated particles

Chapter 1 Introduction

1.1 Particle-based immunoassay

Rapid and quantitative detection of target analytes is crucial in disease diagnosis, environment monitoring, and bioanalytical researches.[1-4] Immunoassay is a popular method to detect antigen owing to its high specificity. However, traditional immunoassays such as enzyme-linked immunosorbent assay (ELISA) require multistep antibody labeling, long assay time, and complicated equipment.[5] Recently, microfluidic immunosensors employed various sensing methods including optical,[6-9] surface plasmon resonance (SPR),[10, 11] and surface-enhanced Raman scattering (SERS).[12, 13] However, these methods still require bulky detectors and/or encoding and decoding processes.[14] In addition, immobilizing antibodies on the surface of a microchannel, is still a challenge for sensitive immunodetection.

Recently, micro particle-enhanced assays have attracted attention because of the rapid and flexible surface modification of particles.[15] Due to its high surface-to-volume ratio, micro particle-enhanced assays provide increased signal and low detection limit in reduced steps. In addition, the magnetic particles can be manipulated by an external magnetic field without an effect of magnetic memory.[16, 17] For example, methods of amplified sensitivity with digital ELISA, [18-20] isomagnetophoresis,[21] surface coverage assays,[22] and resistive pulse sensing (RPS) [23-25] have been proposed. The major benefits in the magnetic manipulation include a rapid preparation for antibody conjugation,[26] ease of particle isolation using magnetic fields,[27, 28] and amplified possibility of immunoreaction based on enhanced diffusion.[29]

Such magnetic characteristics of particles will allow various assays with lower detection minimum and quantitative signal. In contrast with aggregation assay of single type particle for detection, asymmetric aggregates of MG and PS formed *via* antibody-antigen-antibody binding confers multifaceted detection opportunity. Kim *et al.* demonstrated the use of nano MG and micro PS for immunoagglutination in the presence of target analytes.[30] The velocity of aggregate in solution was optically calculated under a magnetic field. The velocity was correlated with target analytes concentration. However, this approach requires manual tracking of each particle under well-defined experimental conditions. Moreover, it may require fluorescence or color labeling of particles for optical clearness.[31]

Here, we present a transduction principle for quantification the asymmetric aggregates (MG and PS) in a format that can be automated and robust against condition variation. Our sliding assay uses the attraction of the asymmetric immunoaggregated particles (AIP) to the upper surface of a microchannel, and sliding motion driven by flow drag. The number and size of the AIPs both increase to target concentration. While the drag force is correlated with the size of AIP, magnetic attraction force and surface friction force are merely correlated and almost cancel each other. Single MG and PS without aggregation move either much slower or faster respectively. Thus, one can count the total AIP number that passes through a defined area in a proper range of velocity and correlates such count with the concentration. This method allows automated calculation with a robust performance against condition variation such as the strength and position of a magnet, and particle size change. In contrast with the previous research [30] that used the velocity tracking of individual agglutination, our method enumerates such aggregates

in a window of velocity, resulting from the interplay between magnetic attraction and surface friction. This method enables precise sensing owing to a relative counting of aggregates per overall particles, and clear observation on a focal plane.

In this thesis, we analyze 6 min signal of measurement in the sensing area of 1.18 mm × 0.94 mm. We analyze the force balance to understand the movement of AIP, image processing method for characterization, and quantitative detection results with influenza type A nucleoprotein (NP) as a target protein.

1.2 Research objectives and contributions

The primary purpose of this study is to develop an immunodetection device capable of robust POC application. The most important prerequisites are; The device should be cheap and simple in structure, properly quantifies the target analyte in a solution, should be rapid in detection, provides high dynamic range and low limit of detection (LOD), and produces minimum non-specific signal. In addition, the following should be recommended; The system is label-free, compatible with other devices, not complicated so that bulky encoder/decoder (*e.g.* electrical system) are not required, and the chip is pattern-less or simple in design, and reusable. To achieve aforementioned requirements, we adopted immunoaggregation method of micro particles using antigen-antibody reactions. The design and analysis were conducted based upon aggregation ratio among the particle which is specific and quantitative outcome of immunoreaction. We used an optical method to directly observe and count the aggregates in a solution in a weak microscopic power (100×). In our configuration, the aggregates in a sample flow were

floated and slid through designated sensing window in response to the external magnetic field for selective counting. The image processing and statistics were obtained by custom-built program. Our microfluidic device satisfies the majority conditions suggested. We proposed asymmetric aggregation in immunoassay through particle aggregation. Asymmetric aggregation is a combination of magnetic particles and non-magnetic particles. Since the size and magnetism of aggregates are distinguished from others, the sensor transduction parts can be simplified. As a result, an interplay of magnetic, drag, and friction force was key parameters for our transducer.

1.3 Research overview

The thesis is organized as follows. First, basic particle-based immunoassays are introduced and asymmetric aggregation techniques are proposed. Next, a basic optical-based immunoassay method is presented as early attempts, followed by a sensing method through a microchannel. The section describes sensing principles, system configuration, and microchannel fabrication. For data acquisition part, MATLAB-based optical image analysis and particle velocimetry technique through video frame analysis is applied. In addition, a CMOS image sensor (CIS) for device miniaturization is integrated into the system for advanced applications. Finally, to understand and improve the performance of the sensor, trajectory and sliding motion of the aggregate inside microchannel were estimated through kinetic analysis.

Chapter 2. Particle aggregation assay

2.1 Conventional methods

Various particle-based immunoassays have been developed in past decades. Here are some popular techiniques utilizing particles.

2.1.1 Coulter counter (Resistive pulse sensor)

A Coulter counter (or Resistive pulse sensor, RPS) is a device that counts and sizes particles dispersed in a liquid. It is often used to analyze cells, bacteria, virus particles, and other bio-analytes.[23, 32-41] The device structure usually comprises two separated chambers connected by a small pore in between. As particles or cells in one chamber migrate to the other through the pore, they temporally block the electrical current path according to the size of particles, which allows to characterize the particles inside the solution.[42-44] The Coulter counters are capable of measuring agglomeration of nano- or micro-sized particles produced by antibody-antigen reaction. Increased aggregate populations can be regarded as a result of higher analyte concentrations and specific particle and aggregate distributions can be characterized by the device when they are randomly taken and traversed the pore. It captures the motion of particles across the pore by a data acquisition card of more than kHz range. In the case of a single particle, a small change in resistance is considered as a non-aggregate. On case of large agglomerate, the effect of electrically blocking of the microchannel is substantially increased, so that radical resistance change will be measured. The Coulter counter is widely used as an analytical transducer most commonly used in conjunction

with the particle agglutination-based assay. The cross-sectional area of the microchannel is designed to correspond to the particle size, and the particle information is converted into a suitable resistance signal. Nano-pores are often used for coagulation analysis of nanoparticles, and polydimethylsiloxane (PDMS) microchannels with a width of about 10 μm are often used for microparticles. In this case, however, an electrical analyzer is required and a current must flow through the sample solution. Also, the number of particles passing through a small microchannel can increase rapidly. In order to obtain sufficient statistical data to count particle aggregates, measurement time takes mostly longer than 20 min and there is also a clogging issue of the pore due to small size. Because the cross-sectional area of the channel is small, the measurement is possible only at low sample flow rates. If a high pressure gradient occurs between the chambers, there may be difficulty in capturing signals.

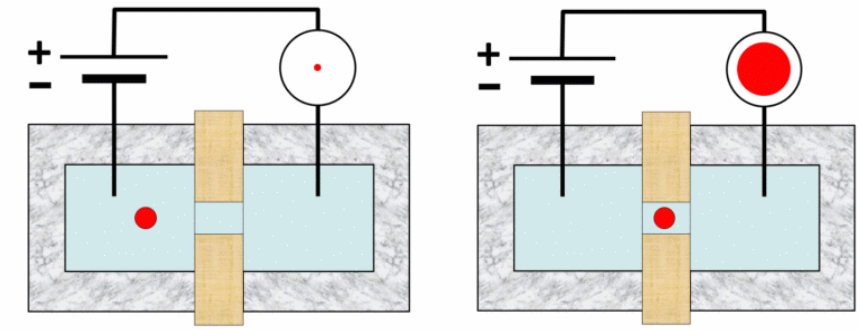

Figure 2-1. Schematic of RPS measurement. As the particle passing through the small pore in between the separated containers of conduction liquid, the electrical resistance increases.[34]

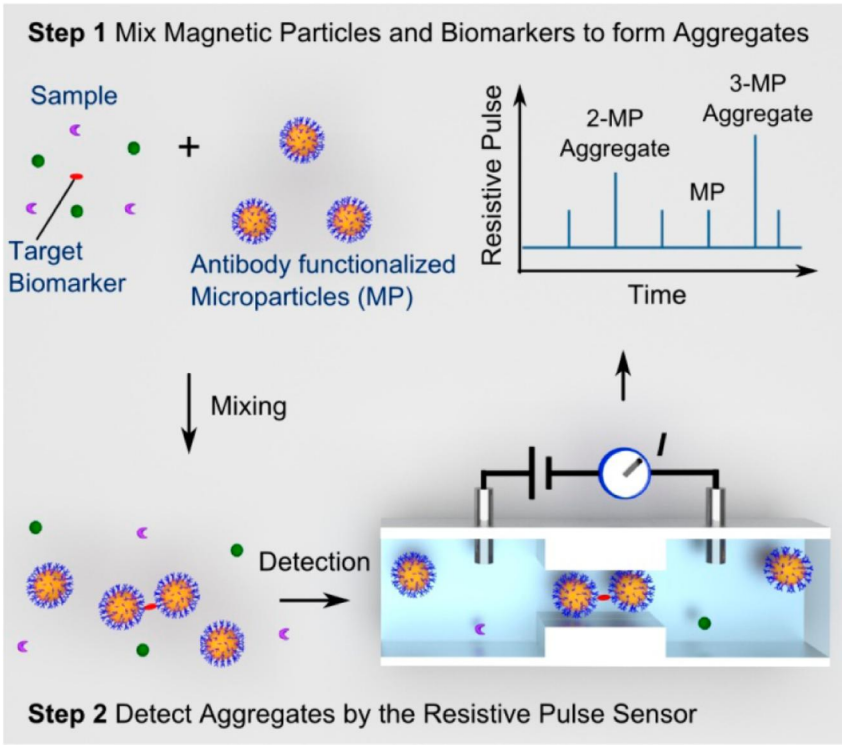

Figure 2-2. Schematic of RPS measurement using antibody-particle, the aggregates passing through the pore produces abrupt resistance change [23]

2.1.2 Magnetic separation & magnetophoresis

In addition to particle agglomeration for particle-based immunodetection, magnetic particles have been widely used as a method of labeling cells and bacteria, or even magnetophoresis. [45-52] For magnetic separation, each cell labeled with a specific magnetic particle using the corresponding antibody flows along the microchannel with outlets to which a nickel guideline is placed. As an example, Fig 2-3 shows a cell separation method using two different magnetic particles with different magnetic strength. A cell with bigger magnetic particle moves toward first outlet with higher angle of nickel

guide against main flow while the other cell moves second outlet with less nickel guide angle. A solution of several cells mixture can be successfully discriminated by this method.

A method called magnetophoresis has also been developed. Depending on the magnetic intensity of the magnetic particles, each particle or aggregate in the microchannel is refracted by an external magnetic field to separate the particles or sort the particles through relative magnetic susceptibility. In this way, it is possible to easily compare and divide the characteristics of particles without electrical equipment.

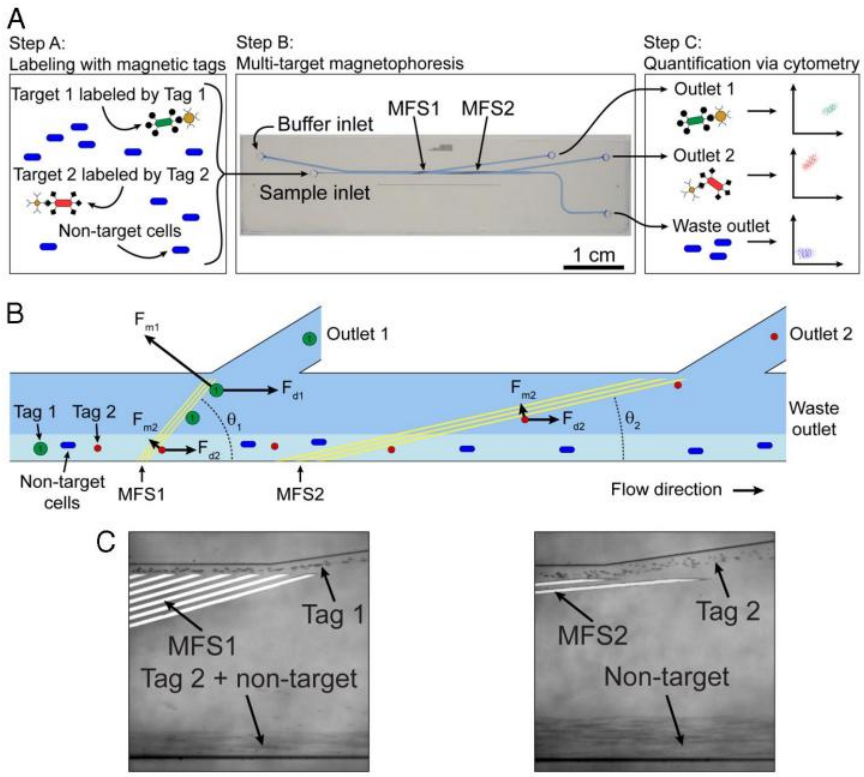

Figure 2-3. Separate two different cells from the microchannel with the nickel guide. With the aid of an external magnetic field, cells bound to different number of magnetic particles move to corresponding outlets. [45]

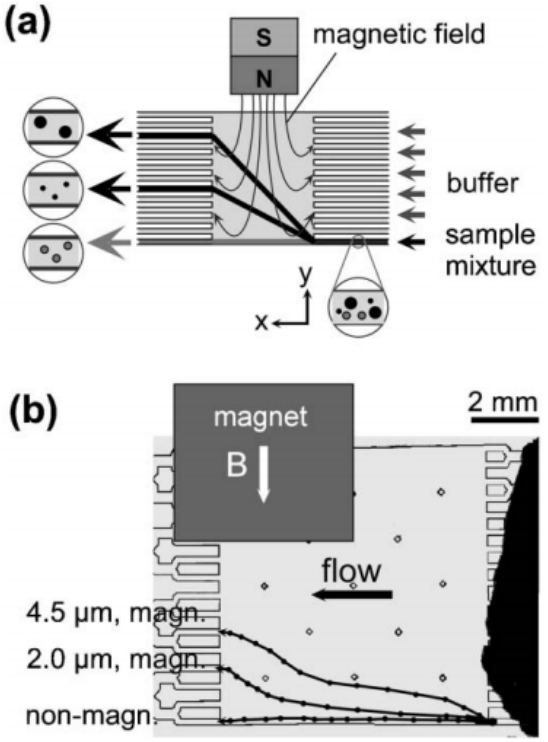

Figure 2-4. Magnetic particles are separated according to the size in response to the external magnetic field. [50]

2.1.3 Velocity tracking method

Antibody conjugated particles are considered as mobile substrates which provide a highly sensitive binding reaction against specific target analyte. Velocity method was firstly proposed using asymmetric particle aggregates [21, 53-56]. The small magnetic particles were agglomerated into large non-magnetic particles through the immunoreaction, and the degree of binding of the nanoparticles was converted into the velocity change under the external magnetic field. That is, when more magnetic particles are bound by a larger amount of antigen *via* an antigen-antibody reaction, the magnetic

susceptibility of the particles becomes larger, which makes them taking more force from the external magnetic field, resulting in faster attraction (deflection). Quantitative estimation of the amount of antigen can be made by differential velocity tracking of individual particles. The advantage of this method is that the immunobinding is sensitive even when the target antigen is lacking. However, this method requires manual tracking of individual aggregates and is vulnerable to initial position shifts. Also, since accurate particle discrimination is required, fluorescence or colored particles may be required. Fig 2-5 shows the detection concept of this velocity tracking method.

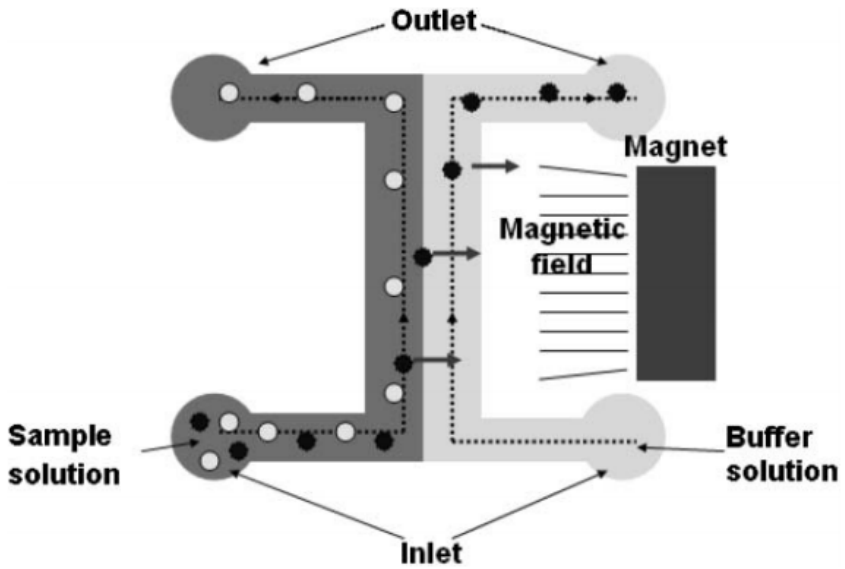

Figure 2-5. Concept of velocity tracking method. Each aggregate is attracted to the external magnetic field according to the number of magnetic particles in each aggregate that are correlated with the concentration of target analyte. [53]

2.2 Asymmetric immunoaggregated particles (AIP)

A new method of particle immunoaggregation has been devised which utilizes a combination of two different particles to perform a new sensing method.

2.2.1 Definition and basic features

AIP is an aggregate formed by immunobinding of MG and PS. The size of each particle generally ranges from nanometer to micron and superparamagnetic particle for MG. The PS is commonly used non-magnetic particle. Each particle is immobilized with a receptor capable of binding target analyte (protein, antigen, DNA, etc.), respectively. AIP is a result of asymmetric particle binding (shape and magnetism). The structural uniqueness allows it to easily be distinguished from other single particles in shape and magnetic strength. Characteristics of AIP are summarized as below:

(1) AIP provides sensitive reaction: Due to size difference of each particle component, the diffusion and encounter chance of each particle increases, resulting in aggregate production even in very low target concentration (*e.g.* picomolar or femtomolar bio-analyte detection).
(2) AIP can be easily distinguished from others by the shape analysis; It can be easily discernable by its contour against other particles.
(3) AIP can be separated by external magnetic field.
(4) AIP has moderate migration/sliding velocity compared to single particles in the microchannel under an external magnetic field; it takes more drag force due to increased size and takes magnetic

friction force at the same time (Detailed theoretical explanation will be given in other sections).

In this thesis, all types of immunoaggregation to be discussed in the later sections are based on the asymmetric particle aggregation.

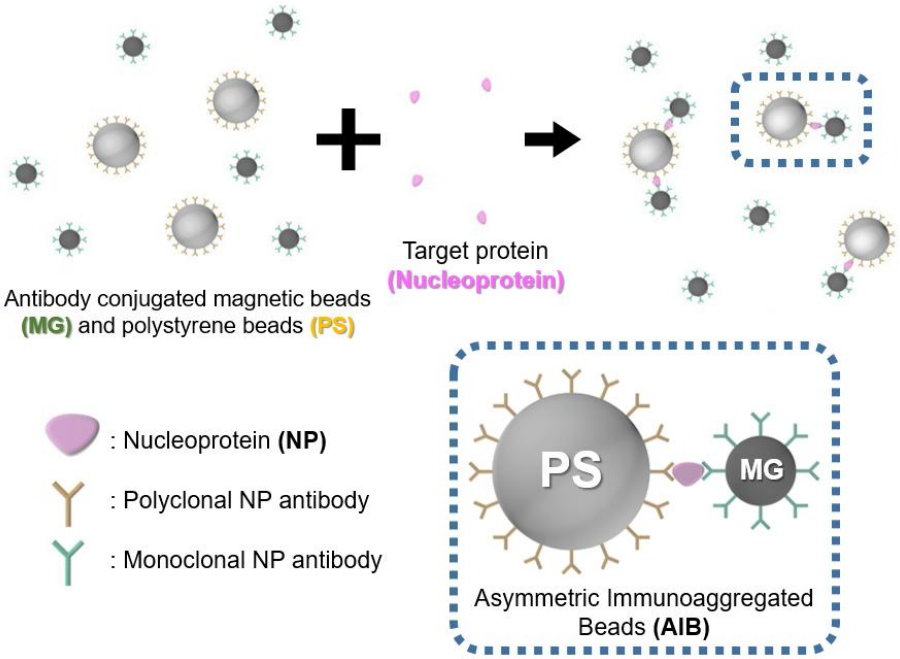

Figure 2-6. Concept of asymmetric particle aggregation. Two different particles form an aggregates triggered by specific target antigen binding.

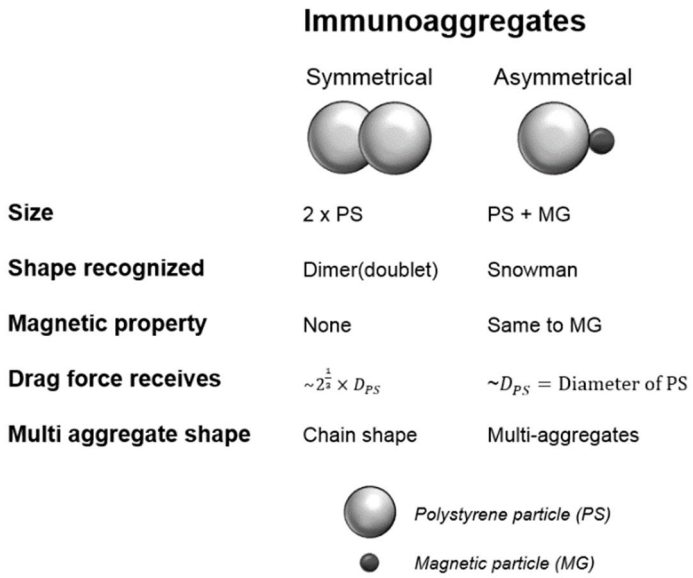

Figure 2-7. Comparison between conventional symmetric aggregation and asymmetric aggregation.

2.2.2 Receptor conjugations on particles

Biological and chemical sensors require special molecules to capture specific molecules, which are called receptors. The receptor provides the biosensor with binding sites for specific target analytes. The function of these receptors determines the characteristics and performance of the sensor; selectivity, sensitivity, and repeatability. An example is the combination of an antigen-antibody complex or an aptamer and a protein. In order to design an effective biosensor, it is important to understand the molecular association between these receptors and targets for consistent and robust performance.

There are various methods for immobilizing receptors on the particles. Most particles commercially available provide product-specific optimization protocols for receptor immobilization. 1-ethyl-3-(3-dimethylaminopropyl)

carbodiimide (EDC) and sulfo-N-hydroxysuccinimide (sulfo-NHS) method have been widely utilized for conjugating antibody on the carboxylic acid particles and a method of using biotinylated receptors on streptavidin particles is also popular method in particle fabrications. The receptors must be effectively bound to the particle to improve the binding chance of the target analyte. In other words, if the receptor is not sufficient for the particle surface or the orientation of the receptor is not favorable for binding to the target analyte, the binding capability will decrease and the chance of non-specific binding will increase. In general, micro- and nanoparticles have a very large surface area relative to their volume, so that a considerable amount of receptors are required for the preparation of conjugations, raising an economical issue as well. It is thus important to produce particles with reasonable receptor amounts based on users customized protocol on purpose.

In this study, EDC-NHS method was selected to immobilize antibodies on carboxylic acid functionalized PS and MG for robust and continuous particle fabrications. The EDC-NHS method produces a covalent binding between the primary amine of the antibody and carboxylic acid of the particle surface through an amide bond. Also, unconjugated native antibody can be used for this methods unlike other methods such as biotin-streptavidin bindings.

2.2.3 Particle fabrication and AIP formation

The process of conjugating antibodies to particles and producing AIP was as follows. First, all the chemicals were purchased from Sigma-Aldrich Corporation (USA) unless otherwise mentioned. Influenza type A H1N1 nucleoprotein and its polyclonal and monoclonal antibodies were kindly provided by the Korea Research Institute of Bioscience & Biotechnology

(KRIBB). Anti-human NP polyclonal antibody was conjugated to 2.8 μm polystyrene carboxyl particle (Carboxyl-polystyrene Particles, Spherotech, USA) and monoclonal antibody was conjugated to 1.05 μm superparamagnetic carboxyl particle (Dynabead MyOne Carboxylic Acid, Thermo Fisher Scientific, USA) by EDC and sulfo-NHS method. First, 1 μL of polystyrene particles (4.18×10^9 particles/mL) was diluted in 50 μL of deionized water (DI water, Milli-Q®) and then washed three times with centrifugation in 2000 g. 1.5 μL of magnetic particles (1.19×10^{10} particles/mL) was diluted with 50 μL of DI water and then washed three times by collecting the particles with an external magnet for 2 min. The particles were then resuspended in 50 μL of 15 mM 2-(N-morpholino) ethanesulfonic acid (MES, pH 6.0) buffer separately. Next, a solution was prepared by dissolving 10 mg of EDC and 15 mg of NHS in 1 mL of MES buffer (EDC-NHS buffer). To activate the particles for biomolecular capture, the particles were resuspended in 50 μL of EDC-NHS buffer and incubated at room temperature for 30 min. After incubation, the supernatant was carefully removed using the centrifugation and magnetic capture methods described above, and each particle was washed twice in 50 μL of fresh MES. For the AIP immunoassay, 50 μL of 0.15 mg/mL polyclonal antibody and the same amount and concentration of monoclonal antibody were mixed with the corresponding, activated particles, followed by incubation for 2 hours in orbital shaker at 100 rpm. Finally, both particles were washed 3 times in 1×phosphate buffered saline (PBS, pH 7.4) containing 0.1% w/v bovine serum albumin (BSA) and redispersed in the same solution, resulting in a volume of 320 μL each. The antibody conjugated particles were stored at 4 ℃ until further use. 50 μL of each antibody conjugated particle solution was mixed to make particles probe

of 100 μL. 50 μL influenza nucleoprotein solution was then added to the particles probe to complete 150 μL solution at target concentrations of 0-54 ng/mL. After 30 min of incubation at room temperature, the final particle concentration was 4.36×10^6 particles/mL for polystyrene, and 1.86×10^7 particles/mL for magnetic particles (1:4.27 in number ratio mixture). This ratio was selected after many trials for optimum results.

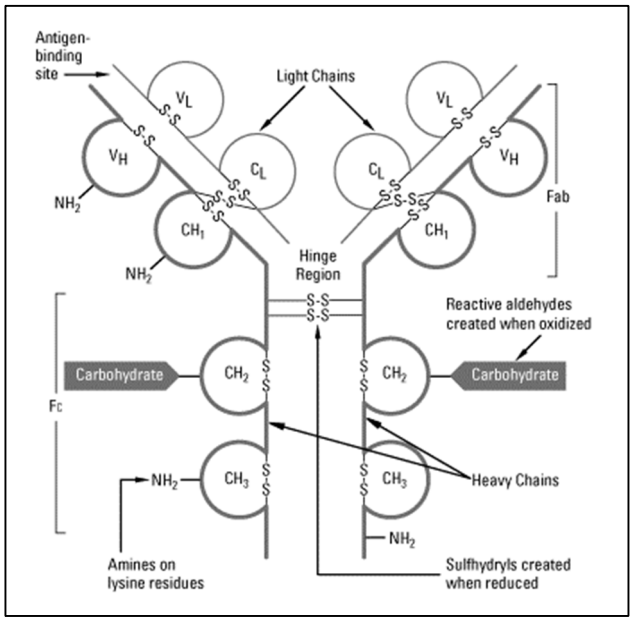

Figure 2-8. The structure of IgG antibody. The primary amine groups placed on the outside of the antibody were used for covalent conjugation between the antibodies and carboxyl particles *via* EDC/NHS method. [57]

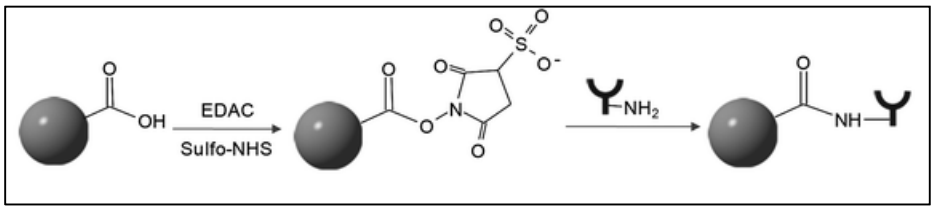

Figure 2-9. Process of covalent conjugation between particle and antibody. [57]

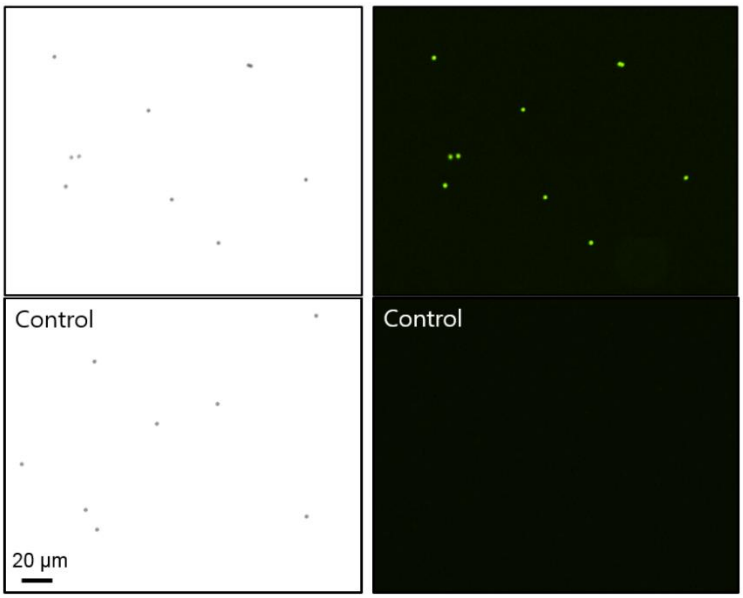

Figure 2-10. FITC labeling test on particles: To verify the immobilization protocol of IgG antibodies on Carboxylic particles, a parallel test was performed by labeling FITC-IgG on the particle. After conjugation, the interface of the particles was bright in green fluorescence. Based on this test, we could confirm that our EDC/NHS process is valid for antibody conjugation.

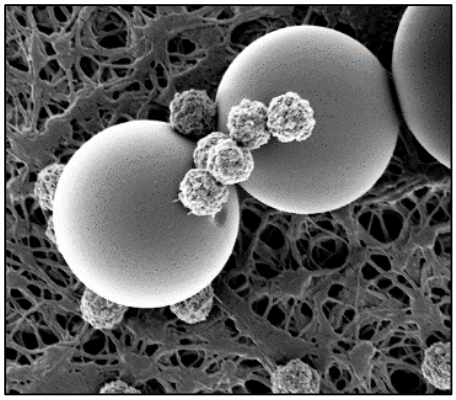

Figure 2-11. An FE-SEM image of PS and MG aggregates (4.3 μm + 1 μm combination). Multi-bonding was formed.

2.2.4 Asymmetric particles mixing ratio

One of the important factors in asymmetric particle aggregation design is the size and mixing ratio of each particle. When large particles (> 5 μm) are used, the number of antibodies required to produce the same number of probe particles increases, and the number of random collisions between particles (encounter chance) decreases during the assay, thereby reducing the aggregation signal. Small sized particles are thus generally viable choice. However, because our system is a fluorescence-free immunosensor based on an optical microscope, particles that are too small (*e.g.* less than 1 μm) may not be observed properly. We designed a detection system based on 2.8 μm particle size because 2.8 μm particles generate a sufficient aggregate with a reasonable amount of antibody. 500 nm and 1 μm particles are viable options of small particles for the asymmetric aggregation pairs. However, several experiments have shown that nanoparticles of 500 nm or less cannot give sufficient magnetic moment to aggregates when bound to PS. Therefore, 1 μm and 2.8 μm were determined as the optimum size range of each particle for proposed sensing system. Another issue is how to aggregate at a certain number of ratios when assaying by setting asymmetric aggregate particle size. In other words, as in the case of symmetric particles, it is necessary to decide whether to perform aggregation with a number ratio of 1:1, whether to increase or decrease the number of smaller particles, and what proportion of particles should be appropriate.

In some cases, the aggregation behavior was briefly tested. It was confirmed that the aggregation was increased in proportion to the amount of antigen in the region where the number of two particles was comparable. Because of the small size of MG, it was possible to observe proper

aggregation with relatively large number. As calculated by the surface area ratio, PS is 7.8 times wider than MG, thus exhibiting higher antigen binding capacity. Therefore, the aggregation assay should be designed by increasing the number of MGs. At the same time, if the amount of free MG is too much, side effects such as noise signal and increase of antigen consumption are increased. Therefore, the ratio between the two particles is about four times the optimum. The final particle number ratio was set to PS:MG = 1:4.27 considering particle fabrication. The results can be seen in the figure below.

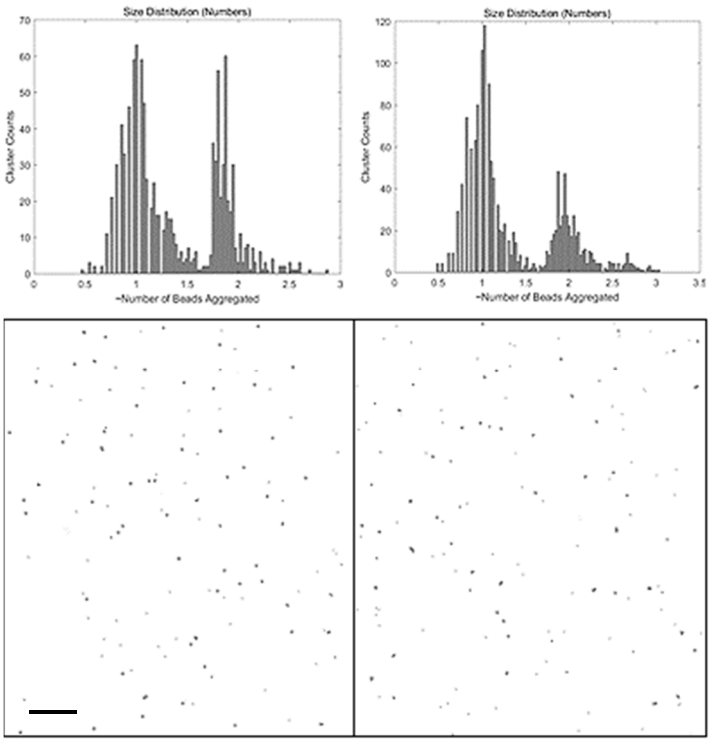

Figure 2-12. Various aggregation mixture ratio and the results. Depending upon the number mixture ratio, distribution graph shows relative peak height. Scale bar: 30 μm (Left: 1.5:1, Right: 4:1 mixing ratio of MG and PS).

2.2.5 AIP discrimination strategy – Shape reading

Another feature of AIP is the size asymmetry between the two bonded particles. Through this, the shape can be distinguished from single particles or symmetric aggregation. The simplest contour reading used in actual experiments is as follows. First, a single particle (spherical) is observed in a circular form under a microscope. The circumference and area of the circle are 2πR and πR^2, respectively, and ratio of circumference to area becomes $\frac{2}{R}$. In the case of a particle with a radius of $r = \frac{1}{3}R$, which is 3 times smaller in diameter (Similar to MG:PS radius ratio), the circumference to area ratio are also $\frac{2}{r} = \frac{6}{R}$. In the case of a shape in which two particle are in contact with the surface, the total circumference is $\frac{8}{3}\pi R$ and the area will be $\frac{10}{9}\pi R^2$. Therefore, in this case, the peripheral area ratio is $\frac{12}{5R}$. When image processing recognizes each particle in a real experiment, it reads the circumference and area information of the connected object as a single. Considering this fact, assuming that the recognized area is a circle, the radius is obtained as $\frac{10}{9}\pi R^2 = \pi R^{*2}$ or $R^* = \sqrt{\frac{10}{9}}R$. Thus, the AIP ratio of the two particle contacting the surface is $\frac{12}{5R} = \frac{2.53}{R^*}$. It can be classified by recognizing the shape of asymmetric aggregation because the circumference of the individual particles is increased by about 27% compared with that of a single particle ($\frac{2}{R}$). AIP, which is usually regarded as a microscope, is not a very ideal snowman, so if we set a criterion that includes the appropriate margin condition (about 15%), we can classify it with an accuracy more than 90%. In the case of symmetric aggregation, on the other hand, the circumference and area ratio is

$\frac{2.82}{R^*}$, which is about 41% more that of a single particle. Therefore, if the area of the single particle is larger by 15% ~ 35% than the area ratio of the single particle, it becomes a suitable shape recognition standard for classifying AIP only (In fact, no upper limit was established in the program code because any kind of aggregates can be considered a result of antigen-mediated aggregation (even in the case of symmetric aggregation)). Fig. 2-13. is a summary of aggregation clarification, and an example of program processing is presented in Fig. 2-13.

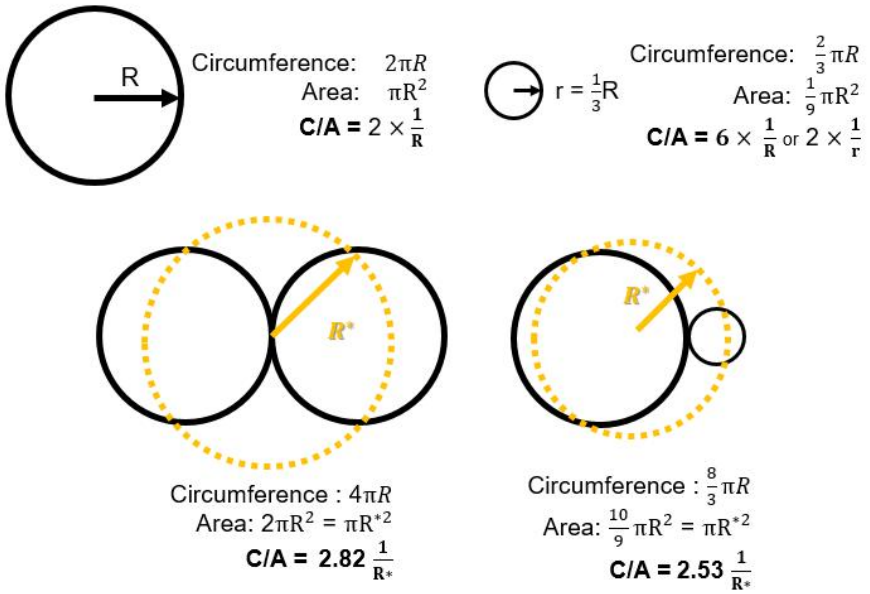

Figure 2-13. Circumference and area and their ratio of each aggregate.

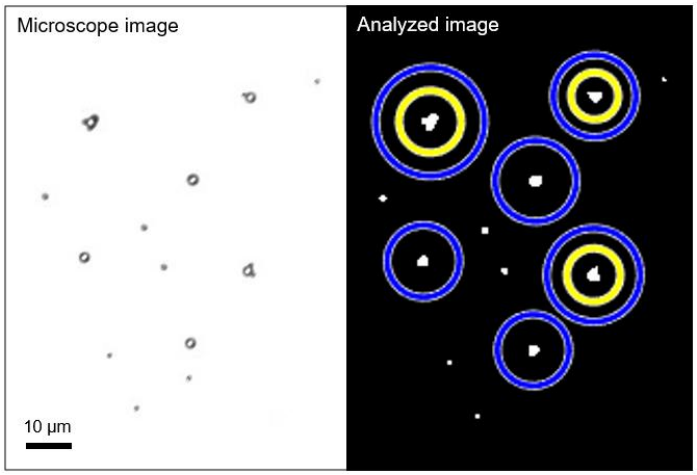

Figure 2-14. AIP shape recognition process. The microscopic particle sample image at a concentration of 10 pM NP (left side) and processed image to discriminate the aggregates and single particles (right side). Blue (bigger) circle indicates PS and aggregates, Yellow (small) circle: only AIPs.

2.3 AIP formation and size distribution

2.3.1 Nucleoprotein detection

Influenza type A H1N1 nucleoprotein was used as a model antigen to verify the AIP sensing concept. It has been widely accepted that the volume fraction of the aggregate to the total volume of particles represents the concentration of the protein at given probe particles concentration.[23] Similarly, in case of our proposed approach, we hypothesized that the formation of asymmetric aggregates increases with the concentration of the protein. To confirm this, we examined the quantitative relationship between protein concentration and the volume ratio, and the average size of AIP. First, an independent characterization was conducted to evaluate AIP formation in the solution prior to the microchannel sliding assay. Microscopic particle

sizing method was used to identify the AIP formation.[58, 59] In the microscopic sample image, the size distribution was obtained by the number of pixels of each recognized object, and the AIP was selectively classified through the circumference and area ratio of the object that represent the shapes of cluster. Fig. 2-15 is an actual size distribution with the scale applied. AIP sample with a target NP concentration of 5.4 ng/mL were observed on a microscope slide (4131 particles (MG, PS particle, and AIP) were randomly captured). Through image analysis, 510 (12.4%) of them were identified as AIP. The size of each particle was determined as 1.02 ± 0.26, 2.81 ± 0.30, and 3.45 ± 0.60 μm for single MG particle, single PS particle, and AIP, respectively, in a good agreement with the nominal size of each particle. The number of AIP formed by multiple bindings rather than a single binding of PS and MG particle was approximately 121, accounting for 2.9% of total particles and 23.7% of total AIP. Since the monoclonal antibody targets only one epitope of the NP, MG-MG self-aggregation induced by NP hardly occurred. At each NP concentration, the fraction of AIP was calculated in the same manner and the fraction increased with increasing NP concentration. The fraction of multi-bonded AIPs, defined as AIP of more than twice the average size of a single PS-MG AIP, also increases with increasing NP concentration (Fig. 2-16). In addition, this multi-bonded AIPs increases for the total AIPs, indicating the average size of AIP increases. The ratio between PS and MG particle was carefully selected here, after repeated tests; between the ratio of 1:1 and 1:10 of PS:MG particle, 1:4 showed decent aggregation signal. At this aggregation ratio, there was relatively little free MG particles to interfere sliding AIPs in the microchannel and sufficient aggregation signals could be obtained. At concentrations above 54 ng/mL (~ 1 nM), the binding

capacity of individual particles rapidly decreases and the aggregation signal begins to decrease again. Therefore, the detection interval obtained from the calibration curve based on the experiment is 0 to 54 ng / mL, and 40 pg / mL to 54 ng / mL when the LOD is considered.

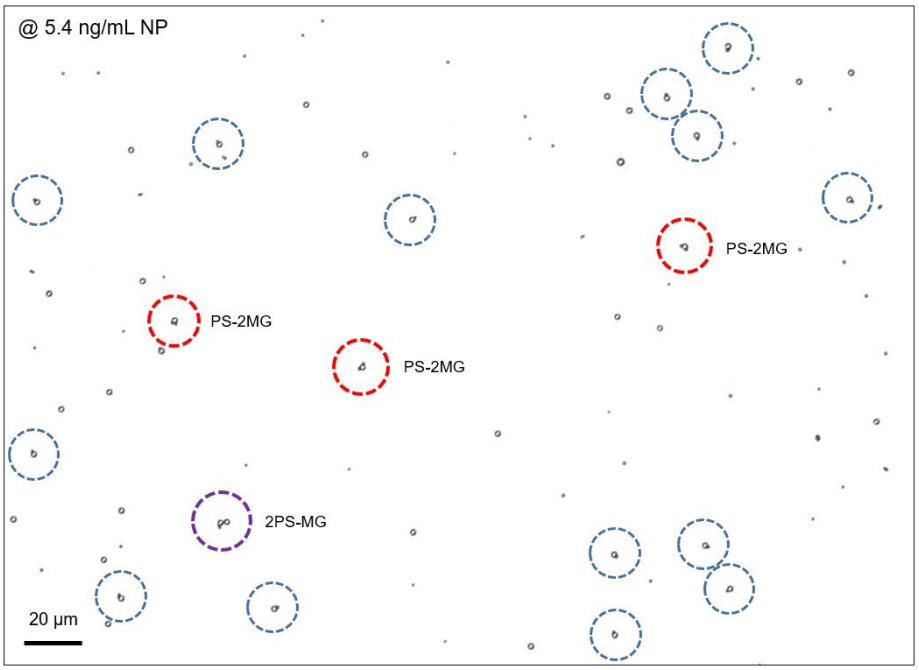

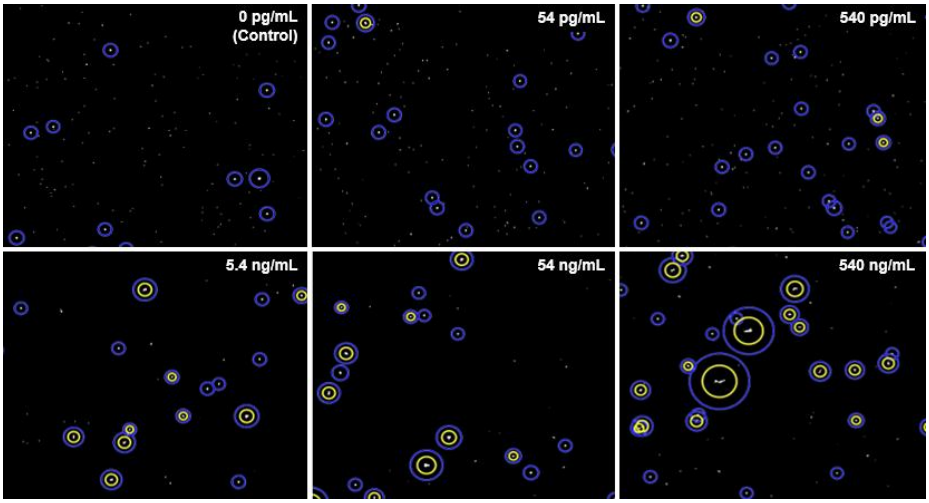

Figure 2-15. Particle aggregation measurement results: (Top) A microscopic image of a sample. (bottom) Results of processed images of random particles in samples. As the target concentration increased, more clusters were formed *via* antibody-antigen-antibody complex binding. Blue circles: PS particles, Yellow circles: AIPs

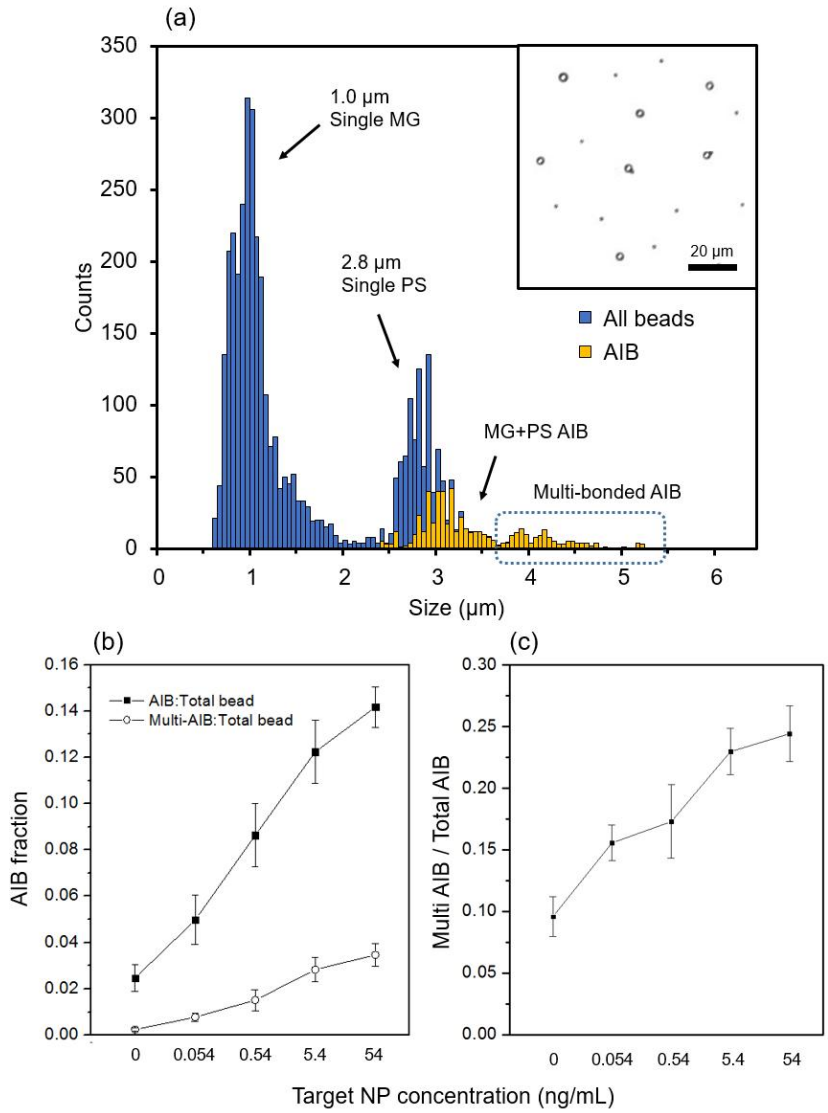

Figure 2-16. Particle aggregation characterization *via* image analysis. (a) Size distribution of single particles and AIP at 5.4 ng/mL of NP concentration. The inset is an optical image of single PS, MG and AIP, which is used for image particle sizing method. (b) Number fraction of AIP and multi-bonded AIP at different NP concentration in PBS. Fractions were calculated by dividing the number of AIPs by number of all particles (3100 ~ 4384, depending on the

sample). (c) The ratio between multi-bonded AIPs and total AIPs. 3 samples were prepared and measured at each concentration.

2.3.2 Human ferritin detection

An asymmetric particle aggregation test in addition to the NP was performed with ferritin as an additional model antigen. This confirms that the AIP method is still valid for various antigen-antibody sets. Ferritin is an iron storage protein of inflammatory markers with a molecular weight of 450 kDa. For detection of human ferritin protein, biotinylated anti-ferritin polyclonal antibody was bound to streptavidin particles. For the ferritin test, polystyrene particles size was reduced to 2.1 μm and streptavidin magnetic particles size was same (1.05 μm). The concentration of each particle was 3.97×10^6 /mL (2.1 μm, PS). 3.17×10^7 /mL (1.05 μm, MG). For the biotinylated antibody, the EDC / NHS method was used in combination with other streptavidin (Dissociation constant = $\sim 10^{-15}$). Each particle was conjugated with ferritin antibody based on the manufacturer's instruction, and the final number ratio of PS to MG mixture was 1:8. Finally, the aggregation experiment was performed by reacting the antibody particles with diluted ferritin at room temperature for 30 min. Fig. 2-17 presents the test result with ferritin protein. As the concentration of ferritin increases, more AIPs are formed.

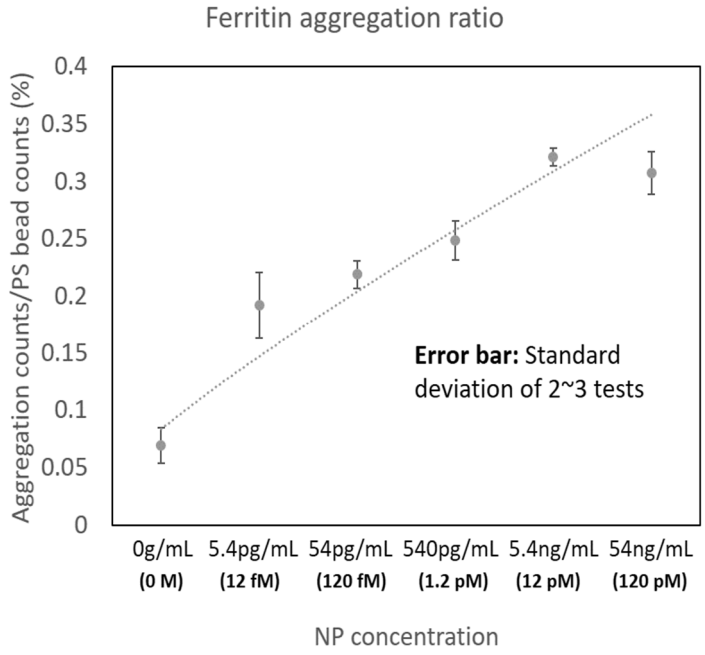

Figure 2-17. Ferritin aggregation test: 2.1 and 1.0 μm, PS and MG were used as 1:8 number ratio mixture. The aggregation increased as the target ferritin concentration increased. 0.1% w/v BSA were added for all samples to minimize non-specific aggregation.

2.3.3. Various types of aggregates formation

Another feature to mention about asymmetric particle aggregation is that particle size and antibody can be adjusted to produce various size of aggregates. This enables application such as multiplexed detection by utilizing multiple particles. Also, a discrete size distribution can be obtained due to the size difference of each particle. For example, when particle sizes are increased to 2.7 and 4.3 μm and aggregated, agglomerates of various sizes and shapes are produced. Fig. 2-18 shows an example of this kind of biological analysis, in which particles 2.7 and 4.3 μm in size combine non-biased with the

possibility of binding. We can extract several types of aggregation patterns if we develop appropriate multiple aggregation that binds each antibody to another and diversifies its size and does not interfere with the size standard deviation of each particle for multiplexing applications.

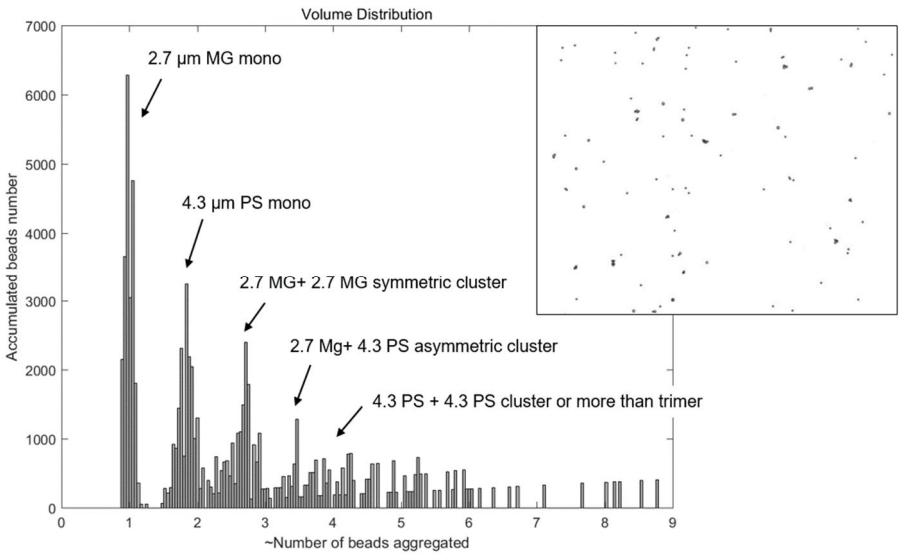

Figure 2-18. Various types of aggregates produced by a mixture of 2.7 and 4.3 μm-sized particles. Various combinations have been produced along the binding chance between the particles.

2.4 Magnetic surviving assay

Another feature of the AIP is that the aggregate has a magnetism. That is, since the MG are bound on PS, the aggregates can be easily separated by an external magnetic field and quantitatively counted as well. We have developed another sensing method that utilizes only the magnetic properties of the AIP.

2.4.1 Idea and detection procedure

The PS and MG have a size of 4.3 μm and 500 nm, respectively (reduced from 1.05 μm for MG) were used for immunoaggregation. The aggregates that had been produced from the antigen-antibody reaction, captured by external magnetic field. The magnetic particles have a small size compared to the wavelength of the visible light and are not easily discernable by an optical microscope. Thus, captured AIPs will be recognized as 4.3 μm sized PS particles and indicate how many aggregates were produced in the reaction vial since observed PS should be AIPs. By just counting this AIPs captured, one can estimate the aggregation ratio and correlate the target analyte concentration. The specific procedure is as follows.

1. The 4.3 μm PS and 500 nm MG were coated with polyclonal and monoclonal antibodies, respectively.
2. Antibody-antigen-antibody reaction was induced by injecting NP to the PS and MG mixture in a vial for 30 min.
3. An external magnet is applied at the side of the vial and the supernatant and unbound single PS were removed by replacing the buffer with fresh one through pipetting.
4. ~10 μL of the remaining solution was taken and put on the sliding glass and the number of PS particles (conjugates) was counted through a microscope.

In this configuration, shape recognizable method is not required on the captured particle images. With a help of the bigger size of PS, optical

magnification from the microscope was substantially reduced. The amount of antigen can be calculated after counting the "survived" AIP together with the calibration curve. The method is simple and similarly utilized under a name of magnetic handling (*e.g.* magnetic washing, magnetic separation, …)

Figure 2-19. Sequence of the magnetic surviving assay: First, two particles (PS and MG) are washed. Second, two particles are conjugate with corresponding antibodies, Third, antibody conjugated particles were mixed with target antigen. Forth, after antibody antigen binding reaction, the aggregates were attracted by an external magnetic field and the supernatant and remainders were removed by fresh buffer. Finally, the remaining particles (AIPs) were taken and counted through a microscope.

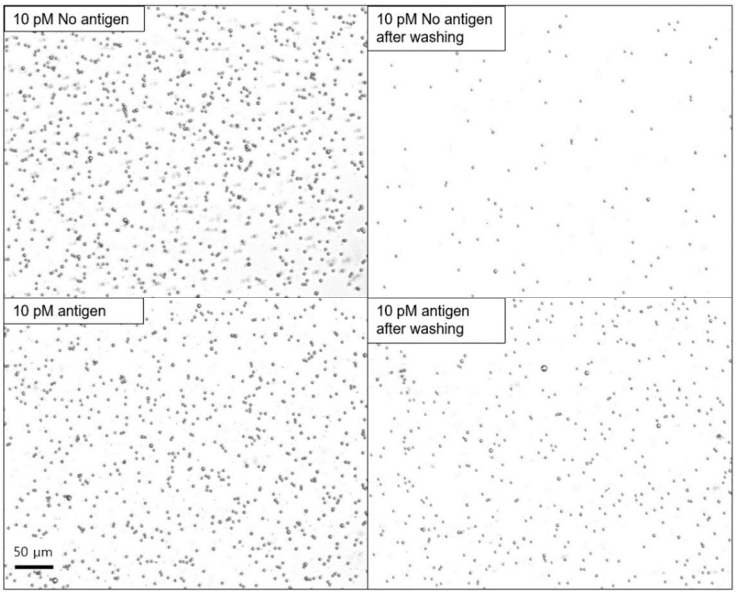

Figure 2-20. Magnetic surviving assay test at 10 pM target antigen concentration (Microscope image). PS (4.3 µm) and MG (500 nm) were mixed at 1:10 number ratio.

2.4.2 Device integration with lens-free CMOS image sensor

Since the magnetic surviving assay requires low microscopic magnification to distinguish and count the particles, we replaced the transmitted microscope into a bare image sensor called CMOS image sensor (CIS) to count the AIPs (survived particles). In particular, we removed the lens part from the image sensor, since the size of PS is relatively big and the exact shape reading was not highly necessary. The overall process follows the aforementioned the protocol of 'surviving assay'. However, in washing step, the vial was still mounted on both image sensor and magnet (Fig. 2-21). By comparing the number of PS(AIPs) before and after washing, we can count and calculate the target analyte in the sample solutions. The particle image

from the lens-free CIS are generally blur due to diffraction patterns. The angular spectrum reconstruction method was applied to reconstruct the image to original form. Fig. 2-22 shows the process and concept of the angular spectrum reconstruction of a particle in the solution and Fig. 2-23 presents captured CIS image of the sample before and after washing after image reconstruction. We can simply calculate the distribution of each sample of each case to obtain a sensing signal. Especially, due to the high sensitivity, this magnetic surviving assay shows much sensitive aggregation signal than conventional symmetric aggregation method (Fig. 2-24).

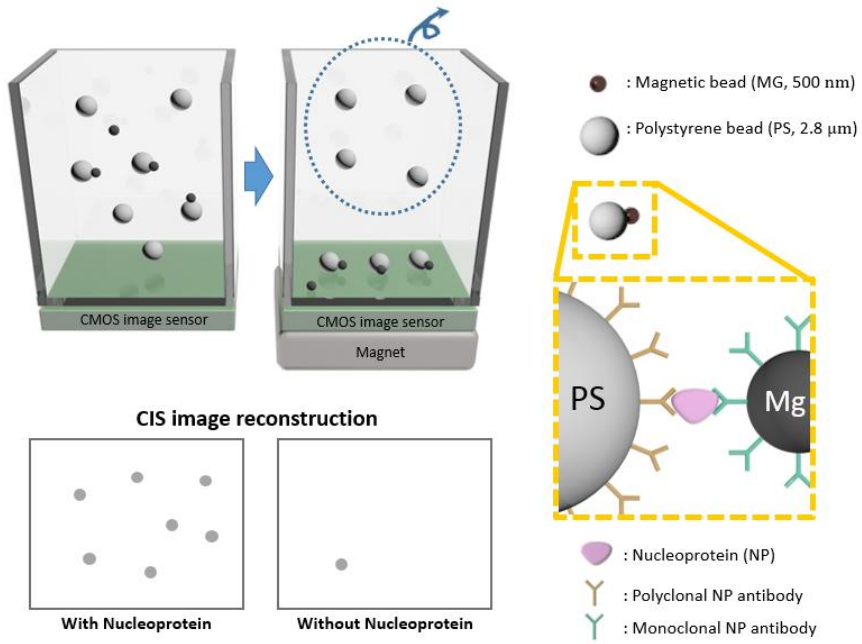

Figure 2-21. Concept of magnetic surviving assay. Aggregation of PS and MG attracted to the bottom surface due to the external magnetic field and monitored through CIS. Non-binding particles are easily eliminated from the solution at washing steps. By comparing the number of “survived” PS before

and after washing step under external magnet, we can easily correlate the concentration of target analyte by AIPs count.

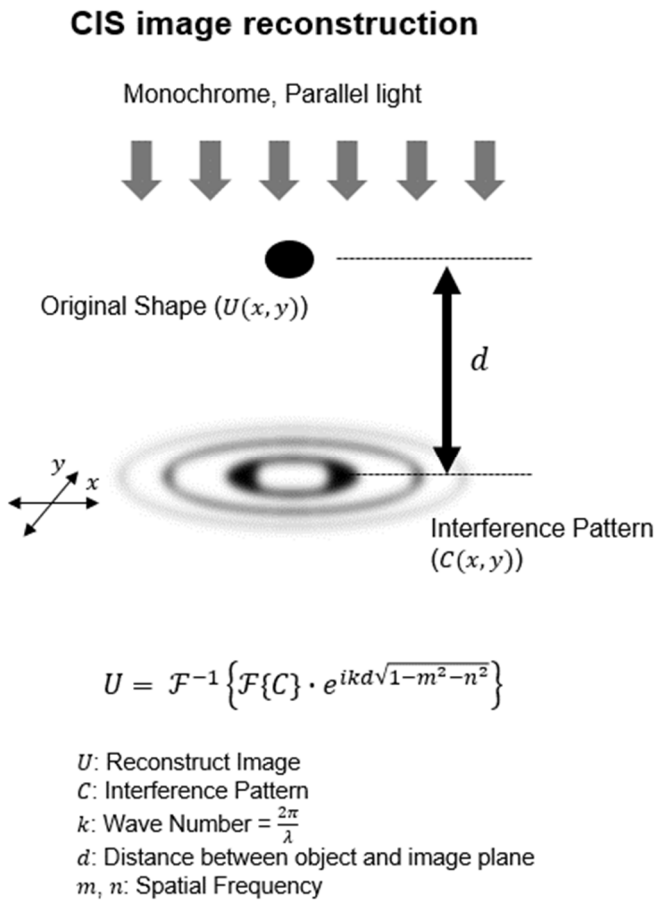

Figure 2-22. Image reconstruction method (Angular spectrum reconstruction). A parallel light coming from the object-top produces a diffraction pattern on the bottom sensor surface due to a spherical object in the middle in the absence of a lens. CIS specification: Each pixel size: 1.4 μm × 1.4 μm, Number of pixels: 2048 × 2036, CIS surface area: 3.2 mm × 2.4 mm

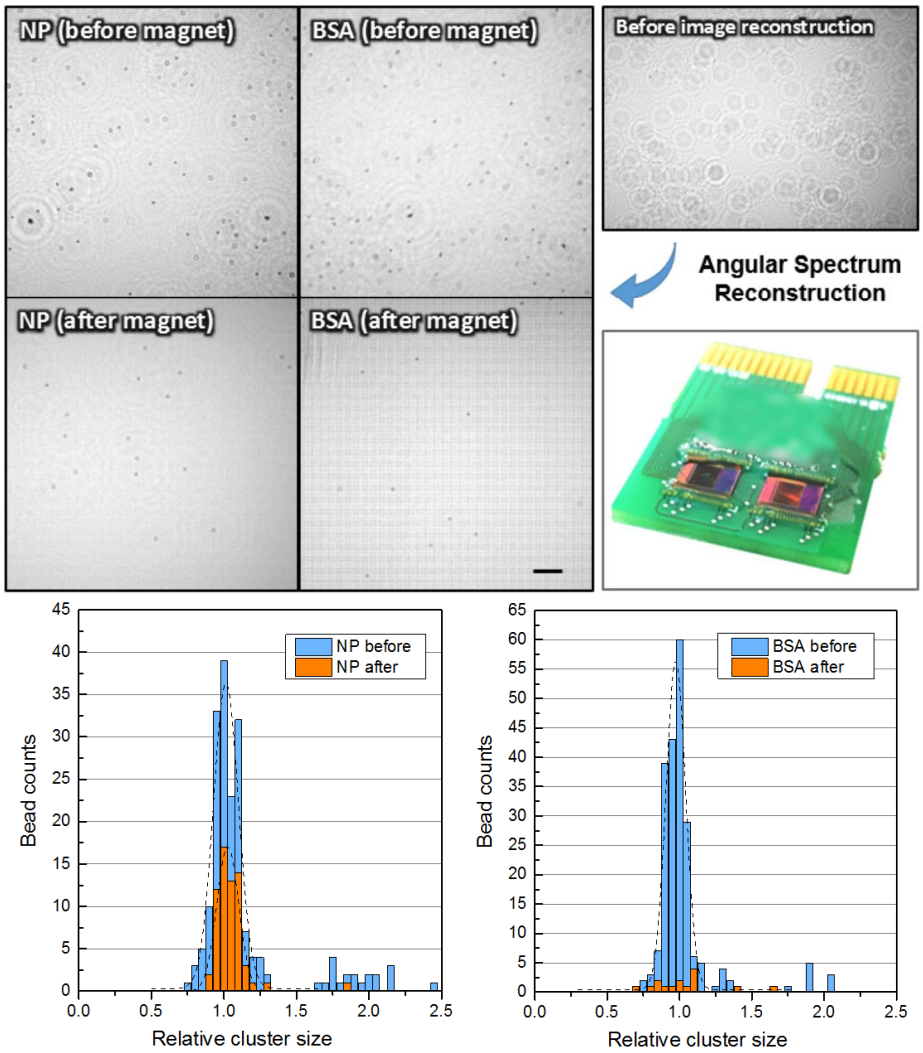

Figure 2-23. CIS measurement results. All sample images captured by the CIS were reconstructed into an original image through angular spectrum reconstruction (inverse Fourier transformation). As shown, certain target antigen produces more conjugates that survive the magnetic field after the washing step. Top: CIS images after reconstruction, Bottom: Number distribution of each sample before and after magnetic washing

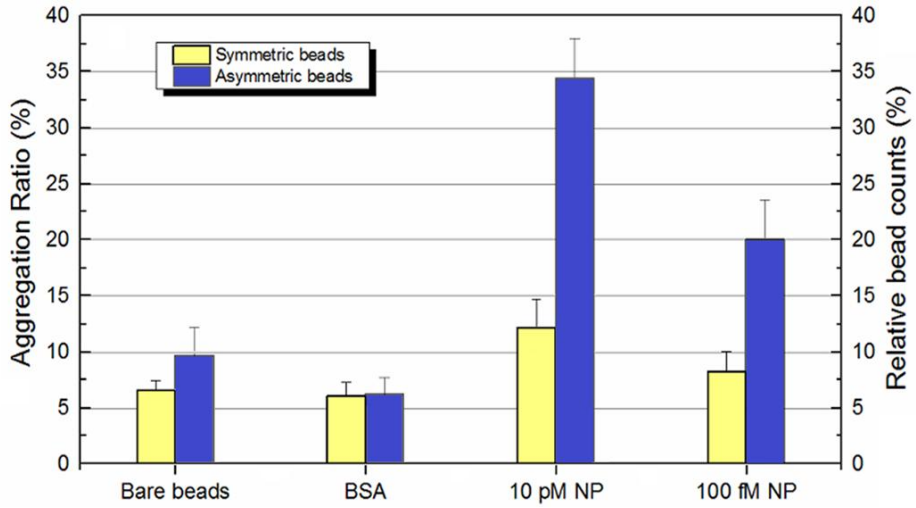

Figure 2-24. A result of the magnetic surviving assay. At higher target concentration, more conjugates were survived, resulting in higher remainder ratio. This method shows better sensing performance than conventional symmetric aggregation assay, which shows about less than a half signal of asymmetric.

Chapter 3. Microfluidic immunodetection system

The characteristics of AIP have been investigated and AIP separation method and magnetic survival method have been examined. Still, the above methods require a routine experimental process such as pipetting and manual handling. Thus, an automated, rapid sensor has been developed. This sensor integrates a cylindrical magnet and syringe pump with a microfluidic channel to provide a sensitive and continuous optical detection.

3.1. Sensing principle of AIP-based microfluidic immunodetection system

Fig. 3-1 shows a schematic of microchannel-based AIP detection. The device identifies the concentration of target protein by counting the number of sliding AIPs formed in the sample solution. AIPs are formed by the asymmetric immunoaggregation of two different particles (small magnetic particles and large polystyrene particles) mediated by the target influenza A H1N1 NP. When a sample solution containing AIPs and single particles (*i.e.*, magnetic and polystyrene particles) flows through the microchannel, only the AIPs selectively "slide" at a proper velocity determined by flow and external magnetic field. This motion is captured and recorded with a microscope, and the AIP number and velocity distribution are analyzed with a custom built program code to determine the concentration of the target protein. In case of higher target protein concentration, larger number of AIPs are formed, and more sliding images would appear on the sensing window.

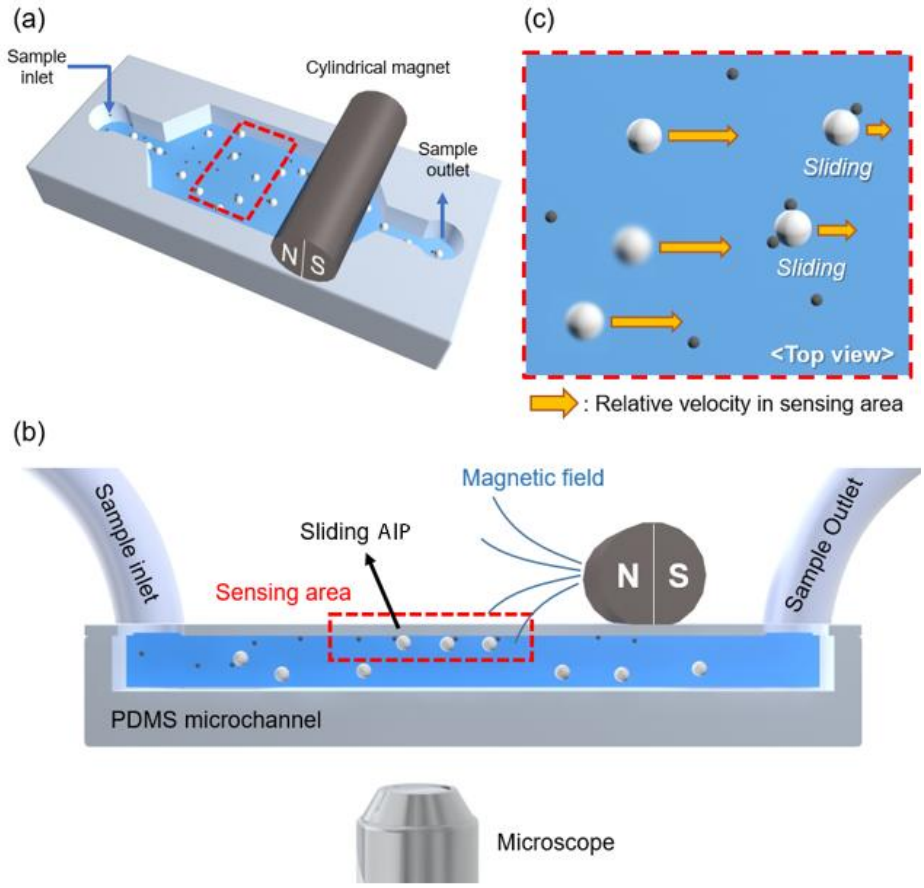
(a)
Sample inlet
Cylindrical magnet
Sample outlet
N
S
(c)
Sliding
Sliding
<Top view>
: Relative velocity in sensing area
(b)
Magnetic field
Sample inlet
Sliding AIP
Sensing area
N
S
Sample Outlet
PDMS microchannel
Microscope

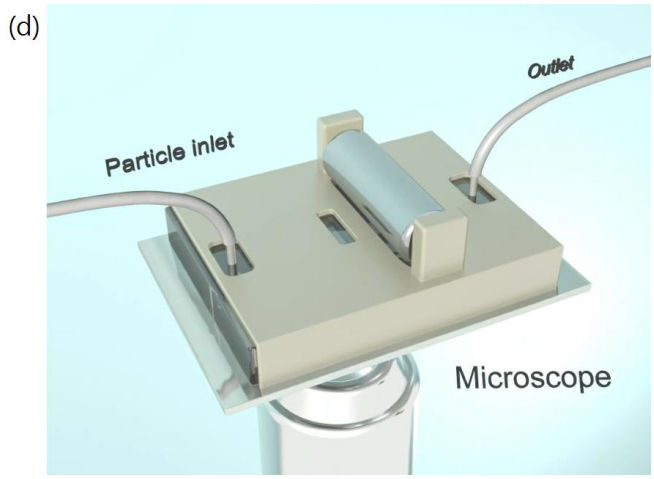
(d)
Outlet
Particle inlet
Microscope

Figure 3-1. The concept of AIP microfluidic detection. (a) AIPs are detected in a sensing area located on the top surface of a linear microchannel (red dotted rectangle). (b) A cross-sectional view of the microfluidic device. (c) AIPs slide with a reduced velocity while PS are flowing at the flow rate of carrier fluid. Note that most of the PS are out of focus in the microscope. (d) A rendered illustration of the microfluidic device. Open slit in front of the magnet indicates to the sensing window.

3.1.1 Device fabrication and system design

The microchannel was fabricated by a single-mask soft lithography process. First, an SU8 3050 (MicroChem Corp.) was spin-coated on top of a silicon wafer, followed by a photolithography step to pattern a mold of the microchannel. The thickness of the mold became the height of the microchannel. Next, PDMS (Sylgard 184, Dow Corning) was mixed with cross-linker 10:1 ratio and degassed in a vacuum chamber. The mixture was poured onto the SU8 mold and cured in an oven at 65 °C for 4 h. The cured PDMS was peeled from the mold. The inlet and outlet were made by biopsy punch with 1 mm holes at each end of the linear microchannel. The PDMS was rinsed in the ethanol and dried in a dry oven at 80 °C. Finally, the PDMS was bonded onto a slide glass by air plasma treatment for 1 min (BD-20V, ETP, USA). The microchannel has a width of 1 mm, a total length of 20 mm, and a height of 75±0.5 μm. PDMS has a thickness of 3 mm.

For a microfluidic device, a diametrically magnetized 4 mm cylindrical magnet (Grade N40, JJtool, South Korea) was mounted on top of the microchannel and a vertical distance between the magnet center and the channel was 5 mm. The magnet was arranged so that the north and south poles were parallel to the microchannel. In this configuration, a magnetic

particle (Single MG or AIP) flowing through the channel is attracted to the upper microchannel by the magnetic field and slides along the surface. In particular, due to the size and speed difference, the AIP is easily distinguished from MG. Note that the magnetic field in the y direction is almost zero ($\boldsymbol{B_y} = 0$), so that all sliding AIPs are observed through a microscope in a linear motion without deflection.

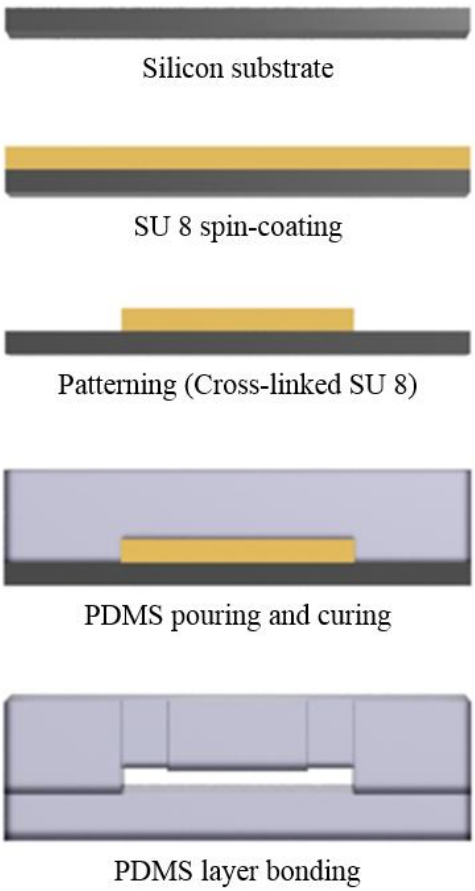

Figure 3-2. Microchannel fabrication flow

3.1.2 Testing procedure

For AIP sliding assay, PBS buffer (1% w/v BSA) was injected into the PDMS microchannel to coat the inner surface of the channel with BSA. This process minimizes the AIP adsorption on the surface while slipping. Immediately prior to testing, each sample was diluted 4-fold with PBS tween-20 (PBST 0.1%) solution to 600 μL, loaded onto a syringe (Hamilton, USA) and transferred to a microchannel with a Teflon tube. The flow rate for all tests was fixed at 1 μL/min by a syringe pump (KDS Pico syringe pump, KD scientific, USA). This is equivalent to an average flow velocity of 222 μm/s when considering the dimensions of the channel. Fig. 3-4 depicts the detailed dimensions of the actual configuration. The sensing area has a size of 1180 μm × 944 μm and is 1 mm laterally away from the external magnet. The thickness of the PDMS above the microchannel is 3 mm. A cylindrical neodymium magnet having a surface induction of 0.35 T, a diameter of 4 mm was placed on top of the microchannel. Since the north and south poles of the magnet are aligned parallel to the microchannel, surface adsorption of AIP due to magnetic field orientation is minimized. In this configuration, a magnetic particle (Single MG or AIP) flowing through the channel is attracted to the upper microchannel by the magnetic field and slides along the surface. In particular, due to the size and speed difference, the AIP is easily distinguished from MG. A 3D-printed polymer housing (DP200, Sindoh, South Korea) was engaged to the microchannel to maintain the relative position of the magnet, microchannel, and sensing area during measurement (Fig. 3-3). After applying the sample flow and the external magnetic field in the microchannel and waiting for 1 min, the number of AIPs passing through the sensing area became uniform. The sensing area was monitored under a

microscope for at least 6 min per measurement at 100× magnification (Nikon Eclipse Ti). The upper surface of the microchannel was focused during the measurement. The microscope shutter exposure time was set to 1 ms and brightness was adjusted for a clear distinction of objects. The width of the sensing area (944 μm) in contrast with the full width (1 mm) was chosen to clearly distinguish most of the AIP passing through the sensing area. The channel height was optimized for clear discrimination of AIPs and good image quality. A shallow channel can induce large velocity gradient in the vicinity of the upper surface for marked motion of AIPs in contrast with other particles. If the height becomes too small, however, the image of PS particles that travel near the microscopic depth of field may frequently interfere with the AIP counting.

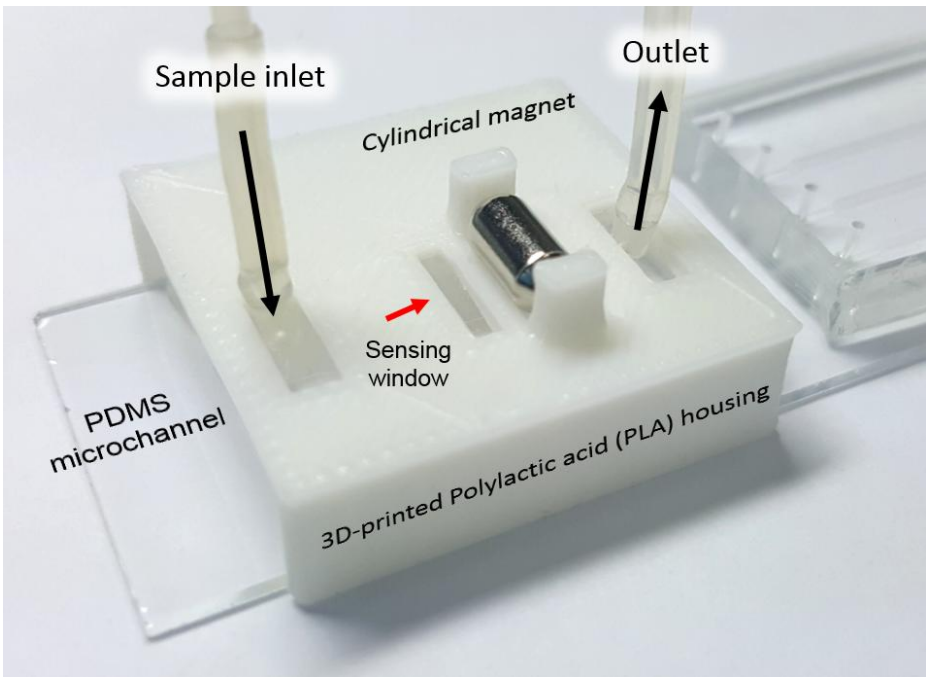

Figure 3-3. Image of the microfluidic device

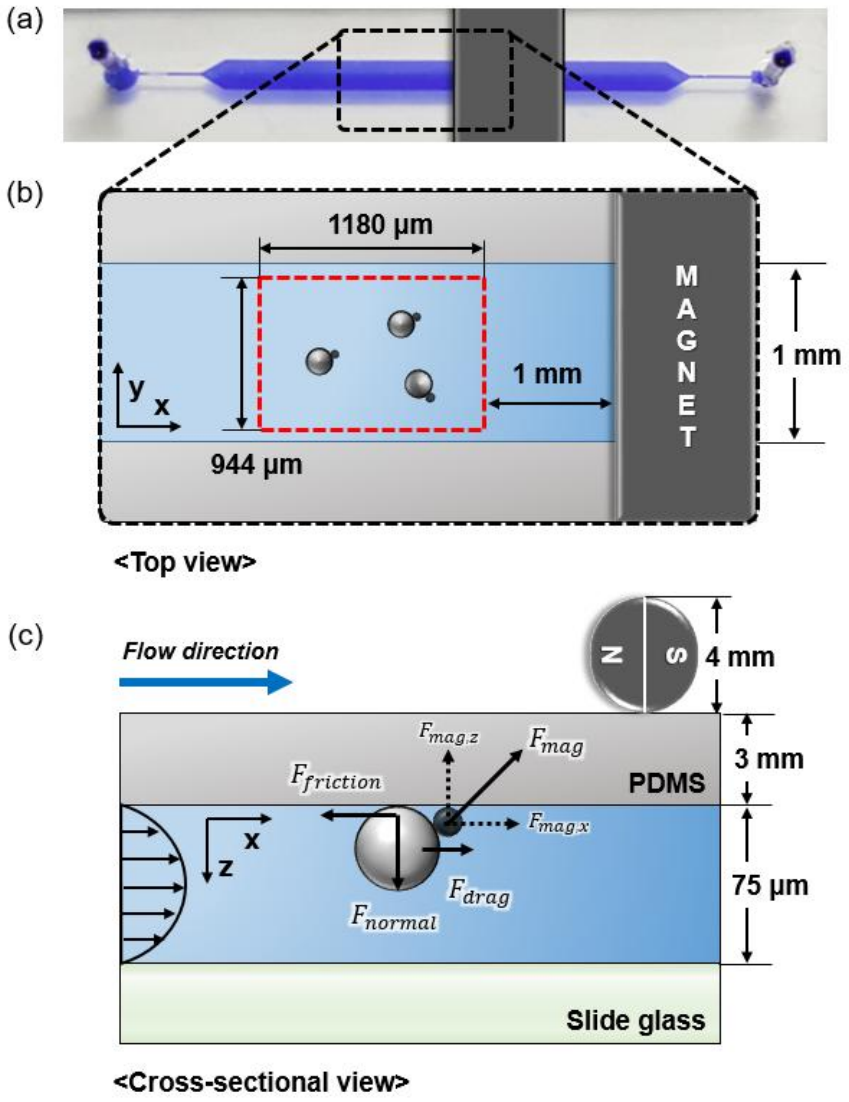

Figure 3-4. Dimensions of microchannel sensing device. (a) Image of the microchannel. (b) Dimensions of sensing area, microchannel, and magnet (top view). (c) Various forces applied to the AIP during sliding and dimensions of the magnet and the microchannel (cross-sectional view) Gravitational and buoyancy force are negligible here (F_g = ~0.01 pN).

3.2 Video frame analysis

The video of sliding AIPs was recorded through a microscope and analyzed using a custom built software (MATLAB R2016b, Mathworks®). The video was recorded at 24 frames per second with a size of 840 by 672 pixels (1.40 μm/pixel). The video was divided into frames and converted to grayscale image, and each object in the image was recognized according to the gray scale value. Every frame was compared with the following frame after 1/8 second to calculate the travel distance of each AIP. Then, the number of AIPs in motion and their respective velocities were calculated. The size of a single PS particle is 2.8 μm (the corresponding area is 6.15 μm^2) and occupies roughly 3 to 5 pixels on the image frame. Therefore, an AIP, an aggregate of 1.05 μm and 2.8 μm particles, has a size distribution of approximately 4 to 18 pixels when considering the sliding orientation, degree of multiple aggregations, and focusing error of the microscope on the channel inner surface. The size exceeding 20 pixels was regarded as non-specific aggregate or impurity and ignored. Objects smaller than 3 pixels were regarded as single MG and neglected as well. The immobile AIPs were considered as adsorbed ones and were not considered in the calculation from that moment. This adsorption occurred on the average of 1-3 in the sensing area per min for all samples. Also, since fast objects cannot be AIPs, objects over half the average flow velocity were ignored.

3.2.1 Data acquisition from video frames

Fig. 3-5 shows how AIP are selectively captured on a frame image. As an example, an image obtained by superimposing 24 frames (1 second) is shown in Fig. 3-5a. The sliding AIP has a velocity range of approximately 1/10 of the

mean flow velocity of the microchannel, leaving a short rod-shaped trace. The length of the bar represents the velocity of the individual sliding AIP. As most PS particles move out of focus, a few of them might move near the channel surface and could be recognized as the AIP. However, since the velocity of PS particle is significantly higher than that of AIP, they can be readily distinguished from AIP. In case of single MG as well, they were moving far slowly across the microchannel after being attracted to the external magnetic field, resulting in no significant interference with the sliding AIP in the sensing area. Fig. 3-5b shows the appearance probability of AIP along with the longitudinal position of the sensing region for 6 min. Given the short measurement times and the natural disturbances caused by data acquisition noise, they are distributed evenly over time. The number of AIP counts per 3 frames (1/8 second) is shown in Fig. 3-5c. Due to the fluctuation of AIP recognition in individual frame images, the data was averaged every 2 seconds before statistical analysis. The number of particles counted is generally constant over time. This indicates that the number of sliding AIP visible at certain point is representative of the formation fraction of AIP among the particles probe.

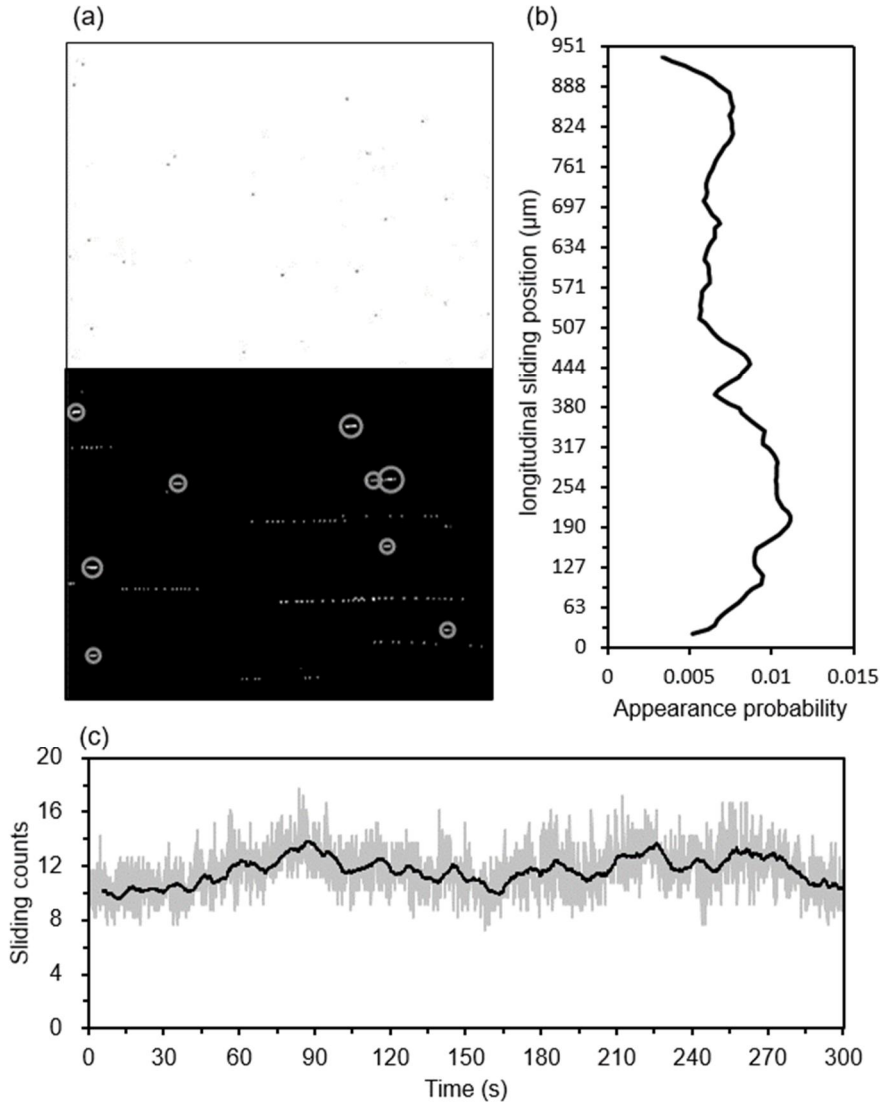

Figure 3-5. MATLAB video frame analysis. (a) Microscopic image of sliding AIP inside sensing area (top) and corresponding image converted to monochrome, with trajectory accumulated for 1 second; Each slipping AIP was marked with a circle (bottom). (b) Appearance probability of AIP by longitudinal position. (c) The number of sliding AIPs detected in the sensing area every 3 frames (1/8 second, Grey line: raw data, Black line: filtered data, @ 5.4 ng/mL NP).

3.2.2 Sliding velocity calculation

The AIPs that slid in the sensing area were recorded as videos and analyzed in custom-built MATLAB software. A simple form of velocity analysis algorithm was used to track the individual velocity of AIPs. In our system, relatively small numbers (0 to 200) of AIPs are observed in the sensing area and the speed of individual aggregates is relatively slow on the moving image (taking about 1 min to traverse the window) The particle velocimetry was performed on the assumption that the intervals of AIPs are moderately long.

First, when n AIPs on a frame are observed at arbitrary time t of the recorded video, each is called $AIB_1, AIB_2, \cdots, AIB_n$ and the coordinates in the sensing area are $(x_1(t), y_1(t))$, $(x_2(t), y_2(t))$, $\cdots$, $(x_n(t), y_n(t))$. The coordinates of n AIPs are called $(x_1(t+\Delta t), y_1(t+\Delta t))$, $(x_2(t+\Delta t), y_2(t+\Delta t)), \cdots$, $(x_n(t+\Delta t), y_n(t+\Delta t))$ in the same way in frames taken after Δt seconds. (Suppose there are no introduced or escaped AIPs in the sensing area.) At this time, the moving distance of each AIP is expressed as $\left|(x_k(t), y_k(t)) - (x_k(t+\Delta t), y_k(t+\Delta t))\right|$ (Where k is from 1 to n). However, since the correspondence relation between the AIPs recognized in each frame is not known, it is necessary to estimate by using the distance analysis. The distance of each n AIPs between t and $t+\Delta t$ is represented by n by n matrix, and is taken as the moving distance of each AIP during Δt, where n is the smallest component. Normally, each AIP moves very little in neighboring frame comparisons, so the diagonal matrix of n by n is the distance traveled during Δt of each AIP itself. Through this diagonal matrix we can see how many AIPs have moved at what speed. We set Δt to 1/8

second (3 frames) in our program. If the searching is performed at shorter interval, the error becomes large due to the pixel limit of a travel distance of AIP. If the searching is performed at a longer time interval, the movement distance becomes larger and may be interfered by nearby AIPs.

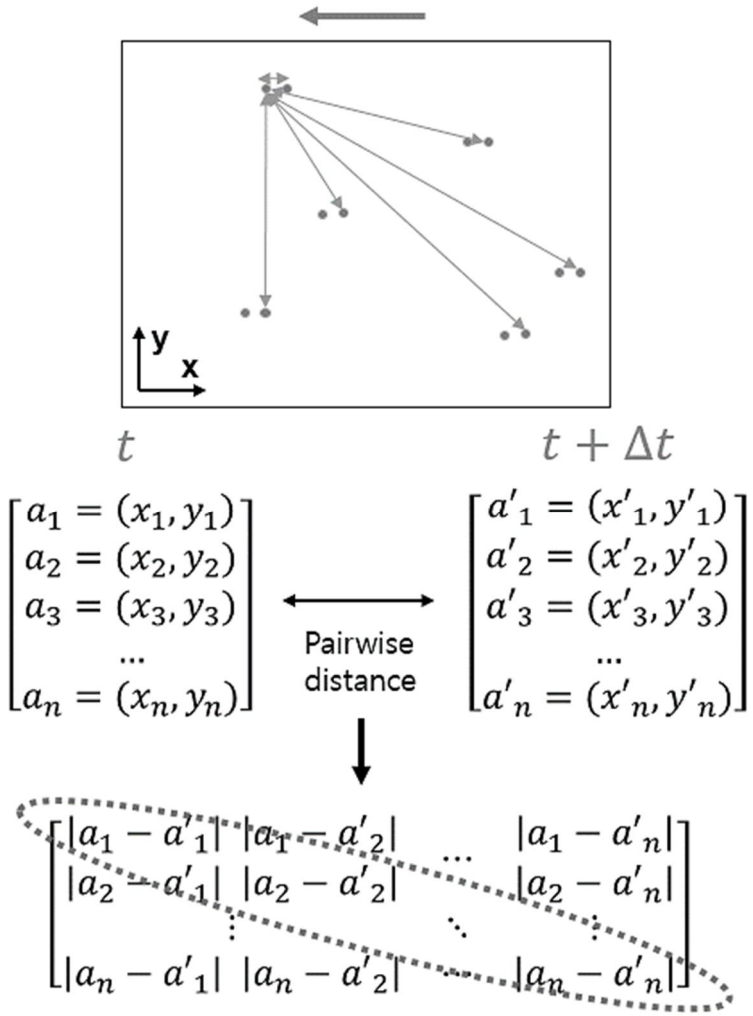

Figure 3-6. AIP travel distance calculation; A matrix representing all distances between neighboring AIPs in adjacent frames is obtained, where the diagonal matrix represents the travel distance of each AIP.

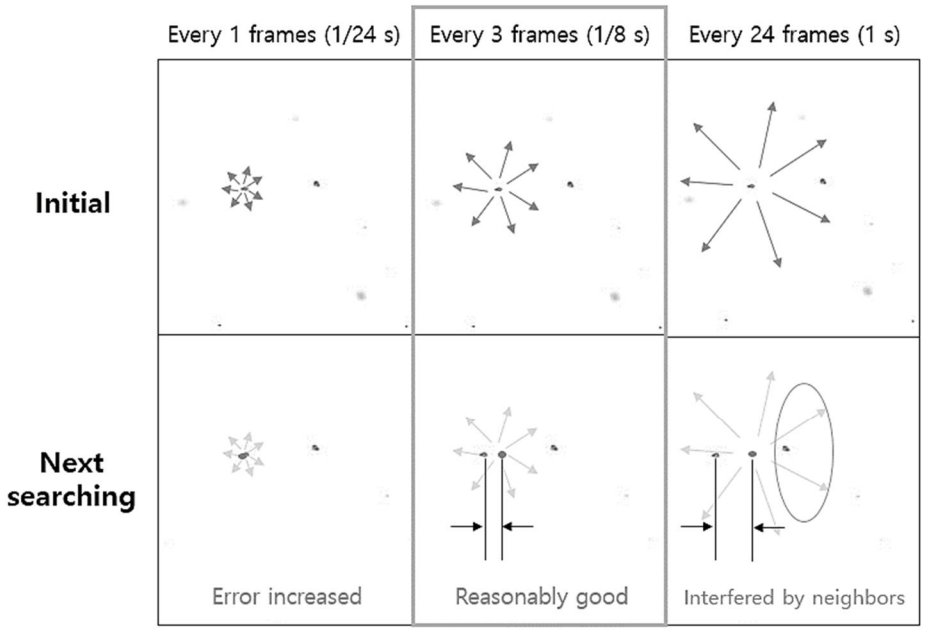

	1	2	3	4	5	6
1	0	284.5174	311.7316	81.8184	93.8055	325.1812
2	286.9899	7.9905	43.6344	251.8663	256.7026	323.4671
3	312.5737	37.0408	4	268.4125	271.2481	305.7930
4	78.3389	244.2402	264.1734	5.8832	19.9899	248.3719
5	90.9480	249.4103	267.3110	10.2659	4.2576	234.4525
6	325.1812	315.5406	301.9141	244.0639	231.4162	0

Figure 3-7. The accuracy of individual AIP velocity calculations depends on how long the frame interval is chosen. When consecutive frames were compared, the error increased due to local pixel resolution limit in short time interval. When comparing longer interval frames, the velocity measurement may be interfered by nearby AIP. The bottom table indicates an example of travel distance acquisition (diagonal elements).

3.3 Sliding AIP counts

First, we used our system for detecting influenza A H1N1 NP as antigen in PBS containing 0.1% w/v BSA. Through video frame analysis, we examined how many AIPs were formed by each target NP concentration in the microchannel. Fig. 3-8 shows representative images for several concentrations; in particular, the randomly sliding AIP, to which size and the number are increased along the target concentration, can be observed. The number of sliding AIP captured in a certain frame indicates target concentration. This method can be applied for the yes/no detection of moderate concentration target in a single shot monitoring.

Since the number of AIPs detected at relatively low concentrations (0 to 0.54 ng/mL) was about 0-15, only one AIP counting deviation could affect the statistics. Therefore, sufficient time and repetition were required for accurate detection at lower concentration. Considering the average speed of the AIP (~17 μm/s), it takes about 1 min for the AIP to pass the sensing area on average, implying that a new AIP will flow into and out into the window every 1 min. In repeated tests, we found that this trend was maintained consistently. The dynamic range from 54 pg/mL to 54 ng/mL (1000 folds) was tested, thus, capable of measuring from pico- to nanomolar concentrations, considering the molecular weight of the nucleoprotein (56.6 kDa). The reason for setting the maximum concentration to 54 ng/mL is that it is the optimal aggregation range for our “tuned” probe particle concentration and the approximate boundary point that accurately counts the sliding AIP in the sensing area. We observed that when the target NP concentration was too high, AIP surface adhesion occurred more frequently due to unbound free NP

in the solution. For all concentration ranges, there was no case of disintegration or change of shape while the AIP was sliding.

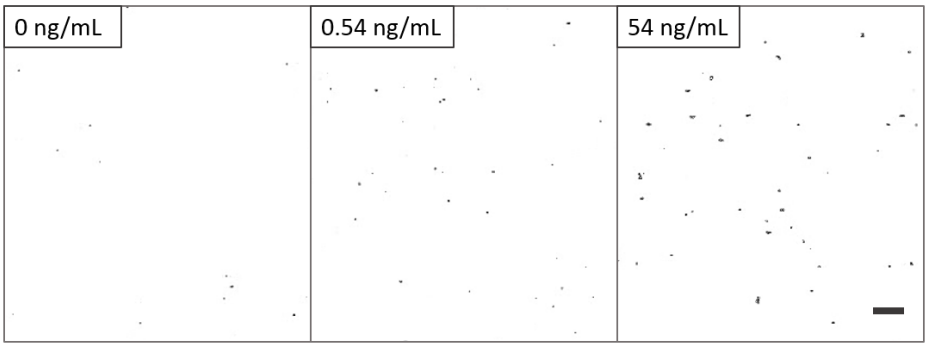

Figure 3-8. Sliding AIP captured in the sensing area. More and larger AIPs were formed in the solution and captured in the sensing area as the target NP concentration increased (scale bar: 20 μm).

3.3.1 Sliding speed for each AIP type

In order to comprehensively understand the movement of the AIPs observed in the device, individual sliding velocities were measured by classifying AIP by shape. The friction force and the attraction force on the MG in AIPs are theoretically always the same, so that even if the AIP contains several MGs, the friction force and the attraction forces are canceled each other. With this configuration, individual AIPs can be distinguished by their size.

An example of tracked velocity of actual AIPs is shown in Fig. 3-9. Multiple aggregates were observed faster in sliding due to their larger size (they experience fast flow speed from surrounding flow), while smaller AIPs were found to have a relatively slower speed. Interestingly, PS-2MG and PS-MG showed a certain difference in speed even though they are quite similar in

effective diameter and the additional MG inside the aggregate plays no role in sliding velocity even though the magnetic strength had been increased. In the case of single MG, they roll on the surface rather than a slide with friction. Fig. 3-10 shows the matching of the actual velocities and theoretical velocities of the individual AIPs measured in the sensing area. It can be seen that the theoretical velocity (velocity near the wall surface) matches to the velocity of the individual aggregates.

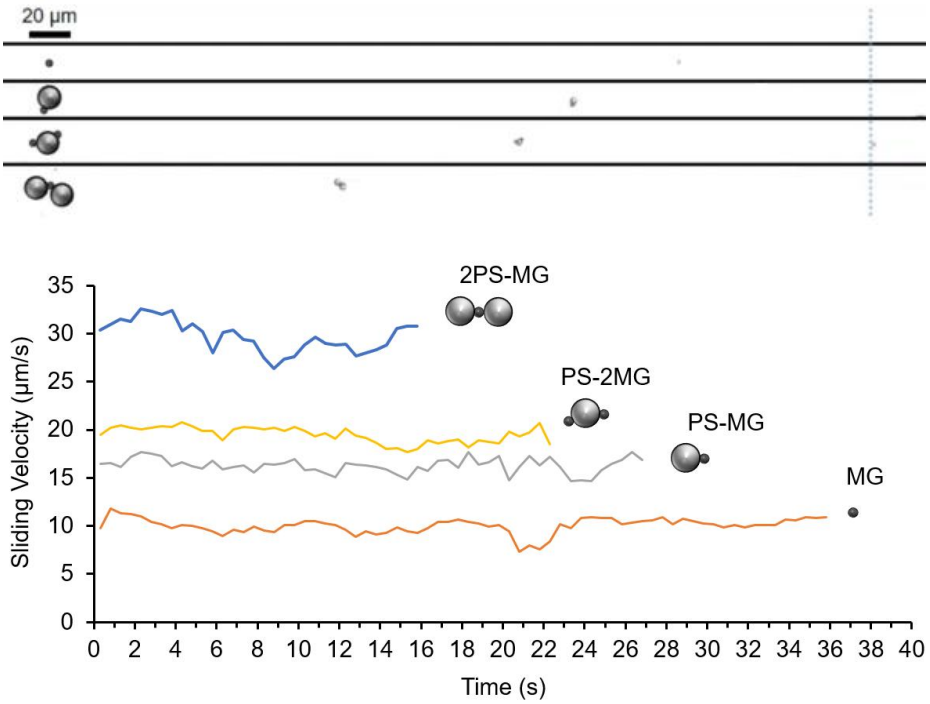

Figure 3-9. Individual sliding velocity of AIP by aggregation degree in local monitoring; each AIP moves from right side to left side (top), time-dependent velocity of each type in the sample (down).

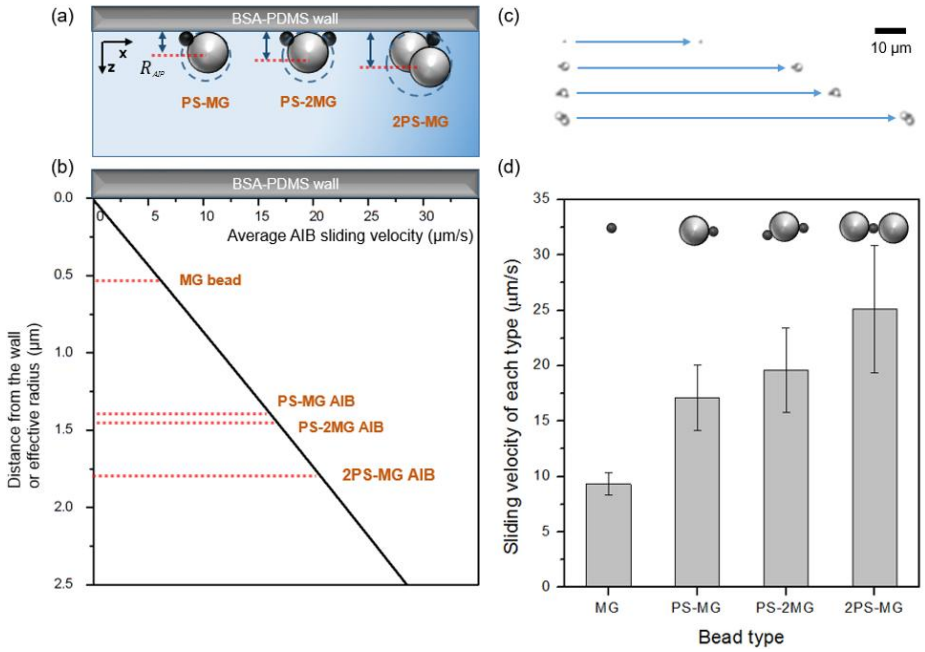

Figure 3-10. Various types of AIP that were frequently observed in the sensing area. (a) Schematic of effective radius and distance from the wall of various AIPs. (b) Flow velocity profile near the microchannel wall and estimated AIP velocity based on the effective radius. (c) Sliding distance of each AIP for 5 seconds at 200X magnification observation. (d) Actual velocity for each AIP monitored in the sensing area. 10~30 AIPs were measured, respectively.

3.3.2 AIP velocity distribution and limit of detection of NP

In our configuration, the attraction and friction forces applied to the AIP in the flow direction induced by external magnet cancel out. The role of the external magnetic field is to bring the AIP near the upper surface. Fig. 3-11 shows the velocity distribution of AIP at each concentration. As a result of monitoring all velocities of AIP detected in the frames for 6 min, area under the curve of each concentration represents the total number of sliding AIPs. In Fig. 3-11b, the average sliding velocity increases gradually, indicating that the average AIP size also increases with NP concentration. This result is in good agreement with previous particle characterizations. On average, the AIP formed by a single PS-MG bond is 1.42 μm. At the NP concentration of 54 pg/mL, most of the AIP (> 97%) consist of only a single PS-MG binding. On the other hand, the ratio of single PS-MG to total AIP is reduced to ~70% at 54 ng/mL (The effective radius of 2PS-MG AIP is 1.8 μm). The total number of AIPs that pass through the sensing area per unit time (N_{pass}) can be derived from the average number of AIPs sliding in each frame with their velocity:

$$N_{pass}(t) = \frac{\overline{v_{AIB}}\overline{N_{AIB}}t}{L_s} \tag{3-1}$$

Where $\overline{N_{AIB}}$ is the average number of AIPs visible at a given concentration, t is measurement time, and L_s is the length of the sensing area of 1180 μm. Fig. 3-12 shows the difference between the number of AIPs that passed through the sensing area for 6 min and the number of AIPs that passed through the same time when the concentration was zero. The data points represent the

mean of 3-4 replicates with error bars standard deviation (SD). The linear fit to these data points with a coefficient of determination (r^2) is also shown as a solid line. In this log-log plot, the limit of detection (LOD) signal is taken as three times SD of background signal. The intersection of the linear fit and the LOD signal represents the LOD concentration.[22, 60] In this way, the minimum detection limit of our device was determined to be 40 pg/mL for NP in PBS solution containing BSA 0.1% w/v. The maximum detection limit tested was 54 ng/mL since the calibration curve is no longer linear after reaching this concentration. This strong nonlinearity occurs because individual particles lose their binding capability due to excessive target antigen in the solution.[23, 30] Reducing non-specific signal is crucial for improving sensing performance.

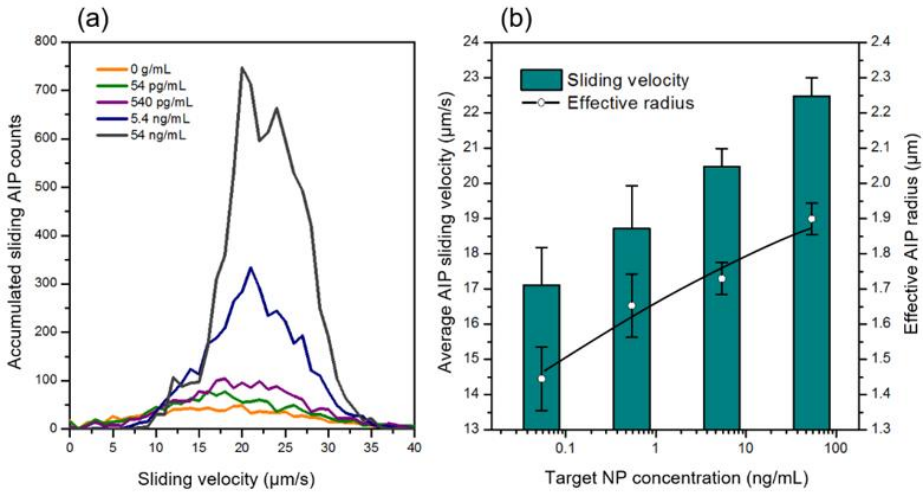

Figure 3-11. Velocity distribution of sliding AIP for 6 min recording. (a) Accumulated sliding AIP counts captured in the sensing area for various target NP concentration (Velocity was weighted by the AIP number every 3

frames (1/8 second)). (b) Mean AIP velocity for each NP concentration and the effective radius derived therefrom (3 different tests).

We used various measures to make our sensing consistent. The sensing area covers an area of 1.1 mm^2, so that it can hold up to ~100 sliding AIPs per frame, resulting in relatively uniform counting. We also measured 6 min for each test to reduce noise while ensuring statistical consistency. The sample was diluted 4 times right before injecting into the microchannel, allowing the particles to flow with sufficient spacing without interference. During the measurement interval under flow, a total of approximately 6,500 PS particles (including AIP) should pass through the microchannel, of which 10 to 300 AIPs slide in the sensing area.

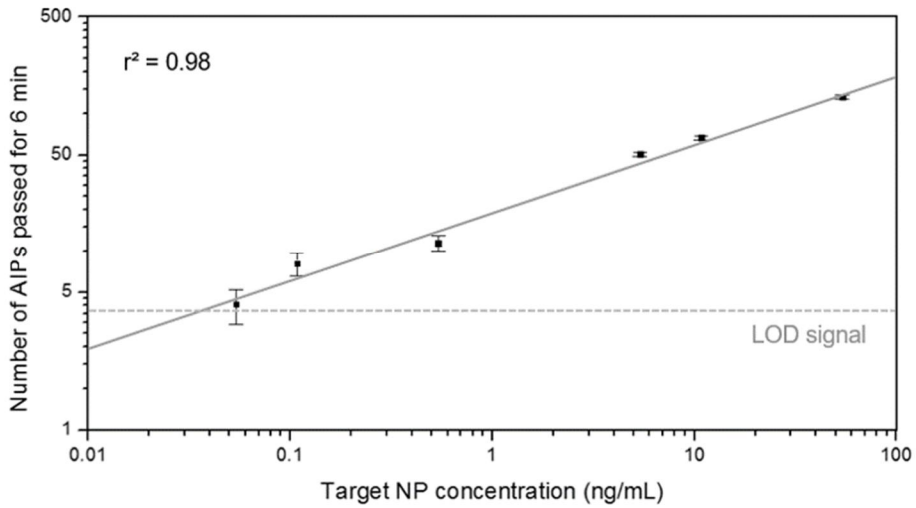

Figure 3-12. Log-log plot of the difference in the number of sliding AIP that pass through the sensing area for 6 min with respect to the background (zero NP concentration) as a function of different concentrations of nucleoprotein as antigen in PBS (BSA 0.1% w/v).

Our proposed AIP method has a higher aggregation sensitivity than the well-known same-sized particle aggregation method.[23, 25] Previous methods suffered from the non-specific aggregation of around ~5% in the absence of antigen, and the detection limit was relatively high.[10] On the other hand, in our case, since the particle size is asymmetric, the probability of inter-particle collision increases during incubation, and provides lower detection limit. The non-specific aggregation ratio was 2.47±0.59% in the absence of NP. NP may contribute to the symmetric aggregation of PS-PS during the assay. However, only limited number of such aggregates could be observed (Fig. 3-12). Moreover, the symmetric aggregation of PS-PS and MG-MG were excluded from all observations in the sensing process. Independent characterization of particle aggregation in previous section shows a good agreement with sensing result in Fig. 3-12.

Although the sensing is separated into two steps (the particle immunoassay and sliding test), integrating into one system is plausible by several other methods.[29] For example, a collision between the PS and MG particles can be induced through a rapidly disturbing electromagnet in a separate chamber for AIP assay. The AIP can then be transported to a linear microchannel for sliding analysis. Detection time is less than 10 min, much shorter than required for other particle characterization methods.[23-25, 30, 31] Our system can monitor multiple AIPs in a parallel fashion, resulting in a quick quantitative analysis without high speed optics. Such performance is enabled without complex electrical systems and fast data acquisition that can simply characterize single particle or an aggregate at a time. Since only aggregates are selectively and magnetically picked up, the structure and testing steps can be further simplified. The flow system can be easily divided into reaction

phase and capillary driven step similar to conventional lateral flow assay. Our device can be fabricated through a single-step molding with a simple structure and integrated with various functional compartments. For example, a microscope-free portable sensor can be an option with a CMOS image sensor, because the used microscope magnification is not high (only 100×) and does not require sensitive pixel counting.

3.4 System miniaturization with CMOS image sensor

So far we have shown and discussed about the principles and detection results of our system. The microfluidic devices enable quantitative immunoassay with particle velocity analysis. Now, in order to miniaturize the system, an attempt has been made to replace the microscope with a compact image sensor. Because our immune sensing is optically accomplished through a microscope, miniaturization of the optical system will be an indispensable requirement for future POC systems. Fortunately, the magnification of the microscope used for optical sensing is low, so we have developed a sensing system that utilizes inexpensive, cheap commercial CMOS image sensors (CIS, less than ~50 USD in price). In this case, unlike the previous system, the lens should be integrated because it guarantees around 100X magnification accuracy. The lens-coupled sensor provides a magnification and sensing area comparable to that of a microscope (Nikon Eclipse TI). Fig. 3-13 shows the sensor configuration with CIS replaced. Samples were supplied through microchannel and syringe pumps, effectively applying a local blue LED light source to obtain clear images and it was possible to distinguish 1 μm particles. For measuring moving particles, the system provides 2~3 FPS (frame per second) capture rate and allow us to measure travel distance of each AIP as

the similar way with microscope. Since the AIP has a speed of around 20 μm/s, a lateral movement should be 6 ~ 10 μm is each observed frame, which is a relatively narrow moving distance eligible to analyze. Therefore, in the case of preliminary test, the CIS microfluidic device showed satisfied sensing results. Further optimization of the image sensor and systems are worth to develop a finalized system in relation to the POC application and is a highly realizable part. It is also expected that the total volume of devices will be reduced.

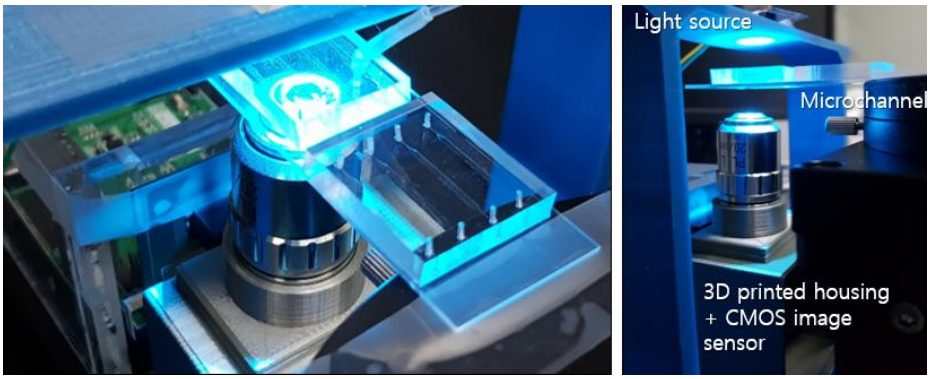

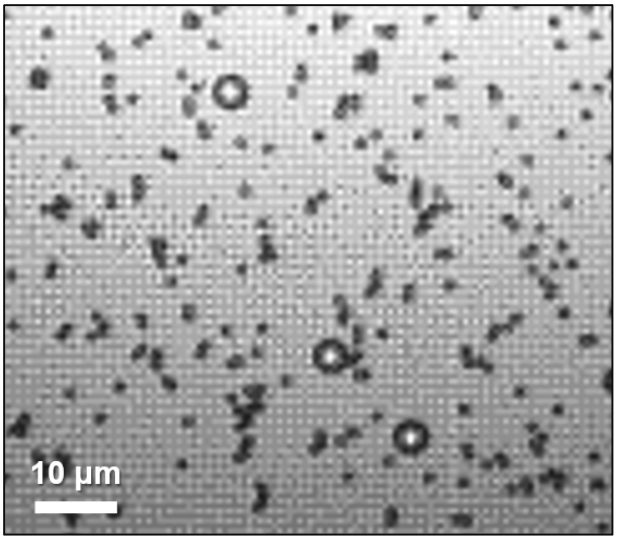

Figure 3-13. CMOS image sensor integrated sensing system (Top), A measurement result of particle mixture (1 + 4.3 μm) as an example (bottom).

3.5 Multiplexed immunoassay and system compatibleness

Developed rapid sensing device does not require antibody-patterned microchannel chips and can therefore be considered "Chipless" systems. This feature ensures that the system is compatible with other devices. The material of the microchannel is not limited to PDMS, so it can be made of plastic or other flexible (even disposable) material. In addition, only one sample flow is required for sliding analysis, so only single syringe pump is enough. This is a major advantage in simplifying the overall system. Detection of our system can be accomplished by mixing the lysis buffer with a random virus sample and then blending the two particles into a mixed probe particle solution. The structure of the proposed system can be implemented for real viruses, so called 'mix-and-read' system.

Multiple detection is also possible by introducing fluorescent or colored particles or introducing new particles (large particles) as independent one (Fig. 3-14). Specifically, each non-magnetic particle (PS) is labeled with an independent color, and then the assay is performed by binding different antibodies, so that the presence of the corresponding antigen can be quantitatively detected in any solution. If asymmetric aggregation is induced for any antigen ‘X’ and then the aggregate is classified and counted at the top of the microchannel, it can be converted to the corresponding antigen concentration according to the above-described method. This leaves the basic principle of not labeling, but it can be an effective strategy for widening the area as an easy-to-use sensor in the actual field. In addition, an external electromagnet can be introduced to accelerate mixing for more practical & tunable system.

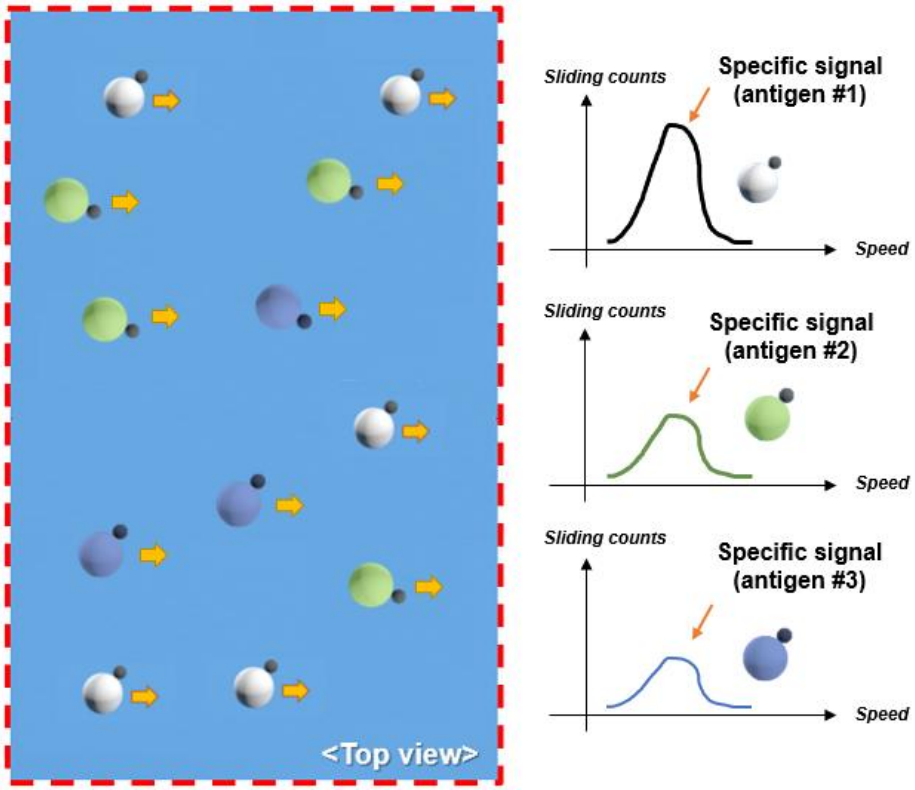

Figure 3-14. Multiplexed immunodetection method using various color particles. Each particle corresponds to different target analyte. Depending upon the amount of specific analyte concentration, one can easily count the sliding AIPs and correlate with target concentration.

Chapter 4. Motion of AIP in a flow

Transport of MP and PS in water (buffer) or ferrofluid has been extensively studied in terms of relative magneto susceptibility under various experimental conditions.[61-69] The difference in the relative magneto susceptibility between the solution and the particle is the main factor that governs particle motion. In this section, the force acting on the AIP under an external magnetic field in the proposed microchannel system is analyzed based on the movement of the AIP. This gives a comprehensive understanding of how the AIP floats and slides in the microchannel.

4.1 Forces acting on an AIP

4.1.1 Magnetic force

Since the AIP is composed of MG and PS, AIP receives magnetic force by external magnetic field. The magnetic force applying on the AIP is equal to that of MG and expressed as[70, 71]

$$\boldsymbol{F_{mag}} = (\boldsymbol{m} \cdot \boldsymbol{\nabla})\boldsymbol{B} \tag{4-1}$$

Where $\boldsymbol{m}$ is the magnetic dipole moment of the MG. Since the carrier fluid is non-magnetic PBS (0.1% w/v BSA) buffer with the negligible magnetic susceptibility, the magnetic dipole moment can be expressed as $\boldsymbol{m} = V\boldsymbol{M} = V\chi\boldsymbol{H}$. Where V is the volume of the magnetic particle. χ is the effective magnetic susceptibility, which is 0.3 from another independent study.[72, 73] $\boldsymbol{B}$ is the magnetic flux density and can be written as $\boldsymbol{B} = \mu_0\boldsymbol{H}$, where $\boldsymbol{H}$ is the

magnetic field and μ_0 is the magnetic permeability constant of 1.26×10^{-6} N/A^2. Thus, the magnetic force can be written as

$$\boldsymbol{F_{mag}} = \mu_0 V \chi (\boldsymbol{H} \cdot \boldsymbol{\nabla}) \boldsymbol{H} \tag{4-2}$$

In our system, the magnet is cylindrical and radially magnetized. Since the magnet is assumed to be infinitely long in the y direction, the magnetic field only applies to the x-z plane. Using Cartesian coordinate system, the magnetic force along the flow direction can be expressed as

$$F_{mag,x} = \mu_0 V \chi [H_x(x,z) \frac{\partial H_x(x,z)}{\partial x} + H_z(x,z) \frac{\partial H_x(x,z)}{\partial z}] \tag{4-3}$$

And the perpendicular component can be similarly expressed as

$$F_{mag,z} = \mu_0 V \chi [H_x(x,z) \frac{\partial H_z(x,z)}{\partial x} + H_z(x,z) \frac{\partial H_z(x,z)}{\partial z}] \tag{4-4}$$

For magnetic magnetized level of M_s through radial direction, the field components can be written in the cylindrical coordinate as

$$H_r(r,\phi) = \frac{M_s}{2} \frac{R_{mag}^2}{r^2} \cos(\phi) \tag{4-5}$$

$$H_\phi(r,\phi) = \frac{M_s}{2} \frac{R_{mag}^2}{r^2} \sin(\phi) \tag{4-6}$$

Where R_{mag} is a radius of the cylindrical magnet. r and ϕ are radius and angle in cylindrical coordinate. By converting the field components to Cartesian coordinates and substitute into magnetic force eqn (4-5,6), the magnetic force on the AIP finally expressed as

$$F_{mag,x}(x,z) = \mu_0 V \chi M_s^2 R_{mag}^4 \frac{x}{2[x^2+z^2]^3} \tag{4-7}$$

$$F_{mag,z}(x,z) = \mu_0 V \chi M_s^2 R_{mag}^4 \frac{z}{2[x^2+z^2]^3} \tag{4-8}$$

x and z is the distance from the center of the magnet in the x and z direction, respectively. Note that this is a general equation of magnetic field for a single-bonded AIP.

4.1.2 Friction force

The frictional force is a force that a particle that slides on a wall receives from the wall in a direction opposite to the direction of travel. This force is expressed as follows for a particle that slides in proportion to the perpendicular drag between the particle and the wall:

$$F_{friction} = \mu_k F_{normal} \tag{4-9}$$

Where μ_k is a friction coefficient of moving object. In our system, the vertical drag is mainly due to the magnetic force.

$$F_{friction}(x,z) = \mu_k \mu_0 V \chi M_s^2 R_{mag}^4 \frac{z}{2[x^2+z^2]^3} \tag{4-10}$$

Where $F_{friction}$ is the vertical force the particle receives and x and z are the x and z distances from the center of the cylinder.

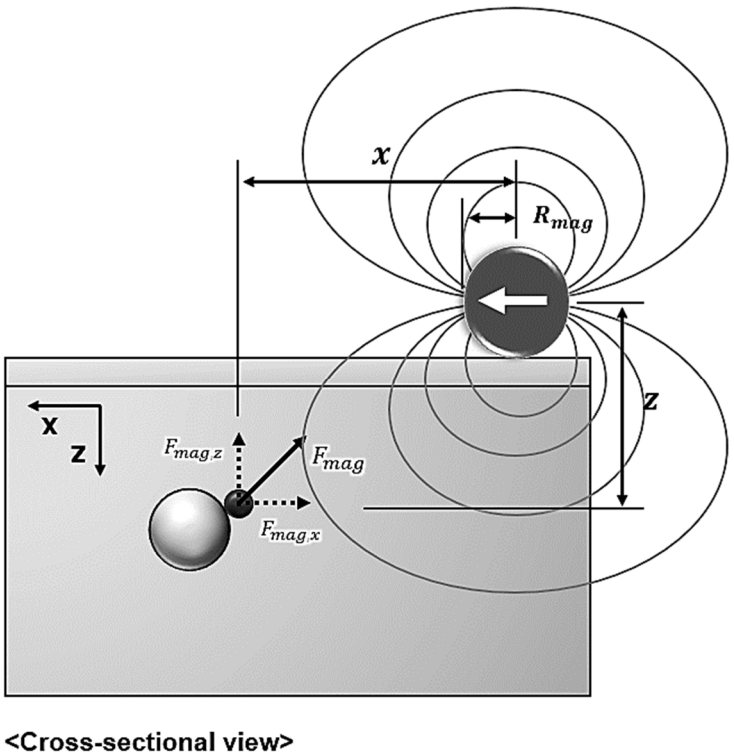

Figure 4-1. Schematic of sliding AIP with magnetic field around a cylindrical magnet.

4.1.3 Stoke's drag force

The AIP and all single particles are subjected to Stoke's drag force in the flow as they travel in microchannel laminar flow. Since the flow in our system is considered for low Reynolds number. The hydrodynamic drag force is given as[17]

$$\boldsymbol{F_{drag}} = 6\pi\eta R\Delta\boldsymbol{v}f_D \tag{4-11}$$

Where η is the viscosity of the medium surrounding particles ($\eta = 8.9 \times 10^{-4}\ N\ s/m^2$ for water). R is radius of the particles. $\Delta\boldsymbol{v}$ is velocity difference between the particles and surrounding liquid. f_D is the drag coefficient of the particle and incorporates the influence of a microchannel wall near the moving particles and is estimated by

$$f_D = \left[1 - \frac{9}{16}\left(\frac{R}{R+z_s}\right) + \frac{1}{8}\left(\frac{R}{R+z_s}\right)^3 - \frac{45}{256}\left(\frac{R}{R+z_s}\right)^4 - \frac{1}{16}\left(\frac{R}{R+z_s}\right)^5\right]^{-1} \tag{4-12}$$

Here, z_s is the distance of the particle to the microchannel wall; in case of the particle moving closer to the wall, $f_D \approx 3$, which means the drag force will be 3 fold greater than when no wall is in the vicinity. In case of AIP, the shape is not spherical the drag force should change with a certain factor.[74]

$$\boldsymbol{F_{drag}} = 6\pi\eta R\Delta\boldsymbol{v}f_D K \tag{4-13}$$

K is a correction factor of shape; has a value range of 1.0~1.5 depending upon the shape, aggregation degrees, and moving orientation. However, the determination of the value is intricate due to asymmetric particle size. In case of symmetric aggregation, K is approximately given as follow table

Table 4-1. Correction coefficient K [75]

Cluster Shape	Correction	Cluster Shape	Correction	Cluster Shape	Correction
oo	K = 1.12	oooo	K = 1.32	oo oo	K = 1.17
ooo	K = 1.27	ooooo	K = 1.45	o o o o o	K = 1.19
o o o	K = 1.16	oooooo	K = 1.57	oo oo oo	K = 1.17
oooooo o o	K = 1.64	ooooooo	K = 1.73		

In many cases of systems which incorporate with particular magnetic field, the magnetic force is generally opposed to the drag force and equalized so that the net force acting on the traveling particle to be zero. Thus, in a simple configuration, the velocity difference is given as follow (combining eqn 4-2 and 4-11)

$$\Delta \boldsymbol{v} = \frac{2\mu_0 \chi R^2 (\boldsymbol{H} \cdot \boldsymbol{\nabla}) \boldsymbol{H}}{9\eta f_D} \tag{4-14}$$

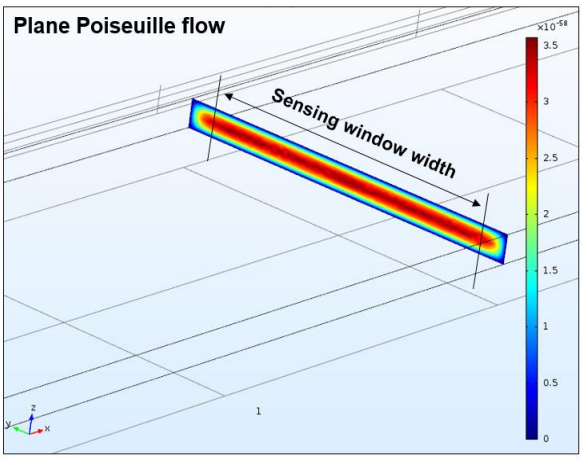

Figure 4-2. Cross-sectional flow velocity distribution in the microchannel (COMSOL Multiphysics 5.2 simulation)

4.1.4 Other forces

In addition to the magnetic and drag force, gravitational and buoyance force, electrical, and thermal force are also effective on micro and nano-sized particles. In case of the gravitational force, the net force ($F_g = F_{gravitation} - F_{buoyance}$) is given by

$$\boldsymbol{F_g} = -V(\rho_{bead} - \rho_{fluid})g\boldsymbol{e_z} \quad (4\text{-}15)$$

Where ρ_{bead} and ρ_{fluid} are the density of particle and surrounding fluid and g is gravitational acceleration. For instance, the F_g of MG (1.05 μm), PS (2.8 μm), and AIP (~2.82 μm) are given as $3.33 \times 10^{-15}\ N$, $4.51 \times 10^{-15}\ N$, and $7.83 \times 10^{-15}\ N$, respectively. All of those are in femto newton range. Considering the magnetic force of MG (Dynabead Myone; volume: 0.52 μm^3, density: 1.6 g/μm^3, 26% iron content), the force given in the microchannel device is an order of ~0.1 pN, indicating the gravitation force is much smaller and negligible. However, in the absence of external magnetic field, the gravitation force is strong enough to bring MG down and the velocity will be 0.5 μm/s as it still receives drag force.

Next, the thermal force (or Brownian force) is not generally effective for those size more than 1 μm. However, below submicron range, the force becomes dominant against magnetic and gravitational forces (those are proportional to r^3). The diffusion coefficient D of the particle is given by well-known Stokes-Einstein relation as below[76]

$$D = \frac{k_B T}{6\pi\eta R} \tag{4-16}$$

As an example, for 1 s of diffusion, MG travels an average distance of 0.7 μm.

4.2 Trajectory of an AIP inside a microchannel

In the previous section, we discussed about the various forces that can be applied to AIP in the microchannel. In this section, we estimate the velocity and trajectory of each particle/aggregate of the proposed device, and analyze sliding and rotational motion. In a microfluidic system, the particles injected into the microchannel initially float to the top of the channel due to the external magnetic field and the surrounding flow, and then slip into a linear motion along the top surface. All AIPs can appear at any z-position near the channel entrance with a differential probability. It is important to arrange the magnets appropriately in order to make all AIPs rise properly and to observe the slippage. Also, in our system, the magnetic field and the velocity are uniform with respect to the y-direction, so there is no y-direction force (the magnet is assumed to be sufficiently long through the y-direction).

At the initial stage, it can be assumed that the particles and AIP introduced along the flow are located at a medium height with high probability (because the flow profile follows the plane Poiseuille flow which is parabolic profile). The movement of AIP is determined by magnetic force, drag and gravity. When x and z are distances from the center of the cylindrical magnet to the AIP, the forces acting on the x and z components are determined as follows:

$$F_{AIP,x}(t) = F_{mag,x}(x, z) - F_{drag,x}(t) \tag{4-17}$$

$$F_{AIB,z}(t) = F_{mag,z}(x,z) - F_{drag,z}(t) - F_g \quad (4\text{-}18)$$

Where

$$F_{mag,x}(x,z) = \mu_0 V \chi M_s^2 R_{mag}^4 \frac{x}{2[x^2+z^2]^3} \quad (4\text{-}19)$$

$$F_{mag,z}(x,z) = \mu_0 V \chi M_s^2 R_{mag}^4 \frac{z}{2[x^2+z^2]^3} \quad (4\text{-}20)$$

And

$$F_{drag,x} = 6\pi\eta R_{AIP}(v_{AIP,x}(t) - v_f(z^*)) \quad (4\text{-}21)$$

$$F_{drag,z} = 6\pi\eta R_{AIP} v_{AIP,z}(t) \quad (4\text{-}22)$$

Where

$$z^* = z - R_{mag} \quad (4\text{-}23)$$

$$v_f(z) = \frac{3\overline{v_f}}{2}\left[1 - \left(\frac{h_c - z}{h_c}\right)^2\right] \quad (4\text{-}24)$$

(All constants are given in table 4-2)

While the AIP is moving, the magnetic force and the gravitation (buoyance) force become equal to the drag force; $F_{AIP,x}(t) = F_{AIP,z}(t) = 0$. Thus, the position of the AIP (x', z') at time T is determined by

$$x'(T) = x'(0) + \int_0^T v_{AIP,x}(t)\,dt \tag{4-25}$$

$$= x'(0) + \int_0^T \left[\frac{\mu_0 V \chi M_s^2 R_{mag}^4}{6\pi\eta R_{AIP}} \left(\frac{x_m - x'(t)}{2[(x_m - x'(t))^2 + (z_m - z'(t))^2]^3} \right) + v_f(z'(t)) \right] dt$$

$$z'(T) = z'(0) + \int_0^T v_{AIP,z}(t)\,dt \tag{4-26}$$

$$= z'(0) + \int_0^T \left[\frac{\mu_0 V \chi M_s^2 R_{mag}^4}{6\pi\eta R_{AIP}} \left(\frac{z_m - z'(t)}{2[(x_m - x'(t))^2 + (z_m - z'(t))^2]^3} - F_g \right) \right] dt$$

Where x_m and z_m are the distance from the center of the magnet to the edge of the starting point (10 mm and 5 mm respectively) and (x', z') is the position from the bottom edge of the microchannel (see Fig. 4-3). By applying numerical analysis (Explicit Euler method) using iterative calculation, the trajectory of AIP in the flow is estimated as Fig. 4-4a (Initial condition: $x'(0) = 0$, $z'(0)$ = 37.5 μm, $v_{AIB,x}(0)$ = 333 μm/s, $v_{AIB,z}(0) = 0$). It takes approximately 19 seconds for the AIP to reach the microchannel surface and 5.4 mm in the horizontal direction (single-bonded AIP). In most cases, AIPs successfully reach the top surface before entering the sensing area and are ready to slide. Likewise, trajectory of PS and MG particles can be estimated. A PS, on the other hand, moves almost along the sample flow due to lack of magnetism while a MG quickly reaches the surface. Fig. 4-3 shows the detailed dimensions and magnetic field applied to the microchannel. The cylindrical magnet is diametrically magnetized and is oriented along the x-axis. The numerical estimation was performed using MATLAB (R2016b,

Mathwork®). With the help of the calculations, we optimized the placement of the magnet and sensing area so that most of the AIPs are able to slide in the sensing area properly.

Table 4-2. List of constants and variables

$\boldsymbol{m_{AIP}}$	Mass of the AIP ($\mathbf{1.29 \times 10^{-14}}$ kg)
$\boldsymbol{v_{AIP}(t)}$	Velocity of the AIP at time t
$\boldsymbol{F_g}$	Gravitation force – Buoyance force (7.8×10^{-15} N)
$\boldsymbol{\mu_0}$	Magnetic permeability constant ($1.26 \times 10^{-6}\ N/A^2$)
$\boldsymbol{V}$	Volume of MG (Dynabead Myone particle, $6.06 \times 10^{-19}\ m^3$)
$\boldsymbol{\eta}$	Viscosity of water ($8.9 \times 10^{-4}\ N\ S/m^2$)
$\boldsymbol{\chi}$	Effective magnetic susceptibility of MG (Dynabead Myone particle, 0.3)
$\boldsymbol{M_s}$	Magnetized level of the cylindrical NdFeB magnet ($1.11 \times 10^6\ A/m$)
$\boldsymbol{R_{mag}}$	Radius of the magnet (2 mm)
$\boldsymbol{R_{AIP}}$	Effective radius of the AIP (1.42 μm)
$\boldsymbol{\overline{v_f}}$	Average velocity of the sample flow (222 μm/s)
$\boldsymbol{h_c}$	Half of the height of the microchannel (37.5 μm)

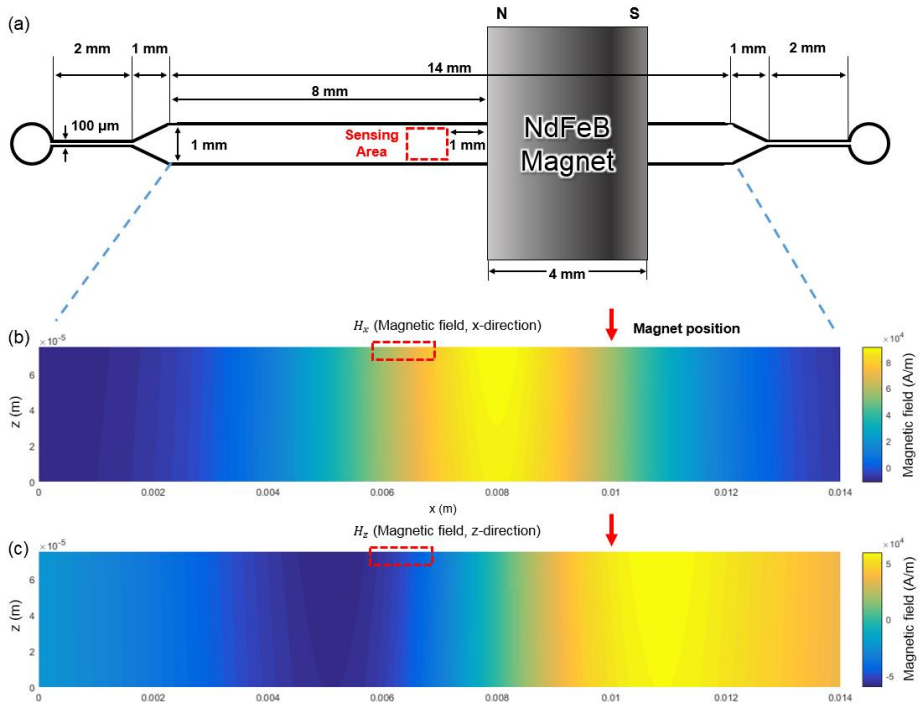

Figure 4-3. (a) Detailed dimensions of the microfluidic channel and position of the cylindrical magnet (top view). (b) The x-component and (c) z-component of the estimated magnetic field inside the microchannel (cross-sectional view). Red dotted boxes indicate the sensing area and red arrow indicates the center of the magnet.

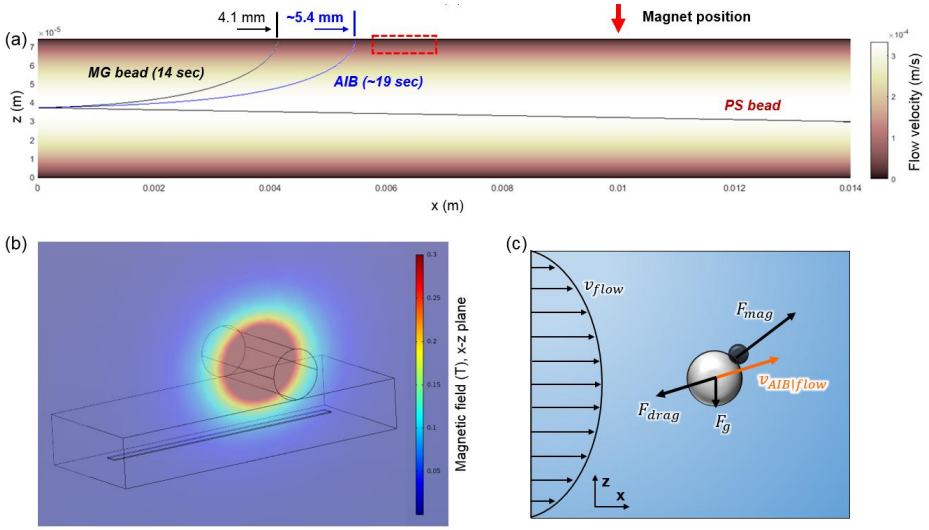

Figure 4-4. (a) Velocity profile of the flow and estimated trajectory of each particle (MG, AIP, and PS). (b) Simulation of the magnetic field of the device (COMSOL Multiphysics 5.2), (c) Various forces exerted on the AIP during the rise. The drag force is proportional to the relative velocity between the AIP and the sample flow. Gravitational force is no longer negligible when AIP is placed far away from the magnet. Red dotted boxes indicate the sensing area and red arrow indicates the center of the magnet.

4.3 Sliding behavior on the surface

Now, the AIP reaching the upper surface of the microchannel receives the resistance of the wall and slides. With a high flow rate, a sufficient but not too strong magnetic force, and smooth surface, our device provides appropriate environment for AIPs to slide along the surface. Especially, the magnet was placed to balance the frictional and the magnetic attraction force for AIPs. As a result, the individual AIPs are speed-distinguished only by their size.

4.3.1 Forces on sliding AIP

The strength, size, and placement of the magnet should be precisely adjusted for AIP to appropriately slide near the surface without being adsorbed. To achieve this, we theoretically estimated the sliding velocity of AIP, based on the forces exerted on the AIP by external magnetic field and driven flow condition. When the AIP slides on the upper surface of the microchannel; it experiences (1) the magnetic force in the flow direction, (2) the friction force induced by the vertical component of magnetic force, and (3) the Stoke's drag force by the flow. The velocity of AIP can be calculated by the balance of these three forces. First, the magnetic force in the flow direction acting on the AIP is obtained by[71, 77]

$$\boldsymbol{F_{mag}} = \mu_0 V \chi (\boldsymbol{H} \cdot \boldsymbol{\nabla}) \boldsymbol{H} \qquad (4\text{-}27)$$

where μ_0 is the magnetic permeability constant which is equal to $1.26 \times 10^{-6} N/A^2$; V is the volume of the superparamagnetic microparticle with a mean diameter of 1.05 μm; χ is the effective magnetic susceptibility which

was measured to be 0.3 from another independent study;[72] $\boldsymbol{H}$ is the magnetic field and $(\boldsymbol{H}\cdot\boldsymbol{\nabla})\boldsymbol{H}$ was calculated by the used magnets of the cylindrical shape. Applying a cylinder magnet model, the magnetic force in the flow direction exerted on AIP is calculated by

$$F_{mag,x} = \mu_0 V \chi M_s^2 R_{mag}^4 \frac{x_d}{2[z_d^2 + x_d^2]^3} \tag{4-28}$$

where M_s is a magnetized level ($1.11 \times 10^6\ A/m$); R_{mag} is the radius of the cylindrical magnet which is equal to 2.0 mm. z_d and x_d are a vertical and lateral distance between AIP and the magnet and equal to 5.0 mm and 3.6 mm, respectively. Note that x_d is obtained by considering average distance in the sensing area. For the AIP with a single magnetic particle, the magnetic force ($F_{mag,x}$) received when sliding in the sensing area is calculated to be 0.15 pN. Second, the magnetic force in the direction perpendicular to the microchannel is similarly calculated by

$$F_{mag,z} = \mu_0 V \chi M_s^2 R_{mag}^4 \frac{z_d}{2[z_d^2 + x_d^2]^3} \tag{4-29}$$

The magnetic normal force ($F_{mag,z}$) is obtained as 0.2 pN, allowing AIPs to reach the upper surface before entering the sensing area. The trajectory of the AIP while reaching the microchannel surface was theoretically estimated in Fig. 4-4. The kinetic friction coefficient (μ_k) between AIP and BSA-PDMS surface was assumed to be in a range of 0.7~1.0, considering the friction between the antibody-grafted particle and hydrophilic surface.[78] We

estimate the friction force as ~0.15 pN ($F_{friction} = \mu_k F_{mag,x}$). It should be pointed out that the net force exerted on the AIP in the direction of the sample flow induced by external magnetic field is nearly cancelled out by the friction force. This condition was achieved by selecting the lateral distance x_d equal to $\mu_k z_d$, which was obtained by axisymmetric magnetic field around cylinder magnet, resulting in AIPs being mainly slid by flow drag. The position of the magnet and the sensing area can be unambiguously determined. In case of AIP with double or multiple magnetic particles, each force increases in proportion to the number of magnetic particles it contains and still offset each other. Third, the drag force exerted on the AIP in a flow can be calculated as[17]

$$F_{drag} = 6\pi\eta R_{AIB}\Delta v_c f_D K \tag{4-30}$$

where R_{AIB} is the effective radius of AIP; for those with only PS-MG single binding, the average value of 1.42 μm by taking the radius of a sphere having the same volume as the AIP, η is the dynamic viscosity ($\eta = 1.0 \times 10^{-3}\ N \cdot S/m^2$ for water), and f_D is the drag coefficient which is assumed to be 3.1 when AIP is sliding close to the surface. Δv_c represents the velocity difference between the AIP (v_{AIB}) and the external flow (v_f). Due to the wall effect, the flow speed is reduced near the surface. K is a correction factor of about 1 to 1.5 for AIPs depending on the number of bindings and aggregation shape since the AIP has a non-spherical shape.[74] Considering the sample flow as a plane Poiseuille flow between two parallel plates, the velocity profile of the sample flow is expressed as[70]

$$v_f(z) = \frac{3\overline{v_f}}{2}\left[1 - \left(\frac{h_c - z}{h_c}\right)^2\right] \quad (4\text{-}31)$$

where $\overline{v_f}$ is the average channel flow velocity of 222 μm/s, and h_c is 37.5 μm, half of the height of the microchannel. z is the distance from the surface and is equal to R_{AIB} for the sliding AIP. From eqn 4-30 and 4-31, a stationary AIP with a single PS-MG bond takes F_{drag} of 2~3 pN while v_f is 24.7 μm/s. Compared to either $F_{mag,x}$ or $F_{friction}$, AIP receives at least 10-fold more force. By balancing the forces acting on the AIP ($F_{drag} = F_{friction} - F_{mag,x}$), Δv_c becomes zero. Thus, the AIP moves along the surrounding flow where it is located. Each AIP has different effect radius according to its shape and R_{AIB} increases as the total volume of AIP increases (Fig. 4-5). The flow velocity profile near the surface is derived from eqn 4-31 and the estimated sliding velocity of each type are marked in Fig. 4-5b. Note that most AIPs did not rotate in any direction and maintain almost constant velocity when they are sliding across the sensing area, regardless of their longitudinal position. The two particles in the AIP have different hydrodynamic strengths. Thus, the AIP tends to align with the external flow.[79]

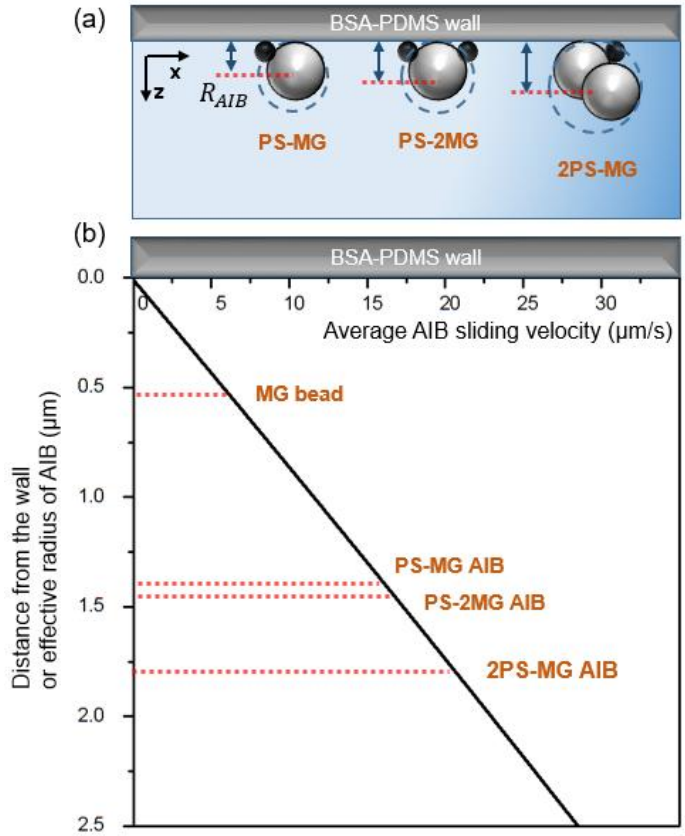

Figure 4-5. Various types of AIP that were frequently observed in the sensing area. (a) Schematic of effective radius and distance from the wall of various AIPs. (b) Flow velocity profile near the microchannel wall and estimated AIP velocity based on the effective radius.

4.3.2 Velocity reduction of sliding AIP in the sensing area

As the AIP slides along the flow and gets closer to the magnet, the magnetic force becomes stronger. Therefore, the net force in the x-direction induced by the external magnetic field also changes. The magnetic force and the friction force applied to the AIP are estimated as shown in Fig. 4-6. Specifically, the net force ($F_{mag,x} - \mu_k F_{mag,z}$) in the x-direction is -0.04 pN on average in the sensing area and smallest at the outermost edge. For single-bond AIP, the velocity is reduced by 3.6% across the sensing area. Similarly, the velocity reduction in 2PS-MG AIP is 2.1% and in the PS-2MG AIP is 6.7%. Thus, the sliding velocity in the sensing area hardly changes by the magnetic force.

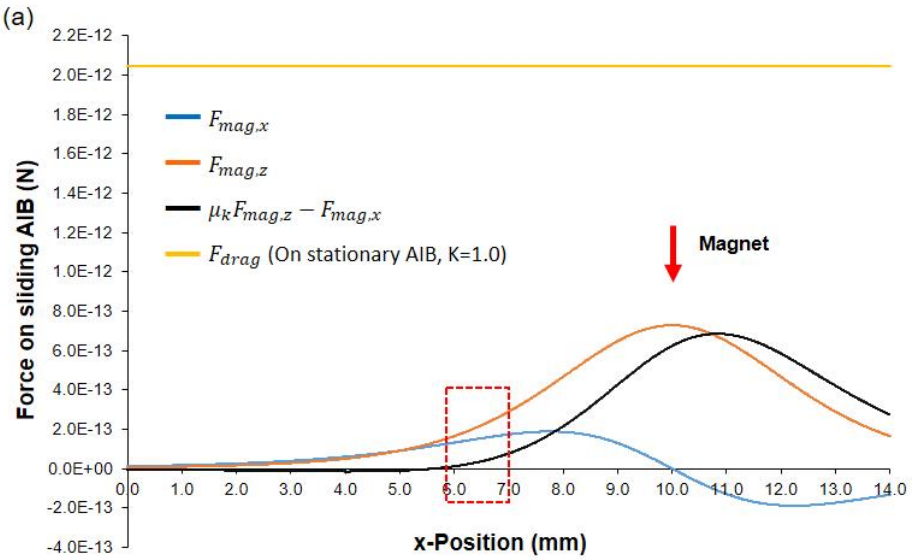

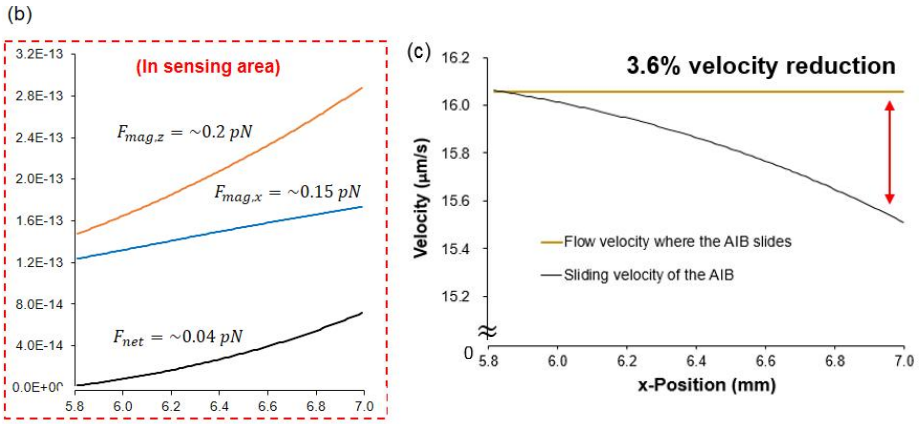

Figure 4-6. (a) The magnetic force and friction force on sliding AIP throughout the microchannel (The magnet is placed at x = 10mm). (b) The magnetic force inside the sensing area. The net force induced by the external magnet is about -0.04 pN in x-direction when the friction coefficient is 0.85 (μ_k = 0.7~1.0) (c) Velocity reduction of single bonded AIP across the sensing area.

4.3.3. Frictional behavior of AIP on BSA-PDMS surface

A slippery surface is a prerequisite for the proposed system to function correctly as a sliding sensor. PDMS was coated with BSA to prevent surface nonspecific adsorption of antibodies or proteins and to prevent particles from adsorbing to the surface. PBS containing 1% w/v BSA was soaked in microchannel for 4 hours and then dried for 24 hours to obtain PDMS coated with BSA at room temperature.[80]

BSA coating helps the particles slip properly without consuming biomolecules in the sample solution without adsorbing them on the walls. Fig. 4-7 shows the contact angle of the droplet when the sample solution (PBS + 0.1% BSA) is placed on PDMS. PDMS generally has hydrophobic surface properties and exhibits a contact angle of 104° for exposed PDMS. On the

other hand, PDMS coated with BSA exhibits hydrophilicity with a contact angle of 55°. Fig. 4-7 shows the recovery performance of such a BSA coated surface. Even when the antibody particles are adsorbed, they are washed with fresh buffer at a flow rate of 10 to 50 μL/min, indicating that they have almost completely recovered the surface. This shows that coated BSA adequately suppresses nonspecific adsorption of particles. If the speed is too slow, it can be adsorbed by BSA coating. Therefore, it is preferable to use an appropriate flow rate (1 μL/min) in the experimental environment.

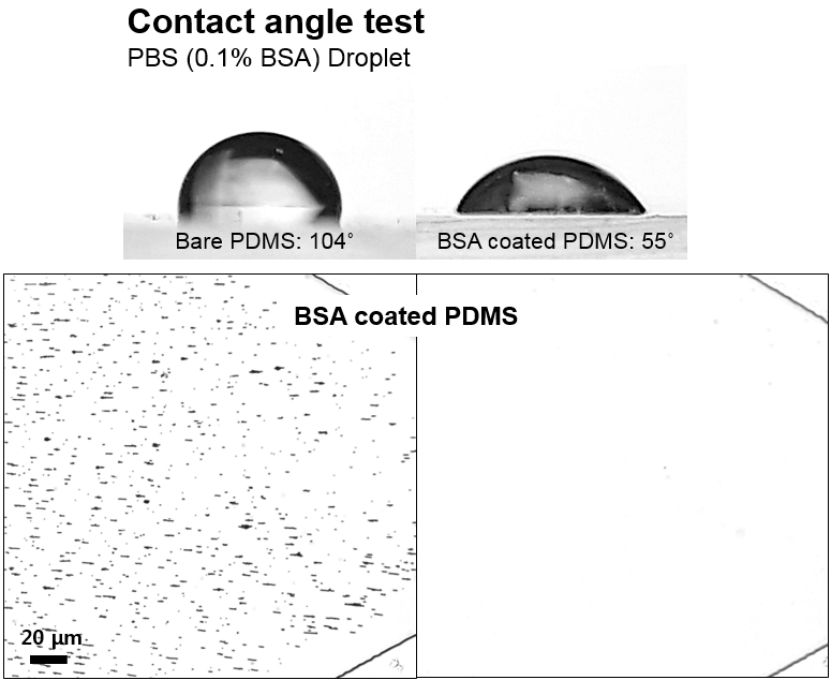

Figure 4-7. Top: Buffer contact angle on PDMS and BSA treated PDMS. Down: Microchannel surface recovery after BSA treatment; adsorbed PS and MG are easily removed and refreshed by PBS buffer.

G. Kokkinis. *et. al*. performed a test of scratching the hydrophilic surface by the antibody coated Dynabead as AFM tip.[81] We measured the magnitude of the kinetic friction coefficient between the antibody particles and the surface. They have a wide range of friction coefficients across different measurements due to their surface adhesion properties with antibody particles. In fact, when analyzing particle movements individually, the particles did not move continuously but discrete movements. Defining the kinematic friction coefficient as a single value is intricate. The kinetic frictional force can vary depending on various factors such as the slip angle, the shape of the aggregate, and the difference in the surface density of the antibody. However, since the hydrodynamic drag is dominant in the system, the influence of the frictional force is negligible and the influence on particle velocity is also relatively small.

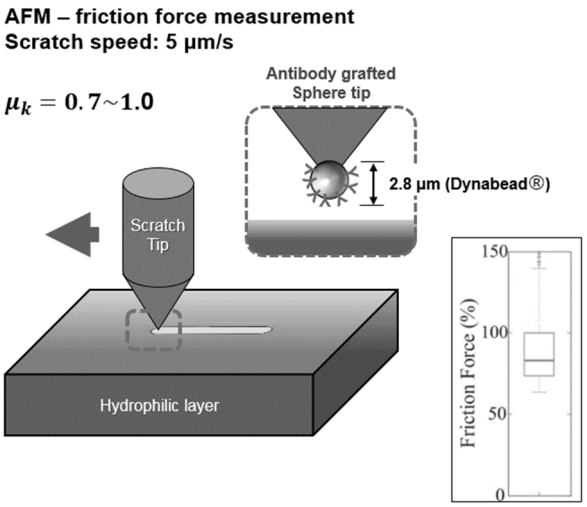

Figure 4-8. Kinetic friction measurement process: Antibody grafted Dynabead was scratched on the hydrophilic surface to estimate kinetic friction coefficient.[81]

4.3.4 Non-rotating AIP in sliding motion

The sensing signals of the proposed system were obtained by measuring the number and speed of AIP. In the system, the AIP was considered as a lump without rotational motion, but a precise understanding of how the individual AIP actually moves on the top surface is needed. In other words, if there is a rotary motion in the AIP that performs a linear constant motion if it is rotated, it is necessary to identify how much the angular velocity is and how the velocity of the slip changes accordingly. Therefore, we analyzed the effects of force and torque when a single bonded AIP (PS-MG) slides on the wall.

Prior to the analysis, one has to make sure that both the PS and MG of the AIP are sitting on the wall and sliding. Starting from the middle of the microchannel, the AIP moves upward toward the external magnet and begins to slip on the wall. The MG of AIP contacts with the wall by magnetic force. In the case of PS, there is no magnetic force, but with the help of the velocity gradient near the wall, it quickly goes to the wall surface. Particularly, in the experimental setup in which the frictional force acting on the magnetic particles and the magnetic attracting force are canceled, the MG and the PS move according to the surrounding velocity of each part. As a result, both the MG and the PS are forced to move along the wall.

For force and torque analysis, the free body diagram is shown in Fig. 4-9. The net force in the x and z directions must be zero since the whole body is moving at a constant velocity. In addition, since the rotation on the x-z plane cannot occur due to the constraint by the upper wall surface, the torque sum in the x-z plane becomes zero (Note that the small particles and large particles

are in contact with each other and the wall surface, resulting in an angle of 28.3°). First, the force in the x-direction acting on the MG of AIP is

$$F_{MG,x} = F_{mag,x} - F_{drag,MG} - F_{fric,MG} \tag{4-32}$$

And acting on the PS of AIP is

$$F_{PS,x} = F_{drag,PS} = -F_{mag,x} + F_{drag,MG} + F_{fric,MG} \tag{4-33}$$

Because the net x-directional force conservation of the AIP. Z-directional force conservation of both particles can similarly be

$$F_{mag,z} = F_{n,tot} = F_{n,MG} + F_{n,PS} \tag{4-34}$$

Because the net z-directional force of both particles should be equal to magnetic normal force of a single magnetic particle (MG). Torque equilibrium of AIP can be described as

$$\begin{aligned}(R_{MG} + R_{PS})cos(\varphi_0)cos(\theta)\, F_{n,PS} \\ = R_{MG}\left(F_{mag,x} - F_{drag,MG}\right) \\ + R_{PS}(F_{drag,MG} + F_{fric,tot} - F_{mag,x})\end{aligned} \tag{4-35}$$

Considering the position of the MG contacting the wall as a pivot point.

Here, the drag force acting on PS and MG does not act in proportion to the radius of each particle. This is because the area in which the particles are

exposed to the flow rate depends on the tilted angle. Thus, although each particle is subject to independent drag forces, there is a complicated relationship. When the particles were moving linearly at constant velocity, forces acting perpendicular to the PS particles were obtained through force and torque equilibrium conditions in the x-z plane. Now, when we analyze the force of the particles in the upper x-y plane, we can see that the net values of these forces acting on each of the MG and PS particles must be zero. Otherwise, the AIP must rotate with respect to the plane by the biasing force. The frictional forces acting on the PS are thus:

$$F_{fric,PS} = \mu_k F_{n,PS} = \mu_k \frac{\{R_{MG}(F_{mag,x} - F_{drag,MG}) + R_{PS}(F_{drag,MG} + F_{fric,tot} - F_{mag,x})\}}{(R_{MG} + R_{PS})cos(\varphi_0)cos(\theta)} \quad (4\text{-}36)$$

Here, since the values of the other terms are negligibly small compared to $R_{MG}F_{mag,x}$ (because friction force and x-directional magnetic force are balanced in our system):

$$F_{fric,PS} \approx \mu_k \frac{R_{MG}F_{mag,x}}{(R_{MG} + R_{PS})cos(\varphi_0)cos(\theta)} \quad (4\text{-}37)$$

Since the net force acting on the center of each particle in the x-y plane must be zero not to rotate:

$$F_{fric,tot} - F_{mag,x} + F_{drag,MG} - F_{fric,PS} = 0 \quad (4\text{-}38)$$

Rewriting the above equation:

$$F_{drag,MG} = F_{fric,PS} \tag{4-39}$$

Therefore, when performing linear motion without angular velocity, the angle θ becomes:

$$cos(\theta) = \mu_k \frac{R_{MG} F_{mag,x}}{(R_{MG} + R_{PS}) cos(\varphi_0) F_{drag,MG}} \tag{4-40}$$

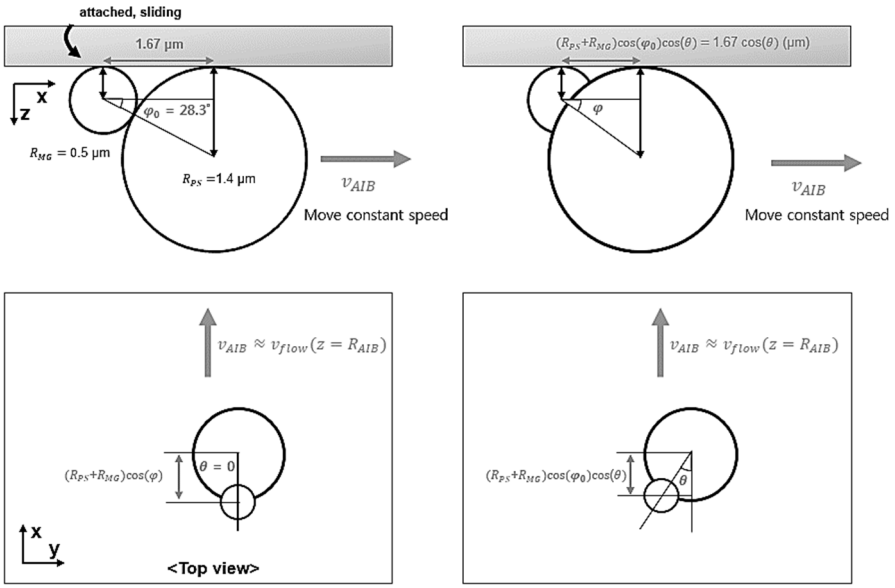

Figure 4-9. The angle between the two spheres of the AIP when attached to the top surface.

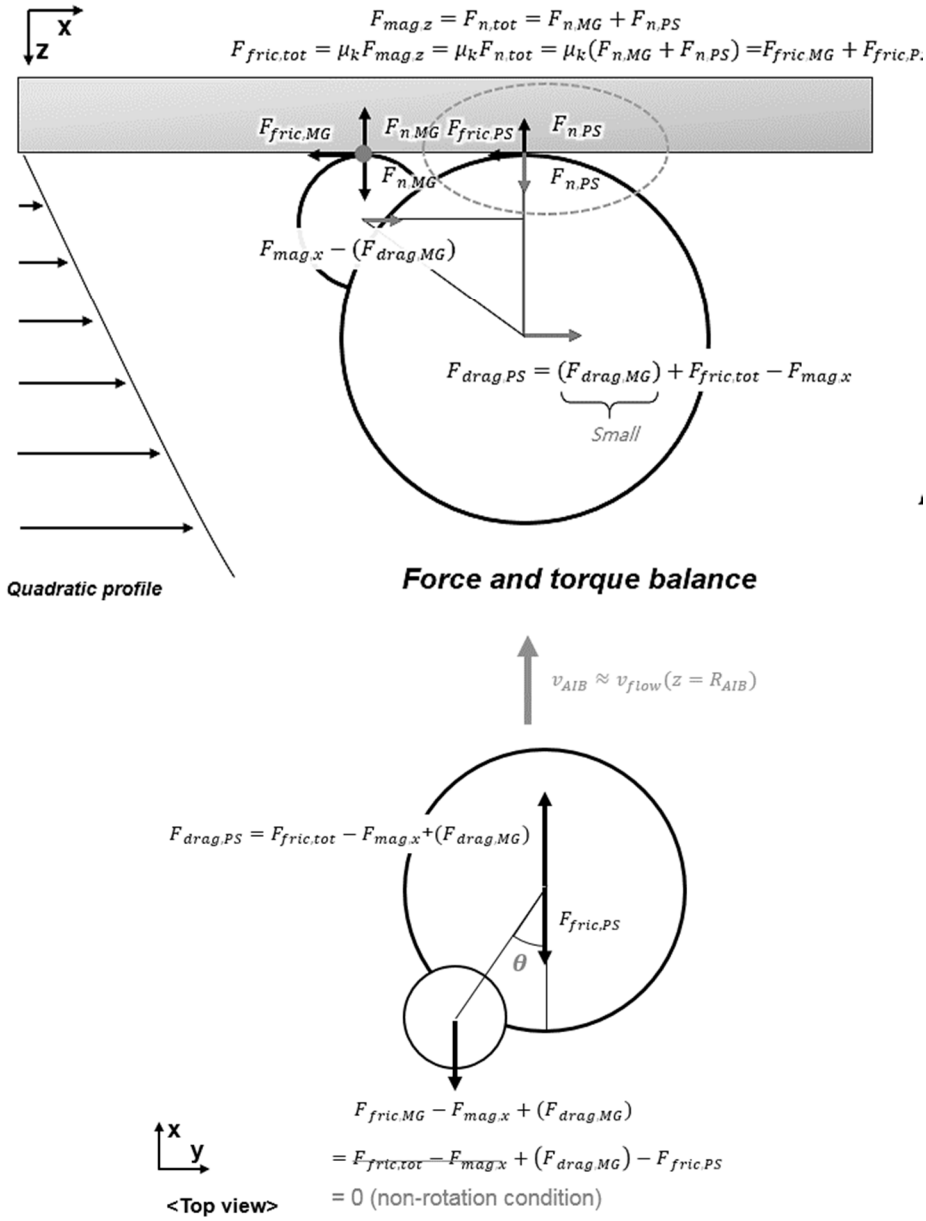

Figure 4-10. Force and torque equilibrium of AIP

Table 4-3. List of constants and variables

$\boldsymbol{F_{fric,MG}}$	Friction force between MG of AIP and upper surface
$\boldsymbol{F_{mag,x}}$	x-directional component of magnetic force of MG of AIP
$\boldsymbol{F_{drag,MG}}$	Drag force on MG of AIP
$\boldsymbol{F_{n,MG}}$	Normal force of MG of AIP against upper surface
$\boldsymbol{F_{fric,PS}}$	Friction force between PS of AIP and upper surface
$\boldsymbol{F_{drag,PS}}$	Drag force on PS of AIP
$\boldsymbol{F_{n,PS}}$	Normal force of PS of AIP against upper surface
$\boldsymbol{F_{n,tot}}$	Total normal force of AIP against upper surface ($= F_{mag,z}$)
$\boldsymbol{F_{fric,tot}}$	Total friction force between AIP and upper surface ($= \mu_k F_{mag,z}$)
$\boldsymbol{R_{MG}}$	Radius of MG (0.5 μm)
$\boldsymbol{R_{PS}}$	Radius of PS (1.4 μm)
$\boldsymbol{\varphi_0}$	The angle formed by the straight line connecting the centers of MG and PS to the wall. (φ_0 =28.27˚)
$\boldsymbol{\theta}$	In the x-y plane, the angle between the straight line connecting the center of MG and PS with the flow direction.

Chapter 5. Conclusion

A novel immunodetection method based on AIP has been proposed. AIP is an asymmetric particle immunoaggregation produced by specific antibody-antigen sandwich binding between two particles of different size and magnetism. Since AIP is larger than a single particle and is also attracted to an external magnetic field, two independent parameters can be used to quantify the formation of AIPs. The number of AIPs formed is associated with a target analyte concentration present in a particular solution. Also, the sensor design becomes simpler due to the magnetic characteristics of AIP.

Firstly, the aggregation behavior of AIP against the target analyte was investigated by comparison with conventional symmetric aggregation techniques. The detectable range of analyte concentration and the correlation between analyte concentration and AIP number was measured *via* custom-built program code. In the case of measuring at least 3~4000 random particles/AIPs by recognizing the shape of the particle/AIPs, it was possible to observe up to ~15% of aggregation ratio in the presence of target analyte. In particular, immunodetection by asymmetric aggregates has been confirmed to be more sensitive because it can exclude non-specific aggregation such as symmetric aggregation, also provides more diffusions.

Secondly, a sensor using only magnetic properties, not particle shape recognition, has been developed. In other words, only AIPs and MGs are selectively taken out from the sample solution by the external magnetic field, and counted, unlike other non-aggregated single particles. In this case, since the MGs are much smaller than the AIP (containing PS), they can be easily distinguished, and only AIPs can be counted and detected. In this case,

because the optical requirements are not strict, the test can be conducted by substituting the microscope with CIS. In general, however, this method has a disadvantage in automation and relatively large error as well as a lot of manual particle handlings (*e.g.* pipetting).

Finally, microchannel-based AIP sensor was developed. We have devised a device in which an external magnetic field is placed on a straight microchannel at the top. AIPs, which enters by the syringe pump, are flowed in the channel and AIPs passing the channel was counted in a designated sensing area in the upper surface after attracted by the external magnetic field. The counted AIPs is correlated the aggregation ratio and target concentration. The AIPs make a sliding motion at a speed proportional to its own size. We analyzed the drifting trajectory of each AIP and conducted force analysis to predict the speed. This allowed us to optimize the proper magnet position and chip fabrication. The AIP has intermediate size and magnetic strength against single particles, enabling the clear-cut sensing. For data acquisition, the sliding AIP was recorded as a video and processed through custom-built video analysis code. As the concentration of the target analyte increased, more AIPs were found to slip faster. We have demonstrated a detection range of 54 pg / mL to 54 ng / mL for influenza H1N1 type A NP as a model antigen (LOD: 40 pg/mL). This method can be applied to various types of antigens and biomarkers for quantification. Compared to traditional ELISA methods, this method is cost-effective, provides fast detection (within 10 min) with high sensitivity and does not require complex measurement setups. In addition, the optical magnification is less or equal than 100X. In particular, large detection windows and video frame analysis enable consistent, robust, and automated detection by a single processing. We expect many applications for rapid

detection and personalized diagnostic systems in a variety of clinical applications.

Bibliography

[1] X. Gao, H. J. Mathieu, and M. Schawaller, "Surface modification of polystyrene biochip for biotin-labelled protein/streptavidin or neutravidin coupling used in fluorescence assay," *Surface and Interface Analysis,* 36, 1507-1512, 2004.

[2] K. Länge, G. Blaess, A. Voigt, R. Götzen, and M. Rapp, "Integration of a surface acoustic wave biosensor in a microfluidic polymer chip," *Biosensors and Bioelectronics,* 22, 227-232, 2006.

[3] A. J. Baeumner, "Biosensors for environmental pollutants and food contaminants," *Analytical and Bioanalytical Chemistry,* 377, 434-445, 2003.

[4] M. J. Jebrail and A. R. Wheeler, "Let's get digital: digitizing chemical biology with microfluidics," *Current Opinion in Chemical Biology,* 14, 574-581, 2010.

[5] S. I. Stoeva, J.-S. Lee, C. S. Thaxton, and C. A. Mirkin, "Multiplexed DNA Detection with Biobarcoded Nanoparticle Probes," *Angewandte Chemie,* 118, 3381-3384, 2006.

[6] Y. Zhang *et al.*, "Two dimensional barcode-inspired automatic analysis for arrayed microfluidic immunoassays," *Biomicrofluidics,* 7, 034110, 2013.

[7] P. Hauer, E. C. Le Ru, and G. R. Willmott, "Co-ordinated detection of microparticles using tunable resistive pulse sensing and fluorescence spectroscopy," *Biomicrofluidics,* 9, 014110, 2015.

[8] H. Li, Z. Cao, Y. Zhang, C. Lau, and J. Lu, "Combination of quantum dot fluorescence with enzyme chemiluminescence for multiplexed detection of lung cancer biomarkers," *Analytical Methods,* 2, 1236-1242, 2010.

[9] T. Ihara, Y. Mori, T. Imamura, M. Mukae, S. Tanaka, and A. Jyo, "Colorimetric multiplexed immunoassay using specific aggregation of antigenic peptide-modified luminous nanoparticles," *Analytica Chimica Acta,* 578, 11-18, 2006.

[10] T. Endo *et al.*, "Multiple Label-Free Detection of Antigen−Antibody Reaction Using Localized Surface Plasmon Resonance-Based Core−Shell Structured Nanoparticle Layer Nanochip," *Analytical Chemistry,* 78, 6465-6475, 2006.

[11] X. D. Hoa, A. G. Kirk, and M. Tabrizian, "Towards integrated and sensitive surface plasmon resonance biosensors: A review of recent progress," *Biosensors and Bioelectronics,* 23, 151-160, 2007.

[12] S. Yang *et al.*, "Electrochemically created highly surface roughened Ag nanoplate arrays for SERS biosensing applications," *Journal of Materials Chemistry C,* 2, 8350-8356, 2014.

[13] S. Yang *et al.*, "Superhydrophobic surface enhanced Raman scattering sensing using Janus particle arrays realized by site-specific electrochemical growth," *Journal of Materials Chemistry C,* 2, 542-547, 2014.

[14] D. C. Pregibon, M. Toner, and P. S. Doyle, "Multifunctional Encoded Particles for High-Throughput Biomolecule Analysis," *Science,* 315, 1393-1396, 2007.

[15] C. T. Lim and Y. Zhang, "Particle-based microfluidic immunoassays: the next generation," *Biosensers & Bioelectronics,* 22, 1197-1204, 2007.

[16] M. A. M. Gijs, "Magnetic particle handling on-chip: new opportunities for analytical applications," *Microfluidics and Nanofluidics,* 1, 22-40, 2004.

[17] M. A. M. Gijs, F. Lacharme, and U. Lehmann, "Microfluidic Applications of Magnetic Particles for Biological Analysis and Catalysis," *Chemical Reviews,* 110, 1518-1563, 2010.

[18] K. Leirs *et al.*, "Bioassay Development for Ultrasensitive Detection of Influenza A Nucleoprotein Using Digital ELISA," *Analytical Chemistry,* 88, 8450-8458, 2016.

[19] D. M. Rissin *et al.*, "Single-molecule enzyme-linked immunosorbent assay detects serum proteins at subfemtomolar concentrations," *Nature Biotechnology,* 28, 595-599, 2010.

[20] D. Witters, K. Knez, F. Ceyssens, R. Puers, and J. Lammertyn, "Digital microfluidics-enabled single-molecule detection by printing and sealing single magnetic particles in femtoliter droplets," *Lab on a Chip,* 13, 2047-2054, 2013.

[21] Y. K. Hahn and J.-K. Park, "Versatile immunoassays based on isomagnetophoresis," *Lab on a Chip,* 11, 2045-2048, 2011.

[22] H. C. Tekin, M. Cornaglia, and M. A. M. Gijs, "Attomolar protein detection using a magnetic particle surface coverage assay," *Lab on a Chip,* 13, 1053-1059, 2013.

[23] Y. Han, H. Wu, F. Liu, G. Cheng, and J. Zhe, "Label-Free Biomarker Assay in a Microresistive Pulse Sensor *via* Immunoaggregation," *Analytical Chemistry,* 86, 9717-9722, 2014.

[24] T. Takakura, I. Yanagi, Y. Goto, Y. Ishige, and Y. Kohara, "Single-molecule detection of proteins with antigen-antibody interaction using resistive-pulse sensing of submicron latex particles," *Applied Physics Letters,* 108, 123701, 2016.

[25] Y. Han, H. Wu, F. Liu, G. Cheng, and J. Zhe, "A multiplexed immunoaggregation biomarker assay using a two-stage micro resistive pulse sensor," *Biomicrofluidics,* 10, 024109, 2016.

[26] J. L. Guesdon and S. Avrameas, "Magnetic Solid-Phase Enzyme-Immunoassay," *Immunochemistry,* 14, 443-447, 1977.

[27] R. S. Sista, A. E. Eckhardt, V. Srinivasan, M. G. Pollack, S. Palanki, and V. K. Pamula, "Heterogeneous immunoassays using magnetic particles on a digital microfluidic platform," *Lab on a Chip,* 8, 2188-2196, 2008.

[28] J. Do and C. H. Ahn, "A polymer lab-on-a-chip for magnetic immunoassay with on-chip sampling and detection capabilities," *Lab on a Chip,* 8, 542-549, 2008.

[29] Y. Moser, T. Lehnert, and M. A. M. Gijs, "On-chip immuno-agglutination assay with analyte capture by dynamic manipulation of superparamagnetic particles," *Lab on a Chip,* 9, 3261-3267, 2009.

[30] K. S. Kim and J. K. Park, "Magnetic force-based multiplexed immunoassay using superparamagnetic nanoparticles in microfluidic channel," *Lab on a Chip,* 5, 657-664, 2005.

[31] Y. K. Hahn, J. B. Chang, Z. Jin, H. S. Kim, and J. Y. Park, "Magnetophoretic position detection for multiplexed immunoassay using colored microspheres in a microchannel," *Biosensors & Bioelectronics,* 24, 1870-1876, 2009.

[32] H. Bayley and C. R. Martin, "Resistive-Pulse Sensing-From Microbes to Molecules," *Chemical Reviews,* 100, 2575-2594, 2000.

[33] K. Zhou, L. Li, Z. Tan, A. Zlotnick, and S. C. Jacobson, "Characterization of hepatitis B virus capsids by resistive-pulse sensing," *Journal of the American Chemical Society,* 133, 1618-1621, 2011.

[34] "Coulter counter," Wikipedia: The Free Encyclopedia., Inc. 1 June 2017. Web., https://en.wikipedia.org/wiki/Coulter_counter

[35] J. Kim, E. G. Kim, S. Bae, S. Kwon, and H. Chun, "Potentiometric multichannel cytometer microchip for high-throughput microdispersion analysis," *Analytical Chemistry,* 85, 362-368, 2013.

[36] J. Sha *et al.*, "Nanotubes complexed with DNA and proteins for resistive-pulse sensing," *ACS Nano,* 7, 8857-8869, 2013.

[37] C. C. Harrell, Y. Choi, L. P. Horne, L. A. Baker, Z. S. Siwy, and C. R. Martin, "Resistive-pulse DNA detection with a conical nanopore sensor," *Langmuir,* 22, 10837-10843, 2006.

[38] Z. D. Harms *et al.*, "Nanofluidic devices with two pores in series for resistive-pulse sensing of single virus capsids," *Analytical Chemistry,* 83, 9573-9578, 2011.

[39] D. J. Niedzwiecki, R. Iyer, P. N. Borer, and L. Movileanu, "Sampling a biomarker of the human immunodeficiency virus across a synthetic nanopore," *ACS Nano,* 7, 3341-3350, 2013.

[40] K. J. Freedman, A. R. Bastian, I. Chaiken, and M. J. Kim, "Solid-state nanopore detection of protein complexes: applications in healthcare and protein kinetics," *Small,* 9, 750-759, 2013.

[41] A. Carbonaro and L. L. Sohn, "A resistive-pulse sensor chip for multianalyte immunoassays," *Lab on a Chip,* 5, 1155-1160, 2005.

[42] W. Li *et al.*, "Single protein molecule detection by glass nanopores," *ACS Nano,* 7, 4129-4134, 2013.

[43] J. L. Fraikin, T. Teesalu, C. M. McKenney, E. Ruoslahti, and A. N. Cleland, "A high-throughput label-free nanoparticle analyser," *Nature Nanotechnology,* 6, 308-313, 2011.

[44] M. Wanunu, W. Morrison, Y. Rabin, A. Y. Grosberg, and A. Meller, "Electrostatic focusing of unlabelled DNA into nanoscale pores using a salt gradient," *Nature Nanotechnology,* 5, 160-165, 2010.

[45] J. D. Adams, U. Kim, and H. T. Soh, "Multitarget magnetic activated cell sorter," *Proceedings of the National Academy of Sciences of the United States of America,* 105, 18165-18170, 2008.

[46] M. Mizuno, M. Yamada, R. Mitamura, K. Ike, K. Toyama, and M. Seki, "Magnetophoresis-integrated hydrodynamic filtration system for size- and surface marker-based two-dimensional cell sorting," *Analytical Chemistry,* 85, 7666-7673, 2013.

[47] N. Pamme, "Magnetism and microfluidics," *Lab on a Chip,* 6, 24-38, 2006.

[48] C. Phurimsak, M. D. Tarn, S. A. Peyman, J. Greenman, and N. Pamme, "On-chip determination of C-reactive protein using magnetic particles in continuous flow," *Analytical Chemistry,* 86, 10552-10559, 2014.

[49] F. Shen, H. Hwang, Y. K. Hahn, and J. K. Park, "Label-free cell separation using a tunable magnetophoretic repulsion force," *Analytical Chemistry,* 84, 3075-3081, 2012.

[50] N. Pamme and A. Manz, "On-chip free-flow magnetophoresis: continuous flow separation of magnetic particles and agglomerates," *Analytical Chemistry,* 76, 7250-7256, 2004.

[51] D. Robert, N. Pamme, H. Conjeaud, F. Gazeau, A. Iles, and C. Wilhelm, "Cell sorting by endocytotic capacity in a microfluidic magnetophoresis device," *Lab on a Chip,* 11, 1902-1910, 2011.

[52] N. Pamme and C. Wilhelm, "Continuous sorting of magnetic cells *via* on-chip free-flow magnetophoresis," *Lab on a Chip,* 6, 974-980, 2006.

[53] K. S. Kim and J. K. Park, "Magnetic force-based multiplexed immunoassay using superparamagnetic nanoparticles in microfluidic channel," *Lab on a Chip,* 5, 657-664, 2005.

[54] Y. K. Hahn, J. B. Chang, Z. Jin, H. S. Kim, and J. K. Park, "Magnetophoretic position detection for multiplexed immunoassay

using colored microspheres in a microchannel," *Biosensors & Bioelectronics,* 24, 1870-1876, 2009.

[55] K. S. Kim and J. K. Park, "Superparamagnetic nanoparticle-based nanobiomolecular detection in a microfluidic channel," *Current Applied Physics,* 6, 976-981, 2006.

[56] N. Xia *et al.*, "Combined microfluidic-micromagnetic separation of living cells in continuous flow," *Biomedical Microdevices,* 8, 299-308, 2006.

[57] T. Scientific. *Immunoglobulin Structure and Classes*. Available: https://www.thermofisher.com/kr/ko/home/life-science/antibodies/antibodies-learning-center/antibodies-resource-library/antibody-methods/immunoglobulin-structure-classes.html

[58] S. Almeida-Prieto, J. Blanco-Méndez, and F. J. Otero-Espinar, "Microscopic image analysis techniques for the morphological characterization of pharmaceutical particles: Influence of the software, and the factor algorithms used in the shape factor estimation," *European Journal of Pharmaceutics and Biopharmaceutics,* 67, 766-776, 2007.

[59] M. Langton and A.-M. Hermansson, "Image analysis determination of particle size distribution," *Food Hydrocolloids,* 7, 11-22, 1993.

[60] D. MacDougall and W. B. Crummett, "Guidelines for data acquisition and data quality evaluation in environmental chemistry," *Analytical Chemistry,* 52, 2242-2249, 1980.

[61] R. Cheng, T. T. Zhu, and L. D. Mao, "Three-dimensional and analytical modeling of microfluidic particle transport in magnetic fluids," *Microfluidics and Nanofluidics,* 16, 1143-1154, 2014.

[62] T. T. Zhu, R. Cheng, Y. F. Liu, J. He, and L. D. Mao, "Combining positive and negative magnetophoreses to separate particles of

different magnetic properties," *Microfluidics and Nanofluidics,* 17, 973-982, 2014.

[63] Y. L. Zhou and X. C. Xuan, "Diamagnetic particle separation by shape in ferrofluids," *Applied Physics Letters,* 109, 131-135, 2016.

[64] C. X. Liu, T. Stakenborg, S. Peeters, and L. Lagae, "Cell manipulation with magnetic particles toward microfluidic cytometry," *Journal of Applied Physics,* 105, 2009.

[65] A. Weddemann, F. Wittbracht, A. Auge, and A. Hutten, "A hydrodynamic switch: Microfluidic separation system for magnetic particles," *Applied Physics Letters,* 94, 2009.

[66] L. F. Zanini, N. M. Dempsey, D. Givord, G. Reyne, and F. Dumas-Bouchiat, "Autonomous micro-magnet based systems for highly efficient magnetic separation," *Applied Physics Letters,* 99, 2011.

[67] L. T. Liang, C. Zhang, and X. C. Xuan, "Enhanced separation of magnetic and diamagnetic particles in a dilute ferrofluid," *Applied Physics Letters,* 102, 2013.

[68] R. Wirix-Speetjens, W. Fyen, X. Kaidong, B. Jo De, and G. Borghs, "A force study of on-chip magnetic particle transport based on tapered conductors," *IEEE Transactions on Magnetics,* 41, 4128-4133, 2005.

[69] Q. Zhao *et al.*, "High-throughput sheathless and three-dimensional microparticle focusing using a microchannel with arc-shaped groove arrays," *Scientific Reports,* 7, 41153, 2017.

[70] E. P. Furlani, Y. Sahoo, K. C. Ng, J. C. Wortman, and T. E. Monk, "A model for predicting magnetic particle capture in a microfluidic bioseparator," *Biomedical Microdevices,* 9, 451-463, 2007.

[71] F. Liu, P. Kc, G. Zhang, and J. Zhe, "Microfluidic Magnetic Particle Assay for Cell Detection," *Analytical Chemistry,* 88, 711-717, 2016.

[72] P. Tierno, S. V. Reddy, T. H. Johansen, and T. M. Fischer, "Rupture and healing of one-dimensional chains in a parametric magnetic ratchet potential," *Physical Review E,* 75, 041404, 2007.

[73] L. E. Helseth, T. M. Fischer, R. W. Hansen, and T. H. Johansen, "Microscopic magnetic squeezer," *Applied Physics Letters,* 85, 2556-2558, 2004.

[74] E. Loth, "Drag of non-spherical solid particles of regular and irregular shape," *Powder Technology,* 182, 342-353, 2008.

[75] G. Ahmadi. *Hydrodynamic forces*.

[76] A. Einstein, "Investigations on the Theory of Brownian Movement," *Dover: New York,* 1956.

[77] E. P. Furlani and K. C. Ng, "Analytical model of magnetic nanoparticle transport and capture in the microvasculature," *Physical Review E,* 73, 061919, 2006.

[78] G. Kokkinis, B. Plochberger, S. Cardoso, F. Keplinger, and I. Giouroudi, "A microfluidic, dual-purpose sensor for in vitro detection of Enterobacteriaceae and biotinylated antibodies," *Lab on a Chip,* 16, 1261-1271, 2016.

[79] W. E. Uspal, H. B. Eral, and P. S. Doyle, "Engineering particle trajectories in microfluidic flows using particle shape," *Nature Communications,* 4, 2013.

[80] I. Nikcevic *et al.*, "Adsorption of fluorescently labeled microparticles on PDMS surfaces," in *International Society for Optics and Photonics.*, 5718, 159-167, 2005.

[81] G. Kokkinis, B. Plochberger, S. Cardoso, F. Keplingera, and I. Giouroudi, "A microfluidic, dual-purpose sensor for in vitro detection of Enterobacteriaceae and biotinylated antibodies," *Lab on a Chip,* 16, 1261-1271, 2016.

Appendix

A.MATLAB code: Particle and AIP discrimination from photomicrographs

Based on the following MATLAB (MATLAB R2016b, Mathworks®) code, all individual particles and AIPs in any photomicrographs (optimally, 200X magnification) were identified, and the number and size distributions of them were estimated. In particular, the AIPs were classified using the manual criteria of the circumference and area ratio of each object. The MATLAB code can be further scaled according to the magnification of the captured image and the size of the particle used (other size options but 2.8 or 1.0 μm), depending on the quality of the image, the focal length, and error sensitivity. One can customize the parameter for optimized results.

```
----------------------------------------------------------------
close all; clear;
format long;

% Error elimination
err1=2;
% Monomer criterion number of pixel
mono_criterion=15;
pixtoleng=1280/589.71; %Scaling of length from pixel
imagefiles = dir('*.jpg');
nfiles=length(imagefiles);
effective_dia_from_area_all_1=zeros(1,20000);
perimeter_all_1=zeros(1,20000);cent_xy_all_1=zeros(20000,2);
effective_dia_from_snowarea_all_1=zeros(1,20000);
snowperi_all_1=zeros(1,20000);snowcent_xy_all_1=zeros(20000,2);
ssize=0; ssize2=0;
area_of_each_img=zeros(1,nfiles);
for ii=1:1:nfiles % image reading
    xx=imagefiles(ii).name;
    x=imread(xx);
    %x = imread('big.jpg');
    bw1 = 1-im2bw(x,graythresh(x));
    bw = imfill(bw1,'holes');
    imshow(bw)
```

```
%title GrayThreshed
bwc=bwconncomp(bw);
 stats = regionprops('table',bwc,'Centroid','Area', ...,
 'Perimeter','MajorAxisLength','MinorAxisLength')
centers = stats.Centroid;
radii = stats.Perimeter/2/pi;
hold on;

% Error elimination
k=0;
for j=1:1:size(stats.Area,1)
     if(stats.Area(j) > err1 && stats.Area(j) <
     8*mono_criterion) %
        k=k+1;
    end
end
effective_dia_from_area1=zeros(1,k);
area1=zeros(1,k); perimeter1=zeros(1,k);
cent_xy1=zeros(k,2);effective_dia_from_snowarea1=zeros(1,k);
snowperi1=zeros(1,k); snowcent_xy1=zeros(k,2);
k=1;mm=1;
for j=1:1:size(stats.Area,1)
   if(stats.Area(j)>err1 && stats.Area(j) <
   8*mono_criterion) %
   effective_dia_from_area1(k)=2*sqrt(stats.Area(j)/pi);
        area1(k)=stats.Area(j);
        perimeter1(k)=stats.Perimeter(j);
        cent_xy1(k,1)=stats.Centroid(j,1);
        cent_xy1(k,2)=stats.Centroid(j,2);

% Snowman detection sensitivity can be tuned here
        snowman_sense = 0.91;
        if(perimeter1(k)/area1(k) > snowman_sense *
            2/(sqrt(area1(k)/pi)) && area1(k)>37)
            effective_dia_from_snowarea1(mm)=effective_dia_f
            rom_area1(k);
            snowperi1(mm)=perimeter1(k);
            snowcent_xy1(mm,1)=cent_xy1(k,1);
            snowcent_xy1(mm,2)=cent_xy1(k,2);
            mm=mm+1;
        end
        k=k+1;
    end
end
viscircles(cent_xy1, 7* perimeter1/2/pi,'Color','b');
viscircles(snowcent_xy1, 4* snowperi1/2/pi,'Color','y');
hold off
for j=1:1:length(effective_dia_from_area1)
    effective_dia_from_area_all_1(j+ssize)=effective_dia_fr
    om_area1(j);
    perimeter_all_1(j+ssize)=perimeter1(j);
    cent_xy_all_1(j+ssize,1)=cent_xy1(j,1);
    cent_xy_all_1(j+ssize,2)=cent_xy1(j,2);
end
```

```
    for j=1:1:length(effective_dia_from_snowarea1)
        effective_dia_from_snowarea_all_1(j+ssize2)=effective_d
        ia_from_snowarea1(j);
        snowperi_all_1(j+ssize2)=snowperi1(j);
        snowcent_xy_all_1(j+ssize2,1)=snowcent_xy1(j,1);
        snowcent_xy_all_1(j+ssize2,2)=snowcent_xy1(j,2);
    end
    ssize=ssize+length(effective_dia_from_area1);
    ssize2=ssize2+length(effective_dia_from_snowarea1);
    area_of_each_img(ii)=length(effective_dia_from_area1);
end
k=0;
for j=1:1:length(effective_dia_from_area_all_1)
    if (effective_dia_from_area_all_1(j)>1)
        k=k+1;
    end
end
effective_dia_from_area_all=zeros(1,k);
perimeter_all=zeros(1,k);
cent_xy_all=zeros(k,2);
kk=0;
for j=1:1:length(effective_dia_from_snowarea_all_1)
    if (effective_dia_from_snowarea_all_1(j)>1)
        kk=kk+1;
    end
end
effective_dia_from_snowarea_all=zeros(1,kk);
snowperi_all=zeros(1,kk);
snowcent_xy_all=zeros(kk,2);
for j=1:1:k
    effective_dia_from_area_all(j)=effective_dia_from_area_all_
    1(j);
    perimeter_all(j)=perimeter_all_1(j);
    cent_xy_all(j,1)=cent_xy_all_1(j,1);
    cent_xy_all(j,2)=cent_xy_all_1(j,2);
end
jj=1;
for j=1:1:length(effective_dia_from_snowarea_all_1)
    if (effective_dia_from_snowarea_all_1(j)>1)
        effective_dia_from_snowarea_all(jj)=effective_dia_from_
        snowarea_all_1(j);
        snowperi_all(jj)=snowperi_all_1(j);
        snowcent_xy_all(jj,1)=snowcent_xy_all_1(j,1);
        snowcent_xy_all(jj,2)=snowcent_xy_all_1(j,2);
        jj=jj+1;
    end
end

% Monomer criterion number of pixel
k=0;
for j=1:1:length(effective_dia_from_area_all)
    if(pi*(effective_dia_from_area_all(j)/2)^2 >
      sqrt(mono_criterion) &&
      pi*(effective_dia_from_area_all(j)/2)^2 <
```

```
       6*sqrt(mono_criterion))  %&&
       pi*(effective_dia_from_area_all(j)/2)^2 <
       2.5*mono_criterion) %
        k=k+1;
    else
    end
end
standard_mono=zeros(1,k);
kk=1;
for j=1:1:length(effective_dia_from_area_all)
    if(pi*(effective_dia_from_area_all(j)/2)^2 >
       sqrt(mono_criterion) &&
       pi*(effective_dia_from_area_all(j)/2)^2 <
       6*sqrt(mono_criterion))  %&&
       pi*(effective_dia_from_area_all(j)/2)^2 <
       2.5*mono_criterion) %
        standard_mono(kk)=effective_dia_from_area_all(j);
        kk=kk+1;
    end
end
pixel_of_single_particle=mean(standard_mono);
% snowman ÁÃ multi-snowman fraction
kz=1;
for j=1:1:length(effective_dia_from_snowarea_all)

if(effective_dia_from_snowarea_all(j)>pixel_of_single_particle*2
.5)
        multi_snow_all(kz)=effective_dia_from_snowarea_all(j);
        kz=kz+1;
    end
end
mean_aggregation_number_of_particles =
mean(effective_dia_from_area_all)/pixel_of_single_particle %
std_of_aggregation_number_of_particles =
std(effective_dia_from_area_all)/pixel_of_single_particle %
hbins=200;
figure
h=histogram(effective_dia_from_snowarea_all/pixel_of_single_part
icle,round(hbins*3/5));
xlabel('~Number of Particles Aggregated')
ylabel('Snowman Counts')
title('Snowman Size Distribution')
saveas(gcf,'Snowman Size Distribution.png');
figure
h=histogram(effective_dia_from_area_all/pixel_of_single_particle
,hbins);
xlabel('~Number of Particles Aggregated')
ylabel('Cluster Counts')
title('Size Distribution (Numbers)')
saveas(gcf,'Number Distribution.png');
aggrecounts=0;
for i=1:1:length(effective_dia_from_area_all)
    if(effective_dia_from_area_all(i) >
pixel_of_single_particle*1.3)
```

```
        aggrecounts=aggrecounts+1;
    end;
end;

Num_of_bigger_or_equal_to_dimers=aggrecounts
aggregation_ratio=aggrecounts/length(effective_dia_from_area_all)
Ave_num_particle_of_img = mean(area_of_each_img)
Std_num_particle_of_img = std(area_of_each_img)

effective_dia_from_area_all=transpose(effective_dia_from_area_al
l);
effective_dia_from_snowarea_all=transpose(effective_dia_from_sno
warea_all);
fid=fopen('Particle analysis results.doc', 'w');
fprintf(fid, 'Number of image analyzed: %.0f \n',nfiles);
fprintf(fid, 'Pixel of single particle: %.4f
\n',pixel_of_single_particle);
fprintf(fid, 'Mean aggregation number of particles(Aggregation
Index): %.4f \n',mean_aggregation_number_of_particles);
fprintf(fid, 'Standard deviation of aggregation number of
particles: %.4f \n',std_of_aggregation_number_of_particles);
fprintf(fid, 'Number of total cluster: %.0f
\n',length(effective_dia_from_area_all));
fprintf(fid, 'Number of bigger than or equal to dimers: %.0f
\n',Num_of_bigger_or_equal_to_dimers);
fprintf(fid, 'Aggregation ratio: %.4f \n',aggregation_ratio);
fprintf(fid, '\nSnowman counting sensitivity(0.9~1.2): %.2f
\n',snowman_sense);
fprintf(fid, 'Snowman count: %.0f
\n',length(effective_dia_from_snowarea_all));
fprintf(fid, 'Snowman average size: %.2f
\n',mean(effective_dia_from_snowarea_all)/pixel_of_single_partic
le);
fprintf(fid, 'Snowman size standard deviation: %.2f
\n',std(effective_dia_from_snowarea_all)/pixel_of_single_particl
e);
fprintf(fid, 'Snowman ratio (vs. # of all particles): %.4f
\n',length(effective_dia_from_snowarea_all)/length(effective_dia
_from_area_all));
fprintf(fid, '\nMulti Snowman counts: %.4f
\n',length(multi_snow_all));
fprintf(fid, 'Multi Snowman ratio (vs. # of all particles): %.4f
\n',length(multi_snow_all)/length(effective_dia_from_area_all));
fprintf(fid, 'Multi Snowman ratio/Snowman ratio: %.4f
\n',length(multi_snow_all)/length(effective_dia_from_snowarea_al
l));
fprintf(fid, '\nAverage #clusters each image(in case of washing
assay): %.4f \n',Ave_num_particle_of_img);
fprintf(fid, 'Standard deviation of #clusters each image(in case
of washing assay): %.4f \n',Std_num_particle_of_img);
fclose(fid);
-------------------------------------------------------------------
```

B. MATLAB code: Trajectory of AIP inside the microchannel

The trajectory of AIP can be estimated by the following code based on the force equilibrium equations given in the force analysis section using a numerical method (Explicit Euler). AIPs are considered to appear at the center of the microchannel (z = 37.5 μm) in the microchannel entrance.

```
-----------------------------------------------------------------
close all; clear;
format long;

x_dist = 10*10^-3; % initial lateral dist. from the mag. center:
5mm
z_dist = 75*10^-6; % microchannel height
z_PDMS = 5*10^-3;% - z_dist; % PDMS thickness: 3mm + Magnet
radius: 2mm

length=2000001; % total iteration cycle
x_AIP = zeros(1,length);  z_AIP = zeros(1,length);
v_AIPx = zeros(1,length); v_AIPz = zeros(1,length);
v_AIPxx = zeros(1,length); v_AIPzz = zeros(1,length);
F_magx = zeros(1,length); F_magz = zeros(1,length);
F_dragx = zeros(1,length); F_dragz = zeros(1,length);
f_D = zeros(1,length); Fxdel = zeros(1,length); Fzdel =
zeros(1,length);
v_f = zeros(1,length);
del_vx = zeros(1,length);
t=linspace(0,1500,length);
dt=t(2)-t(1);

%%%%% Magnetic force and gravitational force %%%%%
mu0 = 1.26*10^-6; %% N/A^2
chi = 0.3;
M_s = 1.114*10^6; %% A/m
R_mag = 2*10^-3; %% m, Radius of cyl. mag.

V_mg = 6.061309e-19; %% 4/3*3.141592*(1.05*10^-6/2)^3 , MG dia:
1.0um
F_g= 7.8*10^-15; %% N, Net gravitational force of MG-PS AIP
Mag_cnst = mu0*chi*M_s^2*R_mag^4*V_mg;
m_AIP = 1.29*10^-14; % (kg, mass of MG-PS AIP)

%%%%% Drag force %%%%%
R_AIP = 1.42*10^-6;
K = 1; % shape factor
eta=1*10^-3;
```

```
pi=3.141592;
v_fbar = 10^-9/60/((1*10^-3)*(z_dist)); % 222*10^-6 m/s

%%%%% Iterative calculation %%%%%
z_AIP(1)=z_dist/2;
for i=1:1:length-1

v_f(i) = 3/2*v_fbar* (1 - ((0.5*z_dist-z_AIP(i))
/(0.5*z_dist))^2);
v_AIPx(1)=v_f(1);
del_vx(i) = v_AIPx(i) - v_f(i);

f_D(i) = 1; % wall effect
F_magx(i) = Mag_cnst * (x_dist-x_AIP(i))/(2*((z_PDMS-z_AIP(i))^2
+ (x_dist-x_AIP(i))^2)^3);
F_dragx(i) = 6*pi*eta*R_AIP*del_vx(i)*f_D(i)*K;
F_magz(i) = Mag_cnst * (z_PDMS-z_AIP(i))/(2*((z_PDMS-z_AIP(i))^2
+ (x_dist-x_AIP(i))^2)^3);
F_dragz(i) = 6*pi*eta*R_AIP*(v_AIPz(i))*f_D(i)*K;

v_AIPx(i+1) = v_AIPx(i) + 1/m_AIP * dt * (F_magx(i) -
F_dragx(i));
v_AIPxx(i+1) = v_f(i) + F_magx(i) /(6*pi*eta*R_AIP*f_D(i)*K);
if v_AIPx(i+1) < v_AIPxx(i+1)
else
    v_AIPx(i+1) = v_AIPxx(i+1);
end

v_AIPz(i+1) = v_AIPz(i) + 1/m_AIP * dt * (F_magz(i) -
F_dragz(i+1) - F_g );
v_AIPzz(i+1) = (F_magz(i) - F_g)/(6*pi*eta*R_AIP*f_D(i)*K);
if (v_AIPz(i+1) < v_AIPzz(i+1)) && v_AIPz(i+1) > 0
else
    v_AIPz(i+1) = v_AIPzz(i+1);
end
if (F_magz(i) - F_g) > 0
else
    v_AIPz(i+1) = 0;
end

    x_AIP(i+1) = x_AIP(i) + v_AIPx(i) * dt;
    z_AIP(i+1) = z_AIP(i) + v_AIPz(i) * dt;

    if (z_AIP(i) > z_dist - R_AIP)
        endtime=i*dt;
        break;
    end
end
plot(x_AIP,z_AIP);
-----------------------------------------------------------------
```

C.MATLAB code: Velocity distribution of sliding AIPs

To analyze and extract statistics from the recorded video, the following code was used for measuring the velocity distribution of the AIPs sliding at the microchannel top surface. The number of sliding AIPs and their corresponding velocity were obtained by comparing the relative positions of AIPs recognized per neighboring frame. Likewise, various parameters can be tuned for different experimental conditions.

```
-----------------------------------------------------------------
close all;clear;
format long;

pixtoleng=1180/840; pix_x=840; nbins=40;
% Snowman detection sensitivity
snowman_sense = 0.93;
% Read video
vidobj=VideoReader('file name.mp4');
NumFrames = vidobj.NumberOfFrames;
fontSize = 16;
level=-1; jj=1; jjj=1; frN=1; distaccu=1;
D_bco_position_tot=zeros(NumFrames*100,2);
D_barea_tot=zeros(NumFrames*100,1);
for m = 1:1:NumFrames
    thisFrame = read(vidobj, m);
    if ndims(thisFrame) >1
        thisFrame2= rgb2gray(thisFrame);
    end
    level = max([level, max(thisFrame(:))]);
    fprintf('After frame %d, the max gray level is %d.\n', m,
    level);
    if level == intmax(class(thisFrame))
        break;
    end
end
num_of_counted_cluster=zeros(1,NumFrames);
for frameNumber = 1:1:NumFrames
    fprintf('Processing frame %d. (Time: %.1f sec).\n',
    frameNumber,frameNumber/24);
    thisFrame = read(vidobj, frameNumber);
    thisFrame = rgb2gray(thisFrame);
    % Threshold the image.
    binaryImage = thisFrame > level-45;
    binaryImage_x = bwareaopen(1-binaryImage,7);
    binaryImage = 1-binaryImage_x
    % Label the image.
```

```
labeledImage = bwconncomp(1-binaryImage,8);
measurements =
regionprops(labeledImage,'Centroid','Area','Perimeter');

if length(measurements) == 0
    % No blobs found.
    fprintf('Done!\n');
    continue; % Skip to the next frame.
end
totalNumberOfBlobs = length(measurements);
num_of_counted_cluster(frameNumber) = totalNumberOfBlobs;
bco=zeros(totalNumberOfBlobs,2);
barea=zeros(totalNumberOfBlobs,1);
bperi=zeros(totalNumberOfBlobs,1);
snowcent_xy=zeros(totalNumberOfBlobs,2);
snowarea=zeros(totalNumberOfBlobs,1);
snowperi=zeros(totalNumberOfBlobs,1);
iii=1
for blobNumber = 1:1:totalNumberOfBlobs
    barea(blobNumber) = measurements(blobNumber).Area;
    if (barea(blobNumber) > 15)
        continue;
    else
        bco(blobNumber,:,:) =
       measurements(blobNumber).Centroid;
        bperi(blobNumber) =
       measurements(blobNumber).Perimeter;
    end
end
if (frameNumber > 1 && mod(frameNumber,3)==1)
    D = pdist2(bco,tempbco,'euclidean');
    % Distance threshold
    D_dist_bet_3frs = D( D > 0.1 & D < 5);
    distaccu_start=distaccu;
    for distrow= 1:1:length(bco)
        for distcol= 1:1:length(tempbco)
            if (D(distrow,distcol) > 0.1 &&
                D(distrow,distcol) < 5)
                D_bco_position_tot(distaccu,1) =
                bco(distrow,1);
                D_bco_position_tot(distaccu,2) =
                bco(distrow,2);
                D_barea_tot(distaccu) =
                barea(distrow)*pixtoleng^2;
                distaccu=distaccu+1;
            end
        end
    end
    D_barea_per_3frs(frN) = 0;
    for disttemp= distaccu_start:1:distaccu-1
        D_barea_per_3frs(frN) = D_barea_per_3frs(frN) +
         D_barea_tot(disttemp);
    end
    D_barea_per_3frs(frN) = D_barea_per_3frs(frN)/(distaccu-
```

```
        distaccu_start);
        D_ave_clusters_velocity(frN) =
        mean(mean(D_dist_bet_3frs))*pixtoleng*8;
        if(D_ave_clusters_velocity(frN) > 0)
            D_num_migration_per_3frs(frN) =
            length(D_dist_bet_3frs);
        else
            D_num_migration_per_3frs(frN) = 0;
            D_ave_clusters_velocity(frN) = 0;
        end
        D_n_X_D_a(frN) =
        length(D_dist_bet_3frs)*mean(mean(D_dist_bet_3frs))*pix
        toleng*8;
        if(D_num_migration_per_3frs(frN) > 0)
            for kk=1:1:D_num_migration_per_3frs(frN)
                D_all(jj)=D_ave_clusters_velocity(frN);
                jj=jj+1;
            end
            D_all(jj)=D_ave_clusters_velocity(frN);
            jj=jj+1;
        end
        if (frameNumber > NumFrames-3)
            continue;
        end
        tempbco=bco;
        frN=frN+1;
    elseif (frameNumber == 1)
        tempbco=bco;
    end
end
temp_position=zeros(distaccu-1,2);
for i_temp=1:1:distaccu-1
temp_position(i_temp,1)=D_bco_position_tot(i_temp,1);
temp_position(i_temp,2)=D_bco_position_tot(i_temp,2);
end
D_bco_position_tot=temp_position;

D_barea_tot(D_barea_tot==0) = [];
D_barea_per_3frs(D_barea_per_3frs==0) = [];
D_barea_per_3frs=transpose(D_barea_per_3frs);
D_ave_clusters_velocity=transpose(D_ave_clusters_velocity);
D_num_migration_per_3frs=transpose(D_num_migration_per_3frs);
D_n_X_D_a=transpose(D_n_X_D_a);
D_all=transpose(D_all);
ave_D_num=mean(D_num_migration_per_3frs);
ave_D_all=mean(D_all);
Tot_ABI_num= ave_D_num * ave_D_all * NumFrames / 24 / (pix_x *
pixtoleng)

Ave_sliding_snowman_area=mean(D_barea_tot)
plot(D_num_migration_per_3frs);
num_of_counted_cluster=transpose(num_of_counted_cluster);
-----------------------------------------------------------------
```

D. Comparison with other particle-based immunoassays

The performance of our device was compared with several other particle-based immunoaggregation assays, and the summary is given in the table below. Unfortunately, it was difficult to find methods to use NP in bead aggregation assay. Thus, methods for targeting other analytes have been compared. Most methods that provide highly sensitive detection require either a long reaction time or measurement time. In the case of 'Velocity' sensing (tracking the velocity of an aggregate produced by asymmetric immunobinding), the measurement time is approximately 30 min by manual tracking. Our proposed method provides decent performance considering the measurement time and various factors regarding biosensor.

Table A1 Comparison of several particle aggregation immunoassay

DETECTION METHOD*	TARGET ANALYTE	DETECTION RANGE*	ASSAY TYPE	PARTICLE SIZE	REACTION TIME*	MEASUREMENT TIME*	FEATURES	REF.
DIGITAL ELISA	TNF-α	0.01 ~ 10 pg/mL	ELISA	2.7 μm	**360 min**		Not particle aggregation method	**[1]**
RPS	Human ferritin	2.3 ~ 140 pM (1.04 ~ 62.4 ng/mL)	Symmetric	2.8 μm	30 min	25 min		**[2]**
RPS	Rabbit IgG	66 pM ~6.6 nM (10 ng/mL ~ 1 μg/mL)	Symmetric	2.0 μm	30 min	30 min		**[3]**
RPS	Human alpha-fetoprotein	95 fM ~ 25 pM	Symmetric	**290 nm**	**180 min**	20 min	Nano particle used	**[4]**
RPS	Mouse IgG	0.83 pM ~ 166.7 pM	Asymmetric	3 + 2.8 μm	**> 120 min**		Asymmetric considered as symmetric aggregation	**[5]**
VELOCITY	Rabbit IgG	1.5 pM ~ 6.25 nM	Asymmetric	1 μm + 50 nm	30 min	**30 min**	5 min for each particle measurement	**[6]**
VELOCITY	Goat IgG, Rabbit IgG, Mouse IgG	10.9 fM ~ 666.0 fM 30.6 fM ~ 799.2 fM 12.1 fM ~ 666.0 fM	Asymmetric	6 μm + 50 nm	30 min	**30 min**	5 min for each particle measurement	**[7]**
DYNAMIC ASSAY	Biotin BSA	3 pM ~ 70 pM	Symmetric	1 μm	-	17.5 min	Reaction and measurement performed simultaneously. Requires electromagnet.	**[8]**
SLIDING ASSAY	Influenza Nucleoprotein	0.70 pM ~ 1 nM (40 pg/mL ~ 54 ng/mL)	Asymmetric	2.8+1.0 μm	30 min (Single step)	**< 10 min (6 min)**	Sample volume: 6 μL Particle are mixed prior to antigen reaction	Ours

***Detection method:** RPS (Restive pulse sensor): Particle aggregates are characterized by electrical resistance measurement across a pore, Velocity: Asymmetric aggregates are characterized according to the velocity under the magnetic field. Dynamic assay: Particle aggregation was performed and characterized under an electromagnet.

***Detection range:** a linear region of a calibration curve or capable detection range mentioned in the paper.

***Reaction time:** Particle aggregation time (Antigen-antibody reaction time).

***Measurement time:** Detection time performed in the device.

References of table A1

[1] D. M. Rissin *et al.*, "Single-molecule enzyme-linked immunosorbent assay detects serum proteins at subfemtomolar concentrations," *Nature Biotechnology,* 28, 595-599, 2010.

[2] Y. Han, H. Wu, F. Liu, G. Cheng, and J. Zhe, "Label-Free Biomarker Assay in a Microresistive Pulse Sensor via Immunoaggregation," *Analytical Chemistry,* 86, 9717-9722, 2014.

[3] Y. Han, H. Wu, F. Liu, G. Cheng, and J. Zhe, "A multiplexed immunoaggregation biomarker assay using a two-stage micro resistive pulse sensor," *Biomicrofluidics,* 10, 024109, 2016.

[4] T. Takakura, I. Yanagi, Y. Goto, Y. Ishige, and Y. Kohara, "Single-molecule detection of proteins with antigen-antibody interaction using resistive-pulse sensing of submicron latex particles," *Applied Physics Letters,* 108, 123701, 2016.

[5] Z. Lin, X. Cao, P. Xie, M. Liu, and M. Javanmard, "PicoMolar level detection of protein biomarkers based on electronic sizing of particle

aggregates: theoretical and experimental considerations," *Biomedical Microdevices,* 17, 119, 2015.

[6] K. S. Kim and J. K. Park, "Magnetic force-based multiplexed immunoassay using superparamagnetic nanoparticles in microfluidic channel," *Lab on a Chip,* 5, 657-664, 2005.

[7] Y. K. Hahn, J. B. Chang, Z. Jin, H. S. Kim, and J. Y. Park, "Magnetophoretic position detection for multiplexed immunoassay using colored microspheres in a microchannel," *Biosensors & Bioelectronics,* 24, 1870-1876, 2009.

[8] Y. Moser, T. Lehnert, and M. A. M. Gijs, "On-chip immuno-agglutination assay with analyte capture by dynamic manipulation of superparamagnetic particles," *Lab on a Chip,* 9, 3261-3267, 2009.

국문 초록

비대칭 입자 응집 기반 미세유체 면역감지 시스템

기능성 마이크로/나노 입자는 생체 분자 또는 세포의 포획, 수송 및 검출 등 생체 분석에 사용된다. 콜로이드 입자 용액은 큰 결합 표면적을 제공하므로 시료 용액에서 표적 분자와의 효율적인 상호 작용이 가능하다. 미세 유체에서 이러한 입자의 조작은 생체 분석을 위한 다각적인 기회를 제공한다. 즉, 랩온어칩(Lab-on-a-Chip) 장치 또는 현장현시검사(Point-of-Care) 응용을 위한 중요한 요소이다.

본 논문에서는 서로 다른 크기와 자기 성질을 갖는 두 미세 입자 사이의 비대칭 면역 응집을 제안하고, 미세 유체 장치를 포함한 여러 가지 응집 검출 방법을 제시한다. 항원-항체 반응에 의해 형성된 입자 응집체는 대상 분자의 양에 따라 증가하는 것으로 알려져 있다. 대칭 입자 응집과 마찬가지로, 비대칭 응집 역시 목표 분석 물의 양에 따라 응집이 증가한다. 특히, 자기적 특성과 크기가 상이한 두 입자간의 결합이기 때문에, 형상을 판독하거나 외부 자기장을 사용하여 응집체를 쉽게 구별 할 수 있다. 본 연구는 용액에서 단일 입자와 응집체를 구별하고 비대칭 응집의 거동을 이해하는 광학 검출 방법을 제안했다. 그 후, 외부 자기장을 사용하여 비대칭 입자를 선별적으로 포착하는 자기장이 포함된 센서를 개발했다. 마지막으로 마이크로 채널 기반의 신속 면역 감지 센서가 개발되었다.

비대칭 면역 응집 입자 (AIPs: Asymmetric Immunoaggregated Particles)의 자기적 및 기하학적 특징으로 인하여 센서를 간단한 변환기 형태로 구현할 수 있다. 제안된 마이크로채널 기반 감지는 외

부 자기장과 유속 흐름 속의 AIP의 광학 모니터링을 통해 이루어진다. AIP는 자기장에 의해 마이크로 채널의 상단으로 끌어 당겨지며 유체 항력에 의해 표면을 따라 미끄러진다. 이 미끄럼 거동은 자성 및 폴리스티렌 구슬과 같은 다른 단일입자와는 대조적이다. 즉, 자성 입자가 작은 크기로 인해 거의 미끄러지지 않는 반면, 폴리스티렌 입자는 자력 부족으로 인해 빠르게 움직인다. AIP의 경우, 이에 비해 중간 속도로 미끄러지며 마이크로 채널의 지정된 감지 영역에서 정량적으로 포착될 수 있다. 본 연구에서는 동영상으로 촬영한 응집체의 거동을 분석하기 위해 맞춤형 프로그램을 개발하였다. 즉, 짧은 시간 동안 감지 영역을 통과하는 AIP의 총 개수와 속도를 분석하여 응집체를 정량화하였고 최종적으로 항원량을 도출하였다. 추가로 힘 분석을 통해 AIP의 궤적과 미끄러짐 거동을 분석하여 시스템 구성을 최적화 할 수 있었다.

제안된 시스템은 인플루엔자 A H1N1 핵 단백질에 대해 40 pg/mL ~ 54 ng/mL의 검출 범위를 나타낸다. 비특이적 응집은 항원이 없을 때 완충용액에서 (BSA 0.1% w/v) 2.47±0.59%로 얻어졌으며 감지 범위는 농도기준으로 1000 배 이상이다. 탐지에는 기존 방법(10 분 ~ 수 시간)보다 훨씬 빠른 6분 가량이 소요된다. 이 방법은 100X 이하의 약한 현미경 배율로 달성되므로 광학 요구 사항이 엄격하지 않고 형광이 필요하지 않다. 간단한 구조로 센서를 재사용할 수 있으며 저렴하고 견고하다.

주요어: 입자기반 면역분석, 면역응집, 비대칭응집, 광학감지,
랩온어칩(Lab-on-a-Chip), 현장현시검사